

## DISSIPATION AND EXTRA LIGHT IN GALACTIC NUCLEI: II. “CUSP” ELLIPTICALS

PHILIP F. HOPKINS<sup>1</sup>, THOMAS J. COX<sup>1,2</sup>, SUVENDRA N. DUTTA<sup>1</sup>, LARS HERNQUIST<sup>1</sup>, JOHN KORMENDY<sup>3</sup>, & TOD R. LAUER<sup>4</sup>

*Submitted to ApJ, January 23, 2008*

### ABSTRACT

We study the origin and properties of “extra” or “excess” central light in the surface brightness profiles of cusp or power-law elliptical galaxies. Dissipational mergers give rise to two-component profiles: an outer profile established by violent relaxation acting on stars already present in the progenitor galaxies prior to the final stages of the merger, and an inner stellar population comprising the extra light, formed in a compact central starburst. By combining a large set of hydrodynamical simulations with data that span a broad range of profiles at various masses, we show that observed cusp ellipticals appear consistent with the predicted “extra light” structure, and we use our simulations to motivate a two-component description of the observations that allows us to examine how the properties and mass of this component scale with e.g. the mass, gas content, and other properties of the galaxies. We show how to robustly separate the physically meaningful extra light and outer, violently relaxed profile, and demonstrate that the observed cusps and “extra light” are reliable tracers of the degree of dissipation in the spheroid-forming merger. We show that the typical degree of dissipation is a strong function of stellar mass, roughly tracing the observed gas fractions of disks of the same mass over the redshift range  $z \sim 0-2$ . We demonstrate a correlation between the strength of this component and effective radius at fixed mass, in the sense that systems with more dissipation are more compact, sufficient to explain the discrepancy in the maximum phase-space and mass densities of ellipticals and their progenitor spirals. We show that the outer shape of the light profile in simulated and observed systems (when fit to properly account for the central light) does not depend on mass, with a mean outer Sérsic index  $\sim 2.5$ . We also explore how this relates to e.g. the shapes, kinematic properties, and stellar population gradients of ellipticals. Extra light contributes to making remnants rounder and diskier, and imprints stellar population gradients. Simulations with the gas content needed to match observed surface brightness profiles reproduce the observed age, metallicity, and color gradients of cusp ellipticals, and we make predictions for how these can be used as tracers of the degree of dissipation in spheroid formation.

*Subject headings:* galaxies: elliptical and lenticular, cD — galaxies: evolution — galaxies: formation — galaxies: nuclei — galaxies: structure — cosmology: theory

### 1. INTRODUCTION

Thirty years ago, Toomre (1977) proposed the “merger hypothesis,” that major mergers between spirals could result in elliptical galaxies, and the combination of detailed observations of recent merger remnants (Schweizer 1982; Lake & Dressler 1986; Doyon et al. 1994; Shier & Fischer 1998; James et al. 1999; Genzel et al. 2001; Tacconi et al. 2002; Dasyra et al. 2006, 2007; Rothberg & Joseph 2004, 2006a) and e.g. faint shells and tidal features around ellipticals (Malin & Carter 1980, 1983; Schweizer 1980; Schweizer & Seitzer 1992; Schweizer 1996) have lent considerable support to this picture (e.g. Barnes & Hernquist 1992). Furthermore, in the now established  $\Lambda$ CDM cosmology, structure grows hierarchically (e.g. White & Rees 1978), making mergers an inescapable element in galaxy formation.

However, it has long been recognized that purely dissipationless (collisionless) mergers of stellar disks cannot explain the high mass and phase-space densities of nearby ellipticals (especially those of relatively low mass  $\lesssim L_*$ ), which are far more dense than local stellar disks of the same mass (Ostriker 1980; Carlberg 1986; Gunn 1987; Kormendy 1989).

Of course, spiral galaxies are not purely collisionless systems, but contain interstellar gas in addition to stars and dark matter. Furthermore, most ellipticals have old stellar populations, implying that their last gas-rich mergers occurred at  $z \gtrsim 1$ , and therefore their progenitors may be high-redshift spirals. These were likely more dense than nearby spirals, and observational evidence (Erb et al. 2006) indicates they had even larger gas fractions than their present-day counterparts ( $f_{\text{gas}} \sim 0.5$ , with some approaching  $f_{\text{gas}} \sim 0.8-0.9$ ). Because gas can radiate, it is not subject to Liouville’s Theorem, and processes related to gas dynamics and star formation can reconcile the high phase space densities of ellipticals relative to spirals (Gunn 1987; Lake 1989; Schweizer 1998). In detail, Hernquist et al. (1993) estimated that  $\sim 10\%$  of the stellar mass must be added in a compact dissipational component to account for the central densities of typical ellipticals.

The possible importance of gas dynamics and triggered star formation in mergers is reinforced by observations of ultraluminous infrared galaxies (ULIRGs) (e.g. Soifer et al. 1984a,b), which are always associated with mergers in the local Universe (Joseph & Wright 1985; Sanders & Mirabel 1996). The infrared emission from ULIRGs is thought to be powered by intense starbursts in the nuclei of these objects, originating in compact, central concentrations of gas (e.g. Scoville et al. 1986; Sargent et al. 1987, 1989), which will leave dense stellar remnants (Kormendy & Sanders 1992; Hibbard & Yun 1999; Rothberg & Joseph 2004). Moreover, observations of merging systems and gas-rich merger

<sup>1</sup> Harvard-Smithsonian Center for Astrophysics, 60 Garden Street, Cambridge, MA 02138

<sup>2</sup> W. M. Keck Postdoctoral Fellow at the Harvard-Smithsonian Center for Astrophysics

<sup>3</sup> Department of Astronomy, University of Texas, 1 University Station, Austin, Texas 78712

<sup>4</sup> National Optical Astronomy Observatory, Tucson, AZ 85726

remnants (e.g., Lake & Dressler 1986; Doyon et al. 1994; Shier & Fischer 1998; James et al. 1999), as well as post-starburst (E+A/K+A) galaxies (Goto 2005), have shown that their kinematic and photometric properties are consistent with them eventually evolving into typical  $\sim L_*$  elliptical galaxies. The correlations obeyed by these mergers and remnants (e.g., Genzel et al. 2001; Rothberg & Joseph 2006a,b, and references above) are similar to e.g. the observed fundamental plane and Kormendy (1977b) relations for relaxed ellipticals, and consistent with evolution onto these relations as their stellar populations age, as well as the clustering and mass density of ellipticals (Hopkins et al. 2007c).

The link between these processes and the formation of ellipticals may be manifest in their surface brightness profiles. Early work by e.g. Kormendy (1977a); King (1978); Young et al. (1978); Lauer (1985) and Kormendy (1985a) (see Kormendy 1987a, for a review) showed that typical elliptical surface brightness profiles were not as simple as uniform  $r^{1/4}$  laws. Typically, central profiles interior to  $\sim 1$  kpc deviate from  $r^{1/4}$  laws fitted to the envelopes of ellipticals, falling both above and below the inward extrapolation of the  $r^{1/4}$  law. Contemporaneously with the discovery of black hole-host galaxy correlations (e.g. Kormendy & Richstone 1995; Ferrarese & Merritt 2000; Gebhardt et al. 2000), *Hubble Space Telescope* observations of the centers of elliptical galaxies established that typical  $\lesssim L_*$  ellipticals exhibit central “cusps” – i.e. a continued rise in power-law like fashion towards small radii (Lauer et al. 1991, 1992; Crane et al. 1993; Ferrarese et al. 1994; Kormendy et al. 1994; Lauer et al. 1995; Kormendy 1999), whereas the most massive ellipticals appear to exhibit central flattening or “cores.” Kormendy (1999) demonstrated in a number of cases that these “cusps” appeared in some sense to be “extra” light, i.e. a distinct component above the inward extrapolation of the outer profile measured at large radii. With the combination of HST and ground-based photometry (Kormendy et al. 2008), it now appears that this excess is ubiquitous in “cuspy” or “power-law” ellipticals, with mass ranges and spatial extents comparable to those expected from observations of ongoing merger-induced starbursts (Hibbard & Yun 1999; Rothberg & Joseph 2004) and numerical simulations (Mihos & Hernquist 1994a; Hopkins et al. 2008d).

Faber et al. (1997) showed that the presence or absence of a cusp or power-law nuclear profile is strongly correlated with other, global properties of ellipticals – cusp ellipticals tend to be more rotationally supported, diskier, and have slightly higher ellipticities. They argued that these differences reinforce the idea that at least the cusp<sup>5</sup> ellipticals are the direct product of gas-rich mergers, with dissipation forming the central “cusp” and giving rise to correlated kinematic and photometric properties. The central excess or “extra light” in these cases may therefore represent a distinct imprint of the degree of dissipation in the spheroid-forming merger.

Numerical modeling over the past twenty years has also indicated that gas physics and star formation play key roles in shaping elliptical galaxies and has elucidated the relationship of mergers to the various phenomena described above. The possible relevance of these additional processes was anticipated already by Toomre & Toomre (1972), who asked

whether mergers would not “... tend to bring *deep* into a galaxy a fairly *sudden* supply of fresh fuel in the form of interstellar material ...” Barnes & Hernquist (1991, 1996) showed that tidal torques excited during *major* mergers excite rapid inflows of gas into the centers of galaxies, providing the fuel to power intense starbursts (Mihos & Hernquist 1994d, 1996) and to feed rapid black hole growth (Di Matteo et al. 2005; Hopkins et al. 2005b,a). Gas consumption by the starburst and dispersal of residual gas by supernova-driven winds and feedback from black hole growth (Springel et al. 2005a), culminating in a pressure-driven blast-wave (e.g. Hopkins et al. 2006b; Hopkins & Hernquist 2006), terminate star formation so that the remnant quickly evolves from a blue to a red galaxy. Provided that the interaction involved a “major” merger,<sup>6</sup> the remnant will resemble an elliptical galaxy, with the bulk of its mass on large scales made from progenitor stars which experienced violent relaxation (e.g. Barnes 1988, 1992; Hernquist 1992, 1993b), and the dissipation-induced starburst appropriately boosting the concentration and central phase space density (Hernquist et al. 1993; Robertson et al. 2006b; Naab et al. 2006a; Cox et al. 2006b). Moreover, Mihos & Hernquist (1994a) predicted that this process should leave an observable signature in the surface brightness profiles of remnants, in the form of an upwards departure from the outer de Vaucouleurs (1948)  $r^{1/4}$ -law distribution in the inner regions: i.e. a central “extra light” above the inwards extrapolation of the outer profile.

Understanding the processes responsible for establishing the structural properties of ellipticals and their correlations has the potential of revealing the formation histories of these objects. However, notwithstanding major observational and numerical advances, little effort has been made to use the extra light content of ellipticals in this manner, and most studies have restricted their focus to determining whether or not some extra light component is evident. This owes largely to the absence of a detailed theoretical framework: while the original work of Mihos & Hernquist (1994a) predicted that such cusps should exist, a more refined treatment of star formation and feedback, along with better resolution, is required for more detailed interpretation and modeling. For example, owing to limited spatial and temporal resolution and a simplified treatment of star formation, the “extra light” profiles predicted by Mihos & Hernquist (1994a) generally exhibited much more severe breaks than predicted by state-of-the-art simulations and seen in recent observations (see Appendix B). There have been considerable improvements in these areas in recent years (e.g. Springel & Hernquist 2003; Springel et al. 2005b; Cox et al. 2006c), and we take advantage of these refinements here, and in companion papers, Hopkins et al. (2008d) (hereafter Paper I) and Hopkins et al. (2008h,a), to study galaxy cusps or extra light in both simulations and observed systems. Our objective in this effort is to identify the existence and understand the origin of different components that contribute to the surface density profiles of ellipticals, their cosmological scalings and relevance for the formation history of such

<sup>6</sup> In a major merger, tidal forces are sufficiently strong to drive nuclear inflows of gas and build realistic spheroids. The precise meaning of major merger in this context is blurred by a degeneracy between the progenitor mass ratio and the orbit (Hernquist 1989; Hernquist & Mihos 1995; Bournaud et al. 2005), but both numerical (Younger et al. 2008) and observational (Dasyra et al. 2006; Woods et al. 2006) studies indicate that massive inflows of gas and morphological transformation are typical for mass ratios only below  $\sim 3:1$ . Unless otherwise noted, we generally take the term “mergers” to refer to major mergers.

<sup>5</sup> There are some differences in the literature in the use of the term “cusp ellipticals.” Unless otherwise stated, we will use it to refer to ellipticals without a central resolved core/flattening – i.e. “power-law” ellipticals.

galaxies, and their implications for global galaxy properties.

In this paper, we focus on the extra light in our simulations and in known cuspy elliptical galaxies. In § 2 and § 3 we describe our set of gas-rich merger simulations and the observational data sets we consider, respectively. In § 4, we compare different approaches for fitting the surface density profile, and attempt to calibrate various methods in order to recover the physically distinct (dissipational versus dissipationless) components in merger remnants. In § 5 we compare our simulations with and apply our fitted galaxy decomposition to a wide range of observed systems. In § 6 we use these comparisons to study how structural parameters of the outer stellar light and inner extra light component scale with galaxy properties. In § 7 we examine how the existence and strength of the extra light component is related to galaxy structure, global shape and rotation, and show that it drives galaxies along the fundamental plane. We investigate how this extra light component influences and is related to stellar population gradients in ellipticals in § 8. Finally, in § 9 we discuss our results and outline future explorations of these correlations.

Throughout, we adopt a  $\Omega_M = 0.3$ ,  $\Omega_\Lambda = 0.7$ ,  $H_0 = 70 \text{ km s}^{-1} \text{ Mpc}^{-1}$  cosmology, and appropriately normalize all observations and models shown, but this has little effect on our conclusions. We also adopt a Chabrier (2003) initial mass function (IMF), and convert all stellar masses and mass-to-light ratios to this choice. The exact IMF systematically shifts the normalization of stellar masses herein, but does not substantially change our comparisons. All magnitudes are in the Vega system, unless otherwise specified.

## 2. THE SIMULATIONS

Our merger simulations were performed with the parallel TreeSPH code GADGET-2 (Springel 2005), based on a fully conservative formulation (Springel & Hernquist 2002) of smoothed particle hydrodynamics (SPH), which conserves energy and entropy simultaneously even when smoothing lengths evolve adaptively (see e.g., Hernquist 1993a; O’Shea et al. 2005). Our simulations account for radiative cooling, optional heating by a UV background (as in Katz et al. 1996; Davé et al. 1999, although it is not important for the masses of interest here), and incorporate a sub-resolution model of a multiphase interstellar medium (ISM) to describe star formation and supernova feedback (Springel & Hernquist 2003). Feedback from supernovae is captured in this sub-resolution model through an effective equation of state for star-forming gas, enabling us to stably evolve disks with arbitrary gas fractions (see, e.g. Springel et al. 2005b; Springel & Hernquist 2005; Robertson et al. 2006a,c). This is described by the parameter  $q_{\text{eos}}$ , which ranges from  $q_{\text{eos}} = 0$  for an isothermal gas with effective temperature of  $10^4 \text{ K}$ , to  $q_{\text{eos}} = 1$  for our full multiphase model with an effective temperature  $\sim 10^5 \text{ K}$ . We also compare with a subset of simulations which adopt the star formation and feedback prescriptions from Mihos & Hernquist (1994a,d, 1996), in which the ISM is treated as a single-phase isothermal medium and feedback energy is deposited in a purely kinetic radial impulse (for details, see, e.g. Mihos & Hernquist (1994c)).

Although we find that they make little difference to the extra light component, most of our simulations include supermassive black holes at the centers of both progenitor galaxies. The black holes are represented by “sink” particles that accrete gas at a rate  $\dot{M}$  estimated from the local gas density and

sound speed using an Eddington-limited prescription based on Bondi-Hoyle-Lyttleton accretion theory. The bolometric luminosity of the black hole is taken to be  $L_{\text{bol}} = \epsilon_r \dot{M} c^2$ , where  $\epsilon_r = 0.1$  is the radiative efficiency. We assume that a small fraction (typically  $\approx 5\%$ ) of  $L_{\text{bol}}$  couples dynamically to the surrounding gas, and that this feedback is injected into the gas as thermal energy, weighted by the SPH smoothing kernel. This fraction is a free parameter, which we determine as in Di Matteo et al. (2005) by matching the observed  $M_{\text{BH}} - \sigma$  relation. For now, we do not resolve the small-scale dynamics of the gas in the immediate vicinity of the black hole, but assume that the time-averaged accretion rate can be estimated from the gas properties on the scale of our spatial resolution (roughly  $\approx 20 \text{ pc}$ , in the best cases). In any case, repeating our analysis for simulations with no black holes yields identical conclusions.

The progenitor galaxy models are described in Springel et al. (2005b), and we review their properties here. For each simulation, we generate two stable, isolated disk galaxies, each with an extended dark matter halo with a Hernquist (1990) profile, motivated by cosmological simulations (Navarro et al. 1996; Busha et al. 2005), an exponential disk of gas and stars, and (optionally) a bulge. The galaxies have total masses  $M_{\text{vir}} = V_{\text{vir}}^3 / (10GH[z])$  for an initial redshift  $z$ , with the baryonic disk having a mass fraction  $m_d = 0.041$ , the bulge (when present) having  $m_b = 0.0136$ , and the rest of the mass in dark matter. The dark matter halos are assigned a concentration parameter scaled as in Robertson et al. (2006c) appropriately for the galaxy mass and redshift following Bullock et al. (2001). We have also varied the concentration in a subset of simulations, and find it has little effect on our conclusions because the central regions of the galaxy are baryon-dominated. The disk scale-length is computed based on an assumed spin parameter  $\lambda = 0.033$ , chosen to be near the mode in the  $\lambda$  distribution measured in simulations (Vitvitska et al. 2002), and the scale-length of the bulge is set to 0.2 times this. Modulo explicit variation in these parameters, these choices ensure that the initial disks are consistent with e.g. the observed baryonic Tully-Fisher relation and estimated halo-galaxy mass scaling laws (Bell & de Jong 2001; Kormendy & Freeman 2004; Mandelbaum et al. 2006, and references therein).

Typically, each galaxy initially consists of 168000 dark matter halo particles, 8000 bulge particles (when present), 40000 gas and 40000 stellar disk particles, and one black hole (BH) particle. We vary the numerical resolution, with many simulations using twice, and a subset up to 128 times, as many particles. We choose the initial seed mass of the black hole either in accord with the observed  $M_{\text{BH}} - \sigma$  relation or to be sufficiently small that its presence will not have an immediate dynamical effect, but we have varied the seed mass to identify any systematic dependencies. Given the particle numbers employed, the dark matter, gas, and star particles are all of roughly equal mass, and central cusps in the dark matter and bulge are reasonably well resolved. The typical gravitational softening in our simulations is  $\sim 20 - 50 \text{ pc}$  in the  $\lesssim L_*$  systems of particular interest here, with a somewhat higher  $\sim 50 - 100 \text{ pc}$  in the most massive systems (yielding an effectively constant resolution  $\sim 0.01 R_e$  in terms of the effective radius). In Paper I and Appendix B we demonstrate that this is sufficient to properly resolve not only the mass fractions but also the spatial extent of the extra light components of interest here (although resolution may become an issue when attempt-

ing to model the very smallest galaxies, with  $R_e \lesssim 100$  pc and  $L < 0.01 L_*$ , as discussed in § 5). The hydrodynamic gas smoothing length in the peak starburst phases of interest is always smaller than this gravitational softening.

We consider a series of several hundred simulations of colliding galaxies, described in Robertson et al. (2006b,c) and Cox et al. (2006a,b). We vary the numerical resolution, the orbit of the encounter (disk inclinations, pericenter separation), the masses and structural properties of the merging galaxies, initial gas fractions, halo concentrations, the parameters describing star formation and feedback from supernovae and black hole growth, and initial black hole masses.

The progenitor galaxies have virial velocities  $V_{\text{vir}} = 55, 80, 113, 160, 226, 320,$  and  $500 \text{ km s}^{-1}$ , and redshifts  $z = 0, 2, 3,$  and  $6$ , and our simulations span a range in final spheroid stellar mass  $M_* \sim 10^8 - 10^{13} M_\odot$ , covering essentially the entire range of the observations we consider at all redshifts, and allowing us to identify any systematic dependencies in our models. We consider initial disk gas fractions by mass of  $f_{\text{gas}} = 0.05, 0.1, 0.2, 0.4, 0.6, 0.8,$  and  $1.0$  (defined as the fraction of disk baryonic mass which is gas) for several choices of virial velocities, redshifts, and ISM equations of state. The results described in this paper are based primarily on simulations of equal-mass mergers; however, by examining a small set of simulations of unequal mass mergers, we find that the behavior does not change dramatically for mass ratios to about 3:1 or 4:1. The mass ratios we study are appropriate for the observations of ellipticals used in this paper, which are only formed in our simulations in major merger events. At higher mass ratios, the result is a small bulge in a still disk-dominated galaxy (see e.g. Younger et al. 2008; Hopkins et al. 2008c,g), which we do not study here.

Each simulation is evolved until the merger is complete and the remnants are fully relaxed, typically  $\sim 1 - 2$  Gyr after the final merger and coalescence of the BHs. We then analyze the remnants following Cox et al. (2006b), in a manner designed to mirror the methods typically used by observers. For each remnant, we project the stars onto a plane as if observed from a particular direction, and consider 100 viewing angles to each remnant, which uniformly sample the unit sphere. Given the projected stellar mass distribution, we calculate the iso-density contours and fit ellipses to each (fitting major and minor axis radii and hence ellipticity at each iso-density contour), moving concentrically from  $r = 0$  until the entire stellar mass has been enclosed. This is designed to mimic observational isophotal fitting algorithms (e.g. Bender et al. 1987; Bender 1988). The radial deviations of the iso-density contours from the fitted ellipses are expanded in a Fourier series in the standard fashion to determine the boxyness or diskyness of each contour (the  $a_4$  parameter). Throughout, we show profiles and quote our results in terms of the major axis radius. For further details, we refer to Cox et al. (2006b).

We directly extract the effective radius  $R_e$  as the projected half-mass stellar effective radius, and the velocity dispersion  $\sigma$  as the average one-dimensional velocity dispersion within a circular aperture of radius  $R_e$ . This differs from what is sometimes adopted in the literature, where  $R_e$  is determined from the best-fitting Sérsic profile, but because we are fitting Sérsic profiles to the observed systems we usually quote both the true effective radius of the galaxy and effective radii of the fitted Sérsic components. Throughout, the stellar mass  $M_*$  refers to the total stellar mass of the galaxy, and the dynamical

mass  $M_{\text{dyn}}$  refers to the traditional dynamical mass estimator

$$M_{\text{dyn}} \equiv k \frac{\sigma^2 R_e}{G}, \quad (1)$$

where we adopt  $k = 3.8$  (roughly what is expected for a Hernquist (1990) profile, and the choice that most accurately matches the true enclosed stellar plus dark matter mass within  $R_e$  in our simulations; although this choice is irrelevant as long as we apply it uniformly to both observations and simulations). When we plot quantities such as  $R_e$ ,  $\sigma$ , and  $M_{\text{dyn}}$ , we typically show just the median value for each simulation across all  $\sim 100$  sightlines. The sightline-to-sightline variation in these quantities is typically smaller than the simulation-to-simulation scatter, but we explicitly note where it is large.

### 3. THE DATA

We compare our simulations to and test our predictions on an ensemble of observed surface brightness profiles of ellipticals. Specifically, we consider three samples of cusp or extra light ellipticals and a compilation of remnants of recent gas-rich mergers. The first is the V-band Virgo elliptical survey of Kormendy et al. (2008), based on the complete sample of Virgo galaxies down to extremely faint systems  $M_B \sim -15$  in Binggeli et al. (1985) (the same sample studied in Côté et al. 2006; Ferrarese et al. 2006). Kormendy et al. (2008) combine observations from a large number of sources (including Bender et al. 1988, 2007; Caon et al. 1990, 1994; Davis et al. 1985; Jedrzejewski et al. 1987; Jedrzejewski 1987; Kormendy et al. 2005; Lauer 1985; Lauer et al. 1995, 2005; Liu et al. 2005; Peletier et al. 1990) and new photometry from McDonald Observatory, the HST archive, and the SDSS for each of their objects which (after careful conversion to a single photometric standard) enables accurate surface brightness measurements over a wide dynamic range (with an estimated zero-point accuracy of  $\pm 0.04 \text{ V mag arcsec}^{-2}$ ). Typically, the galaxies in this sample have profiles spanning  $\sim 12 - 15$  magnitudes in surface brightness, corresponding to a range of nearly four orders of magnitude in physical radii from  $\sim 10$  pc to  $\sim 100$  kpc, permitting the best simultaneous constraints on the shapes of both the outer and inner profiles of any of the objects we study. The profiles include e.g. ellipticity,  $a_4/a$ , and  $g-z$  colors as a function of radius. Unfortunately, since this is restricted to Virgo ellipticals, the number of galaxies is limited, especially at the intermediate and high end of the mass function.

We therefore add surface brightness profiles from Lauer et al. (2007a), further supplemented by Bender et al. (1988). Lauer et al. (2007a) compile V-band measurements of a large number of nearby systems for which HST imaging of the galactic nuclei is available. These include the Lauer et al. (2005) WFPC2 data-set, the Laine et al. (2003) WFPC2 BCG sample (in which the objects are specifically selected as brightest cluster galaxies from Postman & Lauer (1995)), and the Lauer et al. (1995) and Faber et al. (1997) WFPC1 compilations (see also Quillen et al. 2000; Rest et al. 2001; Ravindranath et al. 2001). Details of the treatment of the profiles and conversion to a single standard are given in Lauer et al. (2007a). The sample includes ellipticals over a wide range of luminosities, down to  $M_B \sim -15$ , but is dominated by intermediate and giant ellipticals, with typical magnitudes  $M_B \lesssim -18$ . This therefore greatly extends our sampling of the intermediate and high-mass end of the

mass function, but at the cost of some dynamic range in the data. The HST images alone, while providing information on the central regions, typically extend to only  $\sim 1$  kpc outer radii, which is insufficient to fit the outer profile. Lauer et al. (2007a) therefore combine these data with ground-based measurements from a number of sources (see the references for the Kormendy et al. (2008) sample) to construct profiles that typically span physical radii from  $\sim 10$  pc to  $\sim 10-20$  kpc. Although the composite profiles were used in Lauer et al. (2007a) to estimate effective radii, they were not actually shown in the paper. It should also be noted that there is no single criterion that characterizes galaxies included in this sample, but they generally comprise luminous nearby ellipticals and S0 galaxies for which detailed imaging is available. We emphasize that issues of completeness and e.g. environment are not important for any of our conclusions.

We occasionally supplement the profiles from Lauer et al. (2007a) with additional profiles used in Bender et al. (1988, 1992, 1993, 1994), and in some cases subsequently updated. These are more limited: typically the profiles cover  $\sim 7$  magnitudes in surface brightness, extending from  $\sim 30-50$  pc out to  $\sim$  a few kpc (typically  $\sim 3$  kpc in low-luminosity systems, and  $\sim 15$  kpc in the brightest systems, sufficient for acceptable, but not strong constraints on the outer profile shapes). However, the measurements are usually in each of the  $V$ ,  $R$ , and  $I$  bands, and hence allow us to construct multicolor surface brightness, ellipticity, and  $a_4/a$  profiles. We use this to estimate e.g. the sensitivity of the fitted parameters and galaxy profiles on the observed waveband and on the quality and dynamic range of the photometry.

In various places, we compare our results from the study of these ellipticals to our results in Paper I from a study of local remnants of gas-rich merger remnants (Rothberg & Joseph 2004). For these objects, Rothberg & Joseph (2004) compile  $K$ -band imaging, surface brightness, ellipticity, and  $a_4/a$  profiles, where the profiles typically range from  $\sim 100$  pc to  $\sim 10-20$  kpc. These span a moderate range in luminosity (including objects from  $M_K \sim -20$  to  $M_K \sim -27$ , but with most from  $M_K \sim -24$  to  $M_K \sim -26$ ) and a wide range in merger stage, from ULIRGs and (a few) unrelaxed systems to shell ellipticals. As demonstrated in Rothberg & Joseph (2004) and argued in Paper I, these systems will almost all become (or already are, depending on the classification scheme used) typical  $\sim L_*$  ellipticals, with appropriate phase space densities, surface brightness profiles, fundamental plane relations, kinematics, and other properties. For a detailed discussion of the modeling of these systems and the profiles themselves, we refer to Paper I (all of the results shown for these systems are derived therein). We show the results from Paper I here in order to test the continuity of merger remnant and (cusp) elliptical populations.

Because we are here specifically interested in extra light or cusps in observed ellipticals, and because the generally accepted belief is that core ellipticals are not directly formed in gas-rich major mergers but are subsequently modified by dry re-mergers (see e.g. Faber et al. 1997; van Dokkum 2005; Bell et al. 2006), we restrict our attention only to those ellipticals which are confirmed via HST observations as being cusp ellipticals. We include all the confirmed gas-rich merger remnants, but note there are a small number of extreme unrelaxed cases for which sharp features in the surface brightness profiles prevented derivation of meaningful quantities (note, however, as shown in Paper I, that almost all of the objects in this sample are sufficiently well-relaxed at the radii of inter-

est for our fitting). We exclude dwarf spheroidals, as they are not believed to form in major mergers as are ellipticals (e.g. Kormendy 1985b, 1987b; Kormendy et al. 2008), and in any case they dominate at extremely low masses where our simulations do not sample the population (they also predominate as satellite galaxies, whose effects we do not model).

We also exclude S0 galaxies (adopting the morphological classifications from Kormendy et al. (2008) and Lauer et al. (2007a), although it makes little difference exactly which classifications we consider). This is not because of a physical distinction: observations suggest that these likely form a continuous family with the low-luminosity cusp ellipticals, and in fact a number of our simulated gas-rich merger remnants would, from certain viewing angles, be classified as S0s. However, in order to derive e.g. the parameters of the outer, violently relaxed profile and central extra light, it would be necessary to remove the contribution of the large-scale disk from the surface brightness profiles of these objects. Our two-component (outer dissipationless and inner dissipational) Sérsic models (described in § 4) then become three-component fits, and the degeneracies involved with three independent components, even with our best data and simulations, are so large as to render the results meaningless. We have, however, re-visited all of the S0s in these samples in light of our results, and find that they are, in all cases, consistent with our predicted and observed trends. However, it is too difficult to infer these trends directly from the S0s themselves without ideal disk subtraction.

This yields a final sample of  $\approx 80$  unique elliptical galaxies, and  $\approx 50$  confirmed remnants of gas-rich mergers. Most of the sample spans a range of three orders of magnitude in stellar mass, from  $\lesssim 0.1 M_*$  to  $\sim 10 M_*$ , and a wide range in extra light properties. There is, of course, some overlap in the samples that define our compilation; we have  $\sim 300$  surface brightness profiles for our collection of  $\approx 80$  unique ellipticals, including (for many objects) repeated measurements in multiple bands and with various instruments. This turns out to be quite useful, as it provides a means to quantify error estimates in fits to these profiles. The variations between fit parameters derived from observations in different bands or made using different instruments are usually much larger than the formal statistical errors in the fits to a single profile. There are no obvious systematic effects (i.e. systematic changes in profile fits from  $V$  to  $I$  band), but as demonstrated in Paper I the effects of using different bands or changing dynamic range (from different instruments) can be complex, depending on the structure and degree of relaxation of the outer regions of a system. On the other hand, there are well-relaxed objects for which almost no significant change in the fits occurs from band to band. It is therefore useful to have multiple observations of the same system, as it allows us to get some idea of how sensitive our fits are to differences in e.g. the choice of observed wavelength or dynamic range from instrument to instrument.

In Table 1, we list the names and properties of our sample ellipticals, including the relevant sources of photometry, stellar masses, absolute magnitudes, stellar velocity dispersions and effective radii, ellipticities, isophotal shapes, and rotation properties. We have converted all the observations to physical units given our adopted cosmology, and compile global parameters (where not available in the original papers) including e.g. kinematic properties, luminosities, and black hole masses from the literature. We determine stellar masses ourselves in a uniform manner for all the objects, based on

their total  $K$ -band luminosities and  $(B-V)$  color-dependent mass-to-light ratios from Bell et al. (2003), corrected for our adopted IMF. We have also repeated our analysis using stellar masses derived from a mean  $M/L$  as a function of luminosity or from fitting the integrated  $UBVRJHK$  photometry of each object to a single stellar population with the models of Bruzual & Charlot (2003), and find this makes no difference to our conclusions.

Throughout, we will usually refer interchangeably to the observed surface brightness profiles in the given bands and the surface stellar mass density profile. Of course, stellar light is not exactly the same as stellar mass, but in Paper I and § 8 herein, we consider the differences between the stellar light and the stellar mass density profiles as a function of time, wavelength, and properties of the merger remnant, and show that the  $V$  and  $K$ -band results introduce little bias (i.e. are good tracers of the stellar mass); the Sérsic indices and extra light fractions fitted to the  $K$ -band profiles of the simulations are good proxies for the Sérsic index of the stellar mass profile and extra mass/starburst mass fraction, even close in time to the peak episode of star formation.

Although we are not concerned about the absolute normalization of the profile (i.e. mean  $M/L$ ), since we derive total stellar masses separately from the integrated photometry, we must account for systematics that might be induced by a change in  $M/L$  as a function of radius. The results from our merger remnant sample (observed in  $K$ -band) are, on average, robust in this sense, but they should be treated with care, especially in the most extreme cases (namely the few LIRGs and ULIRGs in the sample), where younger stellar populations may decrease  $M/L$  towards their center (see § 8). We emphasize though that many of these systems are much older and more relaxed (e.g. ellipticals with faint shells or tidal debris). The profiles in optical bands such as  $V$  require more care – when the system is very young ( $\lesssim 1-2$  Gyr after the major merger-induced peak of star formation), there can be considerable bias or uncertainty owing to stellar population gradients and dust. However, once the system is relaxed, the optical bands also become good proxies for the stellar mass distribution.

In fact, in Paper I and § 8 we demonstrate that once the system reaches intermediate age, the bias in e.g.  $B$  or  $V$  band is often less than that in  $K$  band, because systems tend to be both younger and more metal rich in their centers. In  $K$ -band, these both increase  $L/M$ , leading to a (small) systematic bias. In optical bands, however, the two have opposite effects (younger age increases  $L/M$ , but higher metallicity decreases  $L/M$ ), and they tend to mostly cancel. Since essentially all of our ellipticals are older than this stellar population age (even in their centers), and they have been carefully vetted and either corrected for the effects of e.g. dust lanes in the sources or (where correction was too difficult) excluded from our samples (see Kormendy et al. 2008; Lauer et al. 2007a), we are not concerned that significant bias might persist. Furthermore, comparison of systems observed in different bands demonstrates that our conclusions are unchanged (modulo small systematic offsets) regardless of the observed bands in which we analyze these systems. As has been noted in other works, most of these objects have weak color gradients, indicating little variation in  $M/L$  with radius.

#### 4. RECOVERING THE PHYSICALLY APPROPRIATE “EXTRA LIGHT”

We would like to use the surface brightness profiles of merger remnants to estimate the contribution from extra light and, in particular, to infer the fraction of stellar mass that was formed in a compact central starburst. However, as noted in Paper I, the light profiles in our simulation remnants are quite smooth, even where the extra light fraction is large. This makes recovering the extra light component a non-trivial procedure, which can be sensitive to the assumptions made in fitting (see also Naab & Trujillo 2006). We discuss various procedures and their consequences in Paper I, but briefly review them to highlight the most important decomposition we will adopt.

Figure 1 shows the surface density profile of a typical merger remnant from our simulation library, with a gas fraction of  $\sim 10\%$ , which happens to provide a good match to several observed ellipticals. We begin by reducing the profile to the two most physically relevant components: the “pre-starburst” or “disk” stars, i.e. those formed in the rotationally supported disks before the final coalescence of the galaxies, and the “starburst” stars, produced in the final, compact starburst. We operationally define this as stars formed within  $\pm 125$  Myr of the peak in the starburst star formation, but since the starburst is usually very distinct, changing this definition within reason makes almost no difference. We combine both the stars present in the stellar disks at the beginning of our calculations and the stars formed in the disks over the course of the simulations (the disk stars and pre-starburst stars in Figure 1 of Paper I) into a single pre-starburst stellar population, because there is no robust physical distinction between the two. Not only do both populations experience violent relaxation in the final merger/coalescence, but it is also arbitrary where (or at what time) we initialize our simulations, relative to the final merger, and therefore what fraction of the stellar mass forms before our simulation begins.

We also neglect embedded stellar disks which can be formed by gas remaining after the merger; as demonstrated in Paper I, these contribute negligibly to the surface mass density profile in even the most gas-rich merger remnants (and we are primarily concerned with the surface mass density profiles, not the early-time optical/UV light profiles which more strongly reflect the light from new stars). This does not mean such disks are unimportant – indeed they are ubiquitous in gas-rich merger remnant simulations and contribute critically to the kinematics (especially the rotation and  $a_4$ , see Cox et al. 2006b), and observations suggest that low-level disks may be present in nearly all cusp galaxies (perhaps all, given projection effects; see Ferrarese et al. 1994; Lauer et al. 2005). However, especially given our exclusion of S0 galaxies, these are not a significant component of the surface brightness profiles.

We showed in Paper I that the total profile of the system can be robustly represented as a two-component sum of two Sérsic distributions. If we fit each known physical component separately, we find that the pre-starburst component follows a nearly exact Sérsic law (here,  $n_s = 2.85$ ), while the inner component (given its shape and origin in a gas-rich, dissipational event) can be well fit by a lower- $n_s \sim 1$  law.<sup>7</sup> Based on this

<sup>7</sup> Formally, we consider our simulation profiles outside of some multiple  $\sim 3-5$  times the resolution limit, or with a seeing correction appropriate for the comparison observed samples. We equally sample the profile in  $\log r$  over a dynamic range extending to the largest radii in the observed samples (§ 3), and weight each point equally assuming an intrinsic  $\sim 0.1$  mag point-to-point variance in the SB profile (the typical magnitude of residuals fitting arbitrary splines to the data). We have varied these choices and find that our fits and

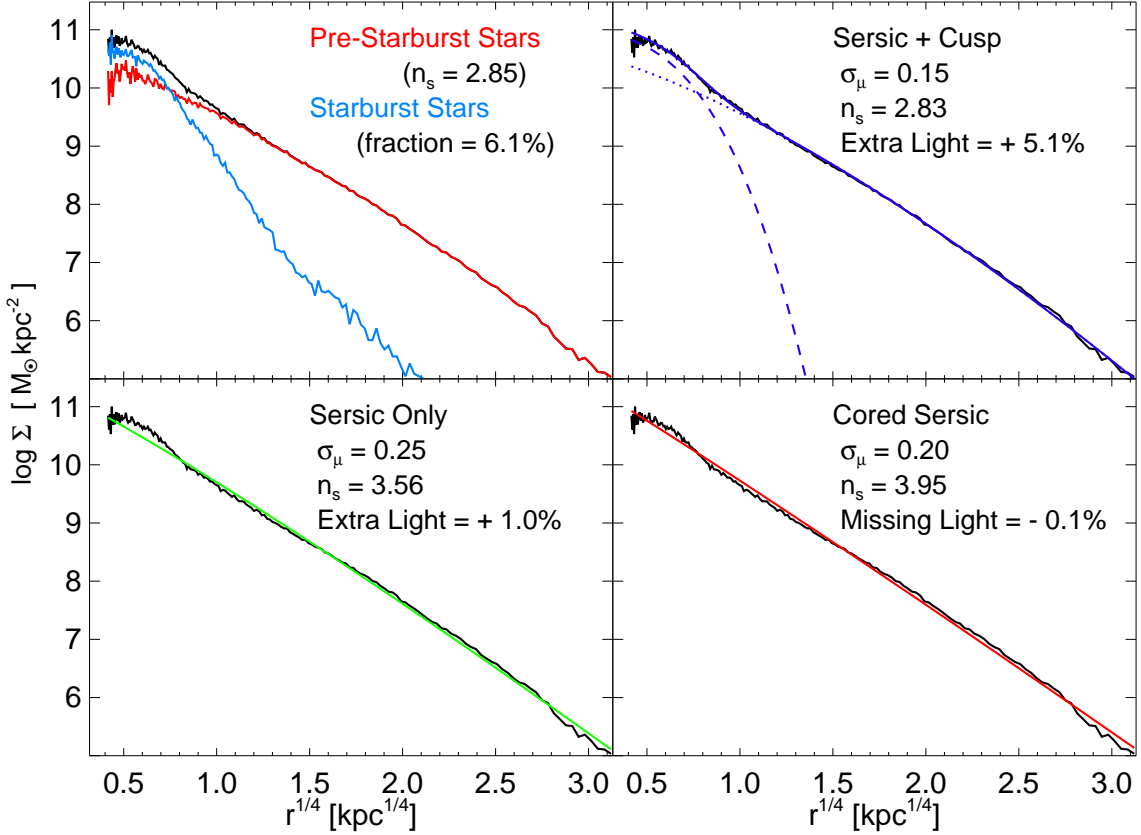


FIG. 1.— *Upper Left*: Surface mass density of a typical merger remnant from our simulation library (black), decomposed into stars formed prior to the final merger (which are then violently relaxed; red) and stars formed in the dissipational starburst (blue). The Sérsic index fitted to the pre-starburst component alone is shown, with the stellar mass fraction of the starburst component. *Upper Right*: Two-component (Sérsic plus cusp or extra light) fit (inner exponential and outer Sérsic) to the total light profile, with the Sérsic index of the outer component and mass fraction of the inner component, and rms scatter ( $\sigma_\mu$ , in mag arcsec $^{-2}$ ) about the fit. *Lower Left*: Single Sérsic function fit to the profile. *Lower Right*: Core-Sérsic function fit. Our two-component, cusp plus Sérsic function fit (*top right*) accurately recovers the profile of the violently relaxed component and mass fraction of the starburst component. The other fits give less intuitive results in this case.

behavior, we therefore adopt a two-component decomposition of the observed quantity, the total surface brightness profile. This is defined as a Sérsic plus cusp or extra light model, with an outer component for the pre-starburst stars with a free Sérsic index, and an inner component reflecting the starburst stars (with fixed  $n_s = 1$  when the shape of the starburst is not well-resolved, or free – albeit still generally low –  $n_s$  when resolution permits). We have studied this decomposition in Paper I, and show that it provides a good description of both simulated and observed merger remnant profiles, accurately separating the central light of younger stellar populations (as observationally determined) from the light of older stars, which form a more extended distribution. The total surface brightness profile is then

$$I_{\text{tot}} = I' \exp \left\{ -b'_n \left( \frac{r}{R_{\text{extra}}} \right)^{1/n'_s} \right\} + I_o \exp \left\{ -b_n \left( \frac{r}{R_{\text{outer}}} \right)^{1/n_s} \right\}, \quad (2)$$

where  $R_{\text{extra}}$  and  $R_{\text{outer}}$  are the effective radii of the inner ( $n'_s \sim 1$ ) and outer ( $n_s$ ) components (which we identify with the starburst and old bulge or pre-starburst components, respectively),  $I'$  and  $I_o$  are the corresponding normalizations,  $n'_s$  is the Sérsic index of the inner (extra light) component

conclusions are not sensitive to them.

(fixed  $n'_s = 1$  where resolution limits apply) and  $n_s$  is the Sérsic index of the outer bulge or pre-starburst component. The constant  $b_n$  is the appropriate function of  $n_s$  such that  $R_{\text{extra}}$  and  $R_{\text{outer}}$  correspond to the projected half-mass radii.

The upper right panel of Figure 1 shows an example of the outcome of such a fit. The resulting model of the surface density profile fits the simulation well, with a rms deviation ( $\sigma_\mu \equiv \langle \Delta\mu^2 \rangle^{1/2}$ ) of only  $\sigma_\mu \sim 0.15$  mag (assuming  $\mu \propto -2.5 \log I_{\text{tot}}$ ). This is comparable to the point-to-point variance in the profile of this simulation if we fit an arbitrary spline to the data, and thus reflects a genuinely good fit. More important, this fit, despite having no direct information about the physical components into which we decompose the brightness profile, recovers almost exactly the appropriate parameters for both components. The best-fit Sérsic index ( $n_s = 2.83$  compared to 2.85) and effective radius of the outer or bulge component reproduce well those from fitting directly to the pre-starburst stellar population. Likewise, the inner or extra light component is a good match to the starburst component, and the fit recovers the extra light fraction accurately (5.1% compared to 6.1%; a smaller difference than reasonable uncertainties in our physical definition of the starburst component). Again, we emphasize that we have simply fit a function of the form in Equation (2) to the total surface brightness profile, ignoring our knowledge of the genuine physical breakdown; but we find that we recover an accurate reflection of that true decomposition.



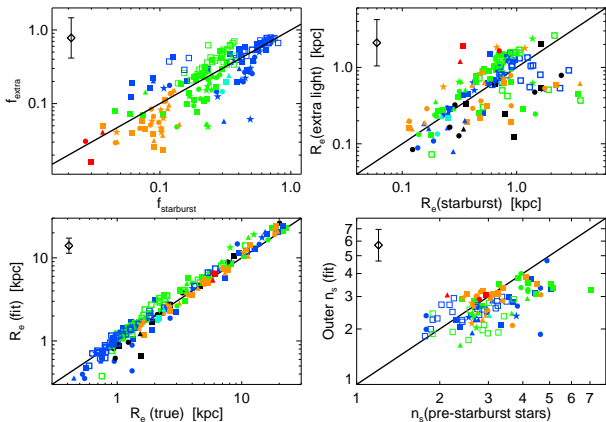


FIG. 2.— Success of our proposed two-component empirical decomposition at recovering the known physical parameters of the galaxy starburst and pre-starburst (violently relaxed) components. *Top Left*: Mass fraction in the fitted “extra light” component  $f_{\text{extra}}$  versus the known mass fraction of the physical starburst  $f_{\text{sb}}$ . Each point is the average across  $\sim 100$  sightlines to a given simulation, although the sightline-to-sightline variance is moderate ( $\approx 0.15$  dex). Different colors and symbols denote different initial disk gas fractions, orbital parameters, and merger redshifts (see key in Figure 14). The fitted  $f_{\text{extra}}$  recovers the physical  $f_{\text{sb}}$  on average, with a factor  $\sim 2$  scatter (plotted error bar), and without any significant bias from any varied simulation parameters. *Top Right*: Fitted effective radius of the extra light component versus the projected half-mass radius of the known starburst stars. Again, the true values are recovered with a factor  $\sim 2$  scatter, independent of simulation choices. *Bottom Left*: Fitted effective radius of the entire galaxy versus  $R_e$  from direct profile integration. The fits recover  $R_e$  to better than  $\sim 0.1$  dex. *Bottom Right*: Fitted Sérsic index of the outer (dissipationless) component versus that fitted directly to the known pre-starburst component profile. The outer profile shape  $n_s$  is recovered to within  $\sim 0.1$  dex (the only significant bias is when there is a large disk in the remnant; but those cases are not relevant for this paper). The empirical decompositions do well at recovering the known parameters in the simulations, across the entire range of simulation parameter space we have surveyed.

Figure 2 shows the results of repeating this procedure for several hundred simulations; we directly compare the fitted extra light mass fraction and size ( $R_{\text{extra}}$ ) to the mass fraction and size of the known physical starburst component, and find that the fitted components recover the physical values in the mean with a factor  $\sim 2$  scatter. This result is robust with respect to e.g. the mass, orbital parameters, mass ratios, initial gas content, treatment of feedback and model for the ISM equation of state, and redshift of our simulations. We similarly compare the effective radius of the entire galaxy determined from these fits to that known from the direct integration of the profile. The fits recover  $R_e$  to within  $\sim 20\text{--}25\%$ , given a dynamic range comparable to the observations with which we compare. We also compare the Sérsic index of the fitted outer component to that fitted directly to the known physical pre-starburst component and find the two agree within  $\sim 30\text{--}40\%$ , without any systematic dependences except where the remnants have large embedded disks (biasing the fitted decompositions to lower  $n_s$ ). This gives us confidence that such an empirical approach can be used, in a statistical sense, to recover physically meaningful parameters describing the galaxy components.

We note that, so long as we are fitting radii  $\gtrsim 50$  pc, we obtain similar results for a free inner component shape parameter  $n'_s$  or fixed inner  $n'_s = 1$ . In Paper I we demonstrate that the choice of  $n'_s = 1$  for the inner component recovers, on average, the correct physical mass fraction which participated in the starburst, and mitigates against degeneracies in fitting to the outer Sérsic profile (so that we recover the same value if we fit the two stellar populations

independently). We therefore adopt this choice for our decompositions in situations where we cannot reliably resolve the innermost extra light shape/structure (namely our simulations and the observed samples of Rothberg & Joseph (2004) and Bender et al. (1988)). We emphasize, however, that this choice for the inner component does *not* imply that this reflects the true shape of the central extra light, which can be complex (see e.g. the range of central profile shapes in Lauer et al. 2005; Côté et al. 2006; Kormendy et al. 2008). In fact, caution should be taken when considering the central  $\sim 30\text{--}50$  pc, which our simulations do not generally resolve (for most of the galaxy observations considered here, this corresponds to  $\sim 0.5''$ , a factor  $\sim 10$  larger than the HST diffraction limit). We include a detailed discussion of profile shapes as  $r \rightarrow 0$  in Appendix B.

For now, we simply note that the quantities of interest here are well-converged in resolution studies, and our numerical tests (smoothing extremely high-resolution simulations over various seeing) find that  $n'_s = 1$  choice is robust (in the sense that the mean properties are recovered similarly in either case). However, where the information is available in the central regions of the galaxy (namely the samples of Kormendy et al. (2008) and Lauer et al. (2007a)), we find the best results using all of the information and freeing the Sérsic index of the inner light component, to accommodate the real, observed shapes and structure in the inner light component. Despite these caveats, our treatment describes the starburst mass profile well where it is important to the overall surface density (from  $\sim 100$  pc to  $\sim 1$  kpc) and accurately recovers the total mass in the starburst component and its effective radius.

We apply this formalism to the observed systems in § 5 below<sup>8</sup>, and we present the results of our fits to each elliptical in our sample in Table 1. For sources with multiple independent observations, we define error bars for each fit parameter representing the  $\sim 1\sigma$  range in parameters derived from various observations, typically from three different surface brightness profiles but in some cases from as many as  $\approx 5\text{--}6$  sources (where there are just 2 sources, the “error” is simply the range between the two fits). In many cases the different observations are comparable; in some there are clearly measurements with larger dynamic range and better resolution: the errors derived in this manner should in such cases be thought of as the typical uncertainties introduced by lower dynamic range or less accurate photometry.

In terms of direct comparison with our simulations, the data often cover a dynamic range and have resolution comparable to our simulations, provided we do not heavily weight the very central ( $\lesssim 30$  pc) regions of HST nuclear profiles. Experimenting with different smoothings and imposed dynamic range limits, we find it is unlikely that resolution or seeing differences will substantially bias our comparisons. They do introduce larger scatter; the robustness of our results increases considerably as the dynamic range of the observed profiles is increased.

As we demonstrate in Paper I, care should be taken to adopt and test physically motivated interpretations of different functional forms that could be considered when fitting these profiles. For example, the lower left panel of Figure 1 shows the results of fitting a pure Sérsic function to

<sup>8</sup> We fit the observed points in the same manner as the simulations, weighting each point with the (quadratic) sum of the same intrinsic  $\sim 0.1$  mag point-to-point variance and the observational errors. These errors are however generally small (much smaller than the plotted points shown in the observed profiles), so weighting the data points equally gives almost identical results.



the entire surface density profile (including the central starburst component). There is a reasonable fit to the entire profile with a single Sérsic index  $n_s = 3.56$ , quite different from the Sérsic index which describes either the pre-starburst or starburst light components. Likewise, if we consider the excess light to be that light in the real profile above the prediction of the best-fit Sérsic model, we would infer only a tiny extra light fraction  $\sim 1.0\%$ . Although the fit is technically worse, with variance  $\sigma_\mu = 0.25$ , the difference is not dramatic, and by many observational standards would be considered a good fit. Clearly, however, the results do not have the same physical meaning in this case – the “extra light” determined in this manner is no longer a direct tracer of the physical starburst component. The differences grow if we add a degree of freedom and fit a “core-Sérsic” profile, of the form  $I \propto [1 + (r_b/r)^\alpha]^\gamma / \alpha \exp\{-b_n[(r^\alpha + r_b^\alpha)/r_e^\alpha]^{1/\alpha n}\}$  (e.g. Graham et al. 2003), which behaves as a single Sérsic profile outside of  $r_b$  and breaks to a power-law of slope  $\gamma$  within  $r_b$ . The lower right panel of Figure 1 shows the outcome of this fit, which is again good in a pure statistical sense, albeit worse than our best fit Sérsic+extra light fit ( $\sigma_\mu = 0.20$  mag). However, here the derived parameters are even less intuitively related to the known physical decomposition – the best fit Sérsic index is a much steeper  $n_s = 3.95$  and one actually infers that the system is a *core* galaxy, with *missing* light relative to the best-fit Sérsic profile. Furthermore, by comparison with our results in Paper I, we find that the discrepancy between the physical parameters which accurately describe the outer and starburst components and those recovered by the pure Sérsic or core-Sérsic profile fits becomes even worse when the mass fraction of starburst component is larger.

The cause of these differences is that the extra light component blends smoothly with the outer pre-starburst light profile. By increasing the central surface brightness, the extra light component makes the overall profile appear steeper (concave up in the  $\mu - r^{1/4}$  projection), owing to the rise at small  $r$ . However, the cusp itself does not continue to rise steeply inwards (in most cases), so after steepening the best-fit Sérsic index to fit the outer part of the extra light component, one is often forced to infer the existence of a core in the central regions. Again, these fits do not directly reflect the physical two-component nature of the profiles (rather reflecting some combination of the components, with the extra light no longer apparent in an excess with respect to the fit but in the higher fitted Sérsic indices), but they are not terrible matches to the light profile. *This emphasizes that a physically motivated profile must be adopted when fitting a parameterized model to the data, if one wishes to translate these parameters into robust physical properties.* Fortunately, there are some indications from observations that the Sérsic only and core-Sérsic fits are not physically motivated as a means to decompose the two-component nature of the observed systems.

First, they are technically worse fits, although the difference is not large (and in some rare cases, core-Sérsic profile is a better match to our simulations than the Sérsic+extra light profile). With photometry accurate to  $\sim 0.01$  mag arcsec $^{-2}$  it is possible to robustly distinguish the quality of the fits shown in Figure 1, especially to note the fact that the errors in the Sérsic and core-Sérsic models are a strong function of radius (an indication of the less appropriate choice of fitting function), but with the exception of Kormendy et al. (2008), our data sets do not attain such high accuracy. Second, they begin to fail at large radii – however, this is where the true nature of the

Sérsic profile of the outer light component is most prominent, so any failure at large  $r$  should be especially worrisome. Furthermore, when we examine the kinematics (e.g. ellipticity, boxy/diskyness, rotation properties) along the major axis, one can often see a transition in these properties where the extra light begins to dominate (see § 5), whereas we would expect no such change if the ability to fit a continuous Sérsic profile were taken to imply that there is only a single physical component constituting the galaxy. Finally, when fitting a core-Sérsic profile to a system with significant extra light, a large *missing* light fraction (defined as the difference between the core-Sérsic fit and the inwards extrapolation of the Sérsic portion of the fit) is sometimes seen, even relative to what is typically observed in genuine core galaxies (e.g. massive, boxy, slow-rotating ellipticals; see Kormendy et al. 2008). This is true when the dissipational component is large – but Figure 1 demonstrates that it is not always the case, so again, care must be taken to employ a physically well-motivated decomposition and interpretation.

We do not claim that a pure Sérsic or core-Sérsic profile is never a physically motivated parameterization of the galaxy light profile. However, for gas-rich merger remnants, we know from our simulations and have good reason to believe observationally that there is some excess light component. In these cases, which we investigate here, the results of these fits are demonstrably less physically intuitive and can be misleading.

We also emphasize that although there are some superficial similarities between our adopted parametric profile decomposition and that in e.g. Côté et al. (2006) and Ferrarese et al. (2006), the two are in detail significantly different and address very different spatial scales and physical properties of the galaxies. Typically, the “outer profile” we refer to extends to and beyond (in our simulations) the limits of our ground-based photometry, corresponding to physical radii of  $\sim 20 - 100$  kpc, and our “inner profile” refers to the residual from a central starburst at scales where a significant fraction of the galaxy mass becomes self-gravitating (see § 6), at  $\sim 0.5 - 1$  kpc. We stress again that we are not resolving inwards of the central  $\sim 30 - 50$  pc, and our modeling should not be extrapolated to within these radii without considerable care. In contrast, the “outer profile” in Ferrarese et al. (2006) is based on the HST ACS profiles, which extend to outer radii  $\sim 1$  kpc, and their “inner profiles” typically dominate the light profile at very small radii  $\sim 0.01 - 0.02 R_e$  ( $\sim 10 - 40$  pc for most of their sample). This is more akin to separating our “inner” component itself into multiple sub-components – i.e. a starburst stellar component that blends (as we have shown) relatively smoothly onto the outer, violently relaxed stars and an innermost nuclear component. The authors themselves address this, and denote these nuclear excesses as central stellar clusters. In Appendix C we demonstrate that such clusters are clearly distinct, orders-of-magnitude smaller objects than the starburst/extra light components we study in this paper. Such systems may indeed be present (and could be formed in the same dissipational starburst which we model): but if so they are distinct subsystems sitting on top of the starburst light component, which we do not have the ability to model or resolve in our simulations. Therefore, while the two approaches may yield complementary constraints, we caution that our results are not directly comparable and are specifically designed to trace distinct physical structures.

### 5. COMPARISON WITH OBSERVATIONS: EXTRA LIGHT IN ELLIPTICALS

We now extend our analysis to the sample of observed ellipticals and merger remnants described in § 3. Figures 3-12 show surface brightness profiles of objects in the Virgo elliptical sample of Kormendy et al. (2008), in order of most massive to least massive.<sup>9</sup> For each object, we plot the surface brightness profile with the best-fit two component model, and the corresponding fitted outer Sérsic index and extra light fraction. It is a reassuring consistency check that our fitted outer Sérsic indices agree well with those estimated independently (and with a slightly different methodology) in Kormendy et al. (2008) – i.e. accounting for the fact that the extra light is an independent component (and with sufficient dynamic range to well-resolve the outer profile), the results in most cases are not highly sensitive to the exact fitting procedure. We refer to Paper I for the same comparisons with local observed gas-rich merger remnants from Rothberg & Joseph (2004). A complete list of fit parameters and compiled galaxy properties is included in Table 1 for the ellipticals and Table 2 for the merger remnants.

We also compare each observed system with our library of simulations, in a non-parametric fashion. We do this by allowing the normalization of the simulated light profile to vary (within  $\pm 0.5$  dex), and quantifying the  $\chi^2$  (variance of the observed points with respect to the simulated light curve at  $> 1$  gravitational softening length) of each simulation. We allow the normalization to vary because we have a finite number of simulations and therefore do not sample a continuum in e.g. total brightness, but instead discretely sample at factor  $\sim 2$  intervals (we do not allow the simulated profiles to vary by more than this amount, to avoid an unphysical match to a simulation with very different total mass). We do not allow any other parameters to vary – i.e. we allow limited rescaling in the surface brightness of the simulated galaxies, but *not* their radii or other properties. Despite the allowed surface brightness rescaling, the best-fit simulations almost always have similar total luminosities to the observed system, because they must have a similar effective radius in order to be a good match. Considering  $\sim 100$  sightlines to each of our simulations (although, as noted in Paper I, the observed surface brightness profile varies by a small amount sightline-to-sightline), we find the best fit to each observed system.

In the middle panels of Figures 3-12 we show the three simulations which most closely match the observed light profile. For the best-fit simulation, we also show the profile of the stars formed in the final, central, merger-driven starburst, as described in § 4. We show in the figures the outer Sérsic indices fitted to these simulations, along with the typical range both across sightlines and across the best-fitting simulations (which together give some rough approximation to the range of  $n_s$  which might be observed for these galaxies along different sightlines). We also show the best-fit starburst mass fraction, along with the range across the best-fitting simulations (described below), and the variance of the observed points

<sup>9</sup> NGC 4382 is typically classified as a core or intermediate galaxy in the literature. We show it because it is also sometimes considered a gas-rich merger remnant, based on the presence of ripples and shells formed by cold tidal material (e.g. Hernquist & Spiegel 1992), a high fine structure index (Schweizer & Seitzer 1992), young ( $\sim 2$ Gyr old) stellar populations (Trager et al. 2000; McDermid et al. 2006), disk isophotes and high ellipticity (Kormendy et al. 2008), and rapid rotation (Emsellem et al. 2007). Excluding it from our sample, however, makes no difference to our conclusions.

with respect to the best fit<sup>10</sup>.

In addition, for these simulations we show the isophotal shape and ellipticity as a function of major axis radius, compared to that observed. Note that we do *not* fit these quantities, only the surface brightness profile. We show, for each simulation, the range across sightlines in these quantities – it is clear that these depend much more strongly on sightline than the surface brightness profile (this is primarily why we do not fit these quantities). In every case, there is a significant fraction of sightlines with shape and ellipticity profiles roughly consistent with those observed, but the simulations highlight the range of profile shapes for similar spheroids to those observed.

For the intermediate and higher mass Virgo ellipticals,  $\gtrsim 0.1 L_*$ , we easily find simulations which provide an excellent match to the observed profiles, with variance  $\sigma_\mu$  often less than even a multi-component parameterized fit. The fits are good over the entire dynamic range from the largest observed radii ( $\sim 100$  kpc) down to our resolution limits ( $\sim 30$  pc)<sup>11</sup>. At radii below our softening limits, the simulation profiles artificially flatten; but we show in Appendix B that the agreement continues down to smaller and smaller radii as we increase our resolution. At moderate and large masses, the starburst fraction recovered by our two-component fit is usually a good match to the physical starburst mass fraction in the best-fitting simulations (see § 6).

At the lowest masses  $L \lesssim 0.01 L_*$ , the fitted extra light components tend to be smaller than our simulated starbursts. This is at least in part a resolution issue, both in our simulations and in the observations (the extra light in the lowest-luminosity ellipticals is poorly resolved even with HST data). Below  $M_B \sim -18$  (i.e. roughly an order of magnitude below  $\sim L_*$ ), it is also no longer clear that the fitted extra light components are the same physical entities – some of the sharp central features in the profiles may in fact be nuclear stellar clusters, modeling of which would require resolving individual star-forming complexes in our simulations. (See Appendix C for a discussion of the differences between extra light components studied herein and the stellar nuclei studied in e.g. Côté et al. (2006) and Ferrarese et al. (2006). Those nuclear components are on much smaller scales and bear little resemblance to the starburst component we are interested in here.) The two lowest-mass “compact ellipticals” in our sample, NGC4486b and VCC1199 (Binggeli et al. 1984), with  $R_e \sim 150-200$  pc, are somewhat smaller than any of our simulated merger remnants. Given our resolution limits and limited sampling of e.g. initial disk sizes at these very low masses, it is premature to say whether some different physics (e.g. tidal stripping; Faber 1973) is needed, but the systems lie on the fundamental plane and their outer profile shapes appear normal.

Figure 13 again shows the observed and best-fit simulated surface brightness profiles, for a subset of confirmed cusp ellipticals in the sample of Lauer et al. (2007a), in order of  $V$ -band magnitude from brightest to faintest. For each simulation in our library, we have a  $\chi^2$  corresponding to its goodness of fit to the observed profile, and the genuine physical

<sup>10</sup> The values shown in Figures 3-12 are based on comparison only to the profiles shown, from Kormendy et al. (2008). In Table 1, the values represent the results from all available data sets, including multiple different observations of the systems shown here, and so can be slightly different (however the differences are generally small).

<sup>11</sup> The dynamic range of the fits is somewhat difficult to discern in Figures 3-12 owing to the plotting versus  $r^{1/4}$ ; we therefore reproduce these figures plotting  $\mu$  versus  $r$  in Appendix A.

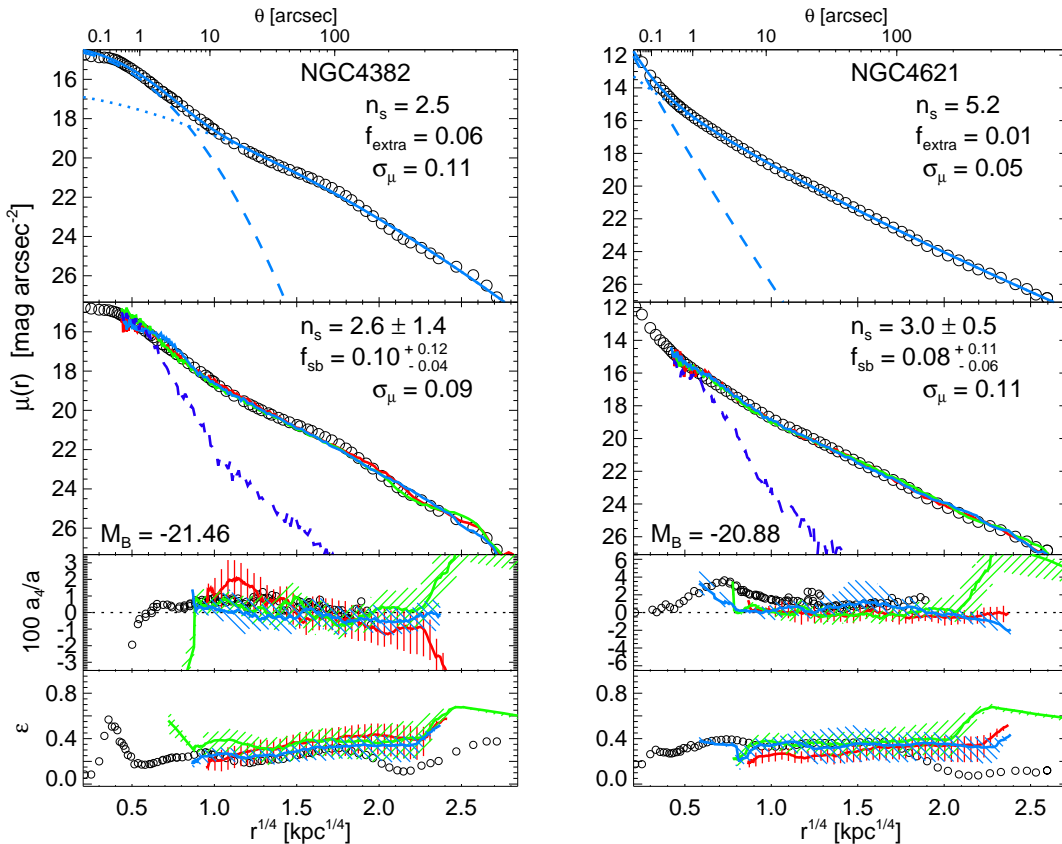


FIG. 3.— Surface brightness profiles are shown for cuspy ellipticals in the Virgo cluster. Open circles show the observations, from Kormendy et al. (2008). These are the highest-mass cusp or extra light ellipticals in Virgo<sup>9</sup> ( $\sim 2M_*$ ). *Top*: Observed V-band surface brightness profile with our two component best-fit model (solid, dashed, and dotted lines show the total, inner/extra light component, and outer/pre-starburst component). The best-fit outer Sérsic index, extra light fraction, and variance about the fit are shown. *Middle*: Colored lines show the corresponding surface brightness profiles from the three simulations in our library which correspond most closely to the observed system (shown outside to the gravitational softening length,  $\sim 30$  pc). Dashed line shows the profile of the starburst light in the best-matching simulation. The range of outer Sérsic indices in the simulations (i.e. across sightlines for these objects) and range of starburst mass fractions ( $f_{\text{sb}}$ ) which match the observed profile are shown<sup>10</sup>, with the variance of the observations about the best-fit simulation ( $\sigma_\mu$ , in  $\text{mag arcsec}^{-2}$ ). *Bottom*: Observed diskiness ( $a_4$ ) and ellipticity profiles, with the median (solid) and 25–75% range (shaded) corresponding profile from the best-fitting simulations above. Note that these are not fitted for in any sense. Figures 5–12 show the other cusp ellipticals in the sample, ranked from most to least massive.

starburst mass fraction  $f_{\text{sb}}$ . We can therefore construct a  $\chi^2$ -weighted distribution of  $f_{\text{sb}}$  for each observed system – essentially, the probability, across a uniform sample of initial conditions, that the observed profile was drawn from a simulation with the given starburst mass fraction. These are shown, and compared to the fitted extra light fraction for our two-component models. In general, the fitted extra light fraction corresponds well to the characteristic starburst mass fractions in simulations which produce similar light profiles.

There are a small number of observed objects for which detailed spectral energy distributions (SEDs) have enabled two-component stellar population models to be fit, in which there are generally an older, smoother distribution and a younger, metal-enriched single burst population (Titus et al. 1997; Schweizer & Seitzer 1998; Schweizer 1996; Schweizer & Seitzer 2007; Reichardt et al. 2001; Michard 2006). For these objects, we plot the observationally estimated mass fraction (from these studies) in the secondary burst population (the vertical red dashed lines), which we expect should correspond (roughly) to the starburst population in the spheroid-forming merger, if this is a good description of the formation history. Although there are only a few systems for which this comparison is possible, the agreement between this estimate and our inferred extra light or starburst fractions is surprisingly good. Of course, there are a

number of uncertainties and degeneracies in an attempt to observationally decompose stellar populations, but this gives us confidence that there is physical meaning to our decompositions.

## 6. PROPERTIES OF “EXTRA LIGHT” PROFILES

Having fit both our simulations and observed cuspy ellipticals to an outer violently relaxed component and an inner starburst profile, we now compare these fits as a function of galaxy properties.

### 6.1. Outer Profiles: Sérsic Indices

Figure 14 plots the outer Sérsic indices of our sample of simulations as a function of galaxy stellar mass, compared with those observed. The lack of any trend is striking – we predict that there is *no dependence of outer Sérsic index on galaxy mass for cusp ellipticals*. In fact, we have searched our entire sample of mergers attempting to find a dependence of outer Sérsic index on some galaxy property, including merger redshift, gas fraction, halo concentration, baryon fraction, and the presence or absence of initial bulges, and find no dependence. There is a weak trend with gas content, but only in the sense that systems with extremely high gas content even at late merger stages (e.g.  $\gtrsim 40\%$  gas at the time of final coalescence) can form or retain massive disks, bringing them closer

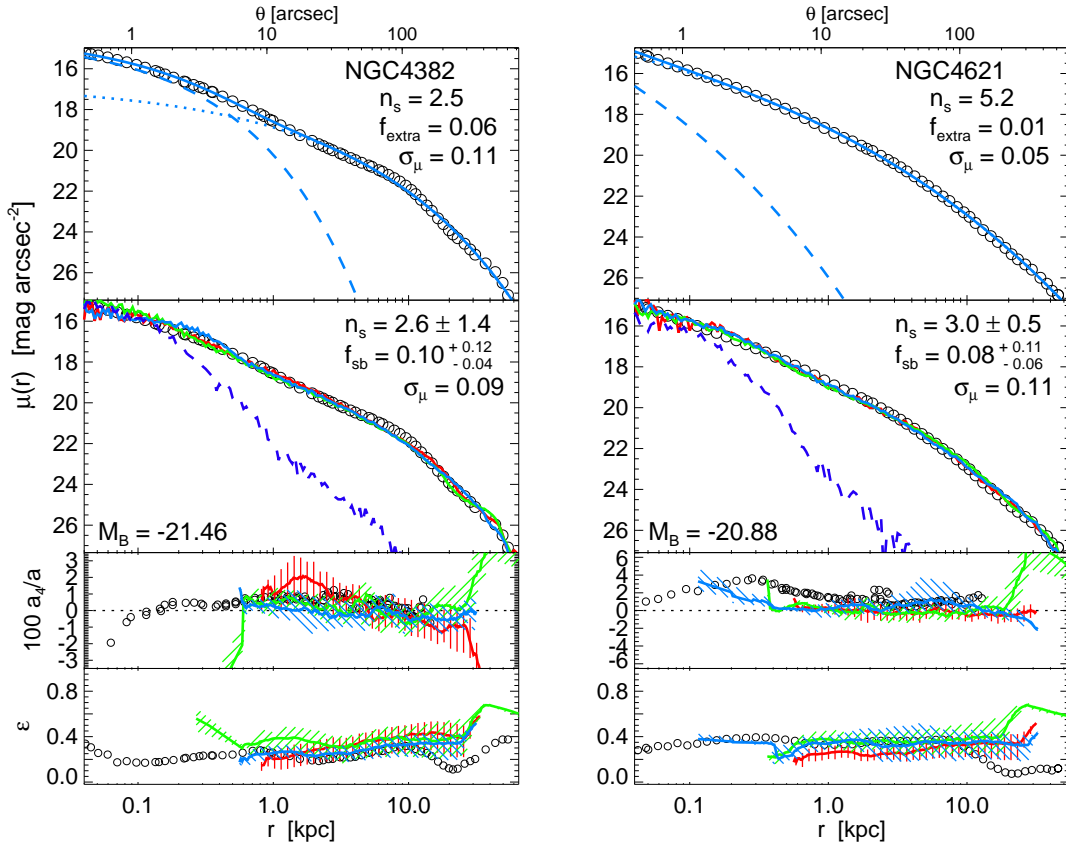


FIG. 4.— As Figure 3, but in log-log space. The two-component nature of the profiles is somewhat less obvious in this projection, but the dynamic range is more clear. We show the systems from the outermost observed radii down to our best simulation resolution limits ( $\sim 30$  pc). Over nearly four orders of magnitude in radius (and  $\sim 14$  mag in surface brightness), simulations and observed systems agree. We show all of Figures 3-12 in this projection in Appendix A.

to  $n_s = 1$ . There is also a weak dependence on orbital parameters, but only in the sense of different, extreme orbits changing the best fit outer Sérsic index by  $\Delta n_s \lesssim 1$ . The apparent difference between our low and high-redshift simulation  $n_s$  distributions is in fact entirely attributable to these effects. Similarly, Naab & Trujillo (2006) find that in simulated collisionless (gas-free) disk merger remnants – i.e. systems for which the entire profile is by definition part of the “outer,” violently relaxed component – there is also no significant dependence of the Sérsic index on mass, effective radius, or merger mass ratio.

The observations appear to confirm this prediction. Kormendy et al. (2008) see no dependence of outer Sérsic index on galaxy luminosity (within the extra light/cusp population), and our other data sets support this over a large baseline in luminosity and stellar mass (albeit with larger scatter, owing primarily to the lower quality of the data). Over more than three orders of magnitude in stellar mass, and two orders of magnitude in effective radius, the observations and simulations both show a typical  $n_s \sim 2-3$  with no dependence of outer Sérsic index on mass, luminosity, or radius in cusp ellipticals.

This prediction appears to contradict some previous results that argue for a strong dependence of Sérsic index on luminosity (Graham 2001; Trujillo et al. 2002; Ferrarese et al. 2006) or effective radius (Caon et al. 1993; Prugniel & Simien 1997). However, we emphasize that these fits are *not* directly comparable to ours. First, these correlations were found considering samples of a broad range of spheroids – from dwarf spheroidals through cuspy, rapidly rotating ellipticals through massive, cored, slowly rotating ellipticals.

Here, we are only arguing that the specific subclass of cuspy, true ellipticals formed in gas-rich mergers should have a mass-independent Sérsic index distribution. Different formation mechanisms (for example, subsequent dry mergers; Hopkins et al. 2008h) can systematically change the Sérsic index, giving rise (via cosmological trends towards more mergers in higher-mass systems) to mean correlations between Sérsic index and galaxy mass or size. To the extent that the observed Sérsic indices of the cusp population are relatively low and do not depend on mass or luminosity, it implies that they are generally formed in a small number of major mergers, without substantial subsequent re-merging.

Second, these authors were often fitting the entire galaxy light profile to a single Sérsic or core-Sérsic law, whereas we have attempted to decompose the inner and outer galaxy light profiles. This two component approach will systematically yield different Sérsic indices, and in some cases as demonstrated in § 4 the difference can be dramatic.

To check if the effect illustrated in Figure 14 is caused by large scatter in our estimates (possibly obscuring an underlying trend), we show in Figure 15 the same Sérsic index as a function of mass, but using a strict, cleaned sample. We include in this subsample only those galaxies for which  $\geq 3$  sources of photometry (or photometry in  $\geq 3$  bands) yield  $n_s$  values different by  $< 20\%$ . We exclude the recent merger remnants, for which unrelaxed features may introduce additional scatter or uncertainties. For the simulations, we plot only those with sightline-to-sightline variance less than this amount (usually eliminating those with significant tidal or unrelaxed features). The distribution and lack of dependence on mass is the same as Figure 14, but the conclusion here is more

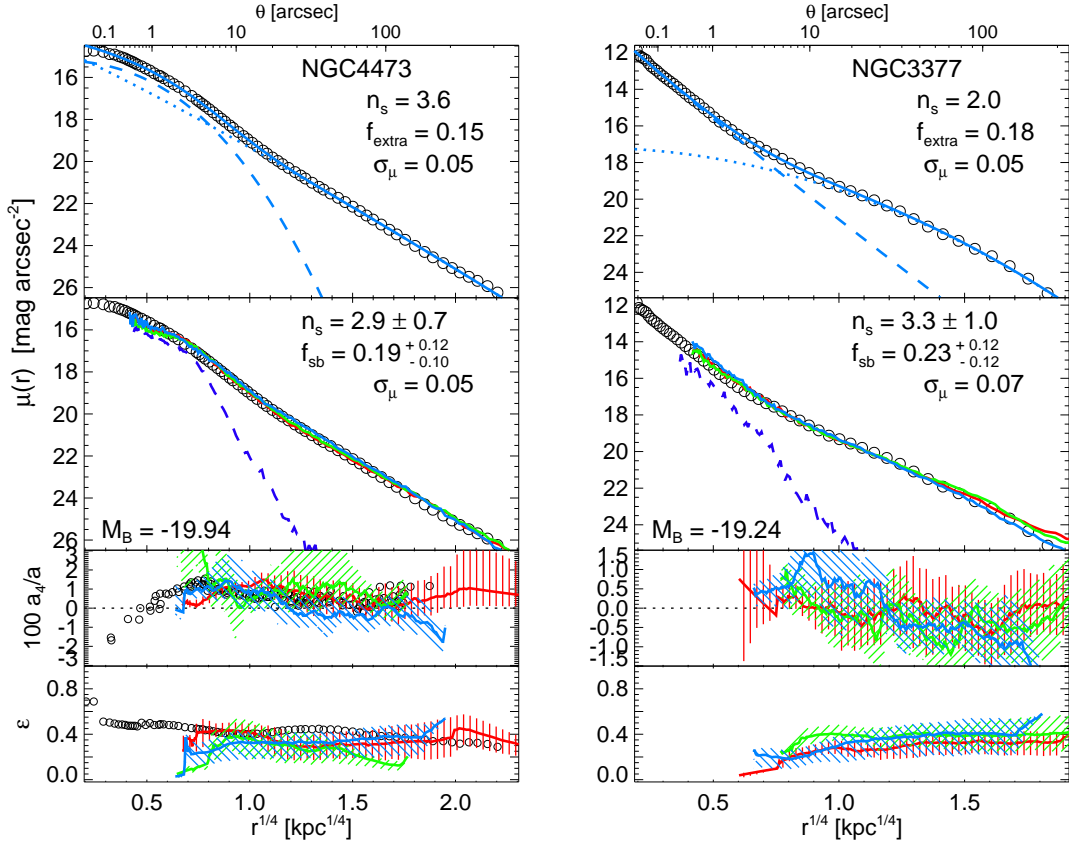


FIG. 5.— The next most massive cusp ellipticals ( $\sim 1M_*$ ). Note that NGC 3377 is not a Virgo member.

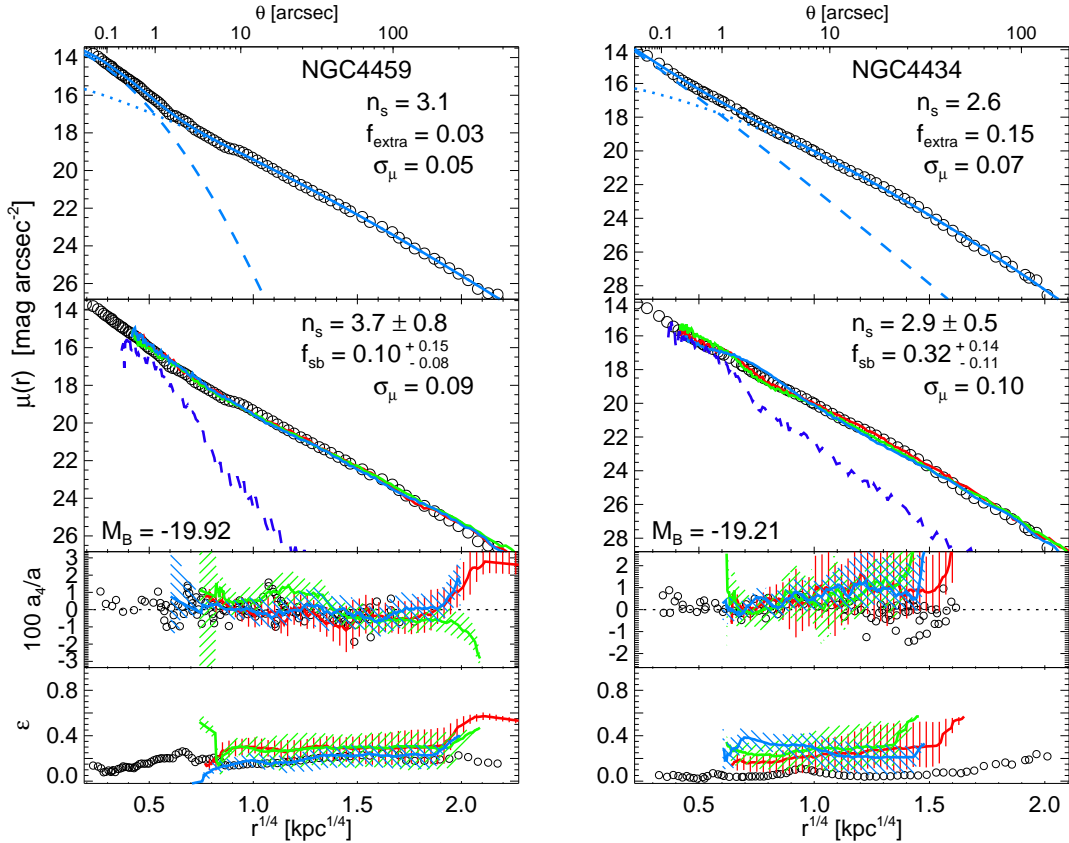


FIG. 6.— The next most massive cusp ellipticals ( $\sim 0.5M_*$ ).

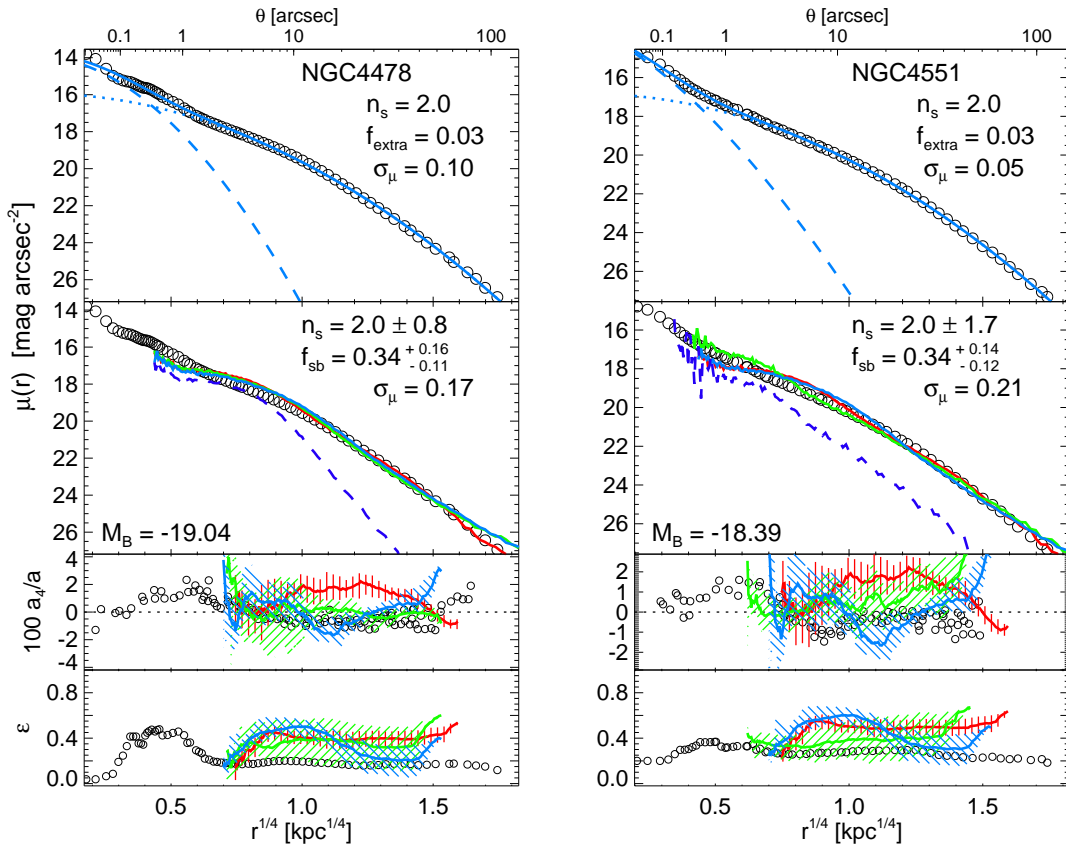


FIG. 7.— Lower-mass cusp ellipticals ( $\sim 0.2-0.3M_*$ ). Our simulations reproduce the observed outer profiles and kinematic properties of such galaxies, but do not resolve the stellar cluster nuclei at small radii. The extra light recovered by our two-component fits therefore may be misleading at such low mass.



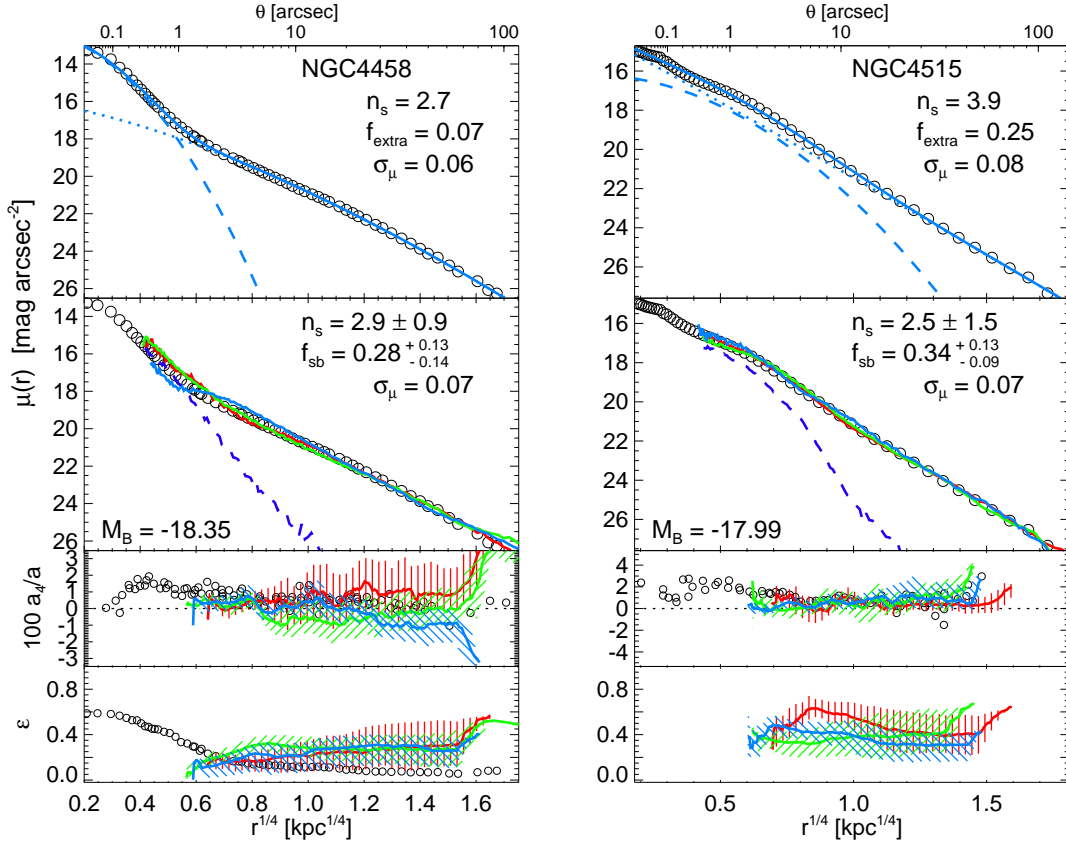


FIG. 8.— Additional low-mass ( $\sim 0.2M_*$ ) cusp ellipticals. Our fits perform better in this case.

robust.

Given that, at least for cuspy ellipticals formed in gas-rich mergers, there is no strong systematic dependence of  $n_s$  on other properties or initial conditions, it is acceptable to place all such systems on the same footing and consider the overall distribution of  $n_s$  values. Figure 16 shows this, for the simulations and our observed samples. Figure 17 shows the same, but restricted to the cleaned subsample of Figure 15. In each case, there is reasonable agreement, within the errors.

The sample of Rothberg & Joseph (2004) shows somewhat more  $n_s \sim 1$  systems than our simulations or observed cuspy ellipticals. This effect is only marginally significant, but probably arises because a few of the systems in their sample will most likely (once they are relaxed) be better classified as S0s than ellipticals. There is a tentative suggestion that our predictions are shifted to systematically higher  $n_s$  than the observed systems, by  $\Delta n \sim 0.25$  or so. At this level, however, observational issues in the measurements become important, as do the exact orbital parameters used in the simulations and the dynamic range over which the fit is performed (see e.g. Boylan-Kolchin et al. 2005). For example, Blanton et al. (2005) find that for SDSS light profiles, the observations may be biased to underestimate  $n_s$  by  $\sim 0.2-0.5$ , and are sensitive to the sky subtraction (see also Lauer et al. 2007b), consistent with the offset we see. It is therefore not surprising that the agreement is not exact. The important thing is that, with few rare exceptions ( $\lesssim 5\%$  of cases), cuspy ellipticals and gas-rich merger remnants have  $n_s < 4$  (as in Kormendy et al. 2008), i.e. are concave-down in  $\mu-r^{1/4}$  space, without a significant dependence of  $n_s$  on other galaxy properties.

## 6.2. Dissipational (“Extra Light”) Mass Fractions

Figure 18 compares our estimates of the dissipational mass fraction in the observed ellipticals: the directly fitted extra light fraction  $f_{\text{extra}}$  and inferred starburst mass fraction  $f_{\text{sb}}$  from the best-fitting simulations. For clarity we restrict to the cleaned sample from Figure 15. Our fitted decomposed extra light fraction reliably traces the inferred starburst mass fraction, with a factor  $\sim 2$  scatter similar to that predicted from our simulations (Figure 2). The starburst fraction  $f_{\text{sb}}$  itself must, in some sense, reflect the cold gas mass available in the disks just before the final merger (and we show in Paper I that this is the case) – in this physical sense, our fitted  $f_{\text{extra}}$  and inferred  $f_{\text{sb}}$  are a robust reflection of the gas content of the progenitors. Of course, changing simulation properties such as the presence or absence of an initial bulge, the concentration of the progenitor halos and disks, the presence or absence of a supermassive black hole, and the treatment of star formation and the ISM equation of state can indirectly influence  $f_{\text{sb}}$  by altering how efficiently gas is consumed and/or expelled before the final merger, and therefore how much is available to participate in the starburst. For a fixed gas mass at the time of the final starburst, however, the starburst component mass (and therefore also extra light mass, which traces the starburst) is independent of these effects.

Figure 18 also compares the results of our fitting to independent stellar population-based estimates of the starburst fraction in observed ellipticals. It is in principle possible, by studying the stellar populations in sufficient detail, to estimate the mass fraction which formed in a recent, central starburst (as opposed to the more extended quiescent star formation history), and this should provide an indepen-

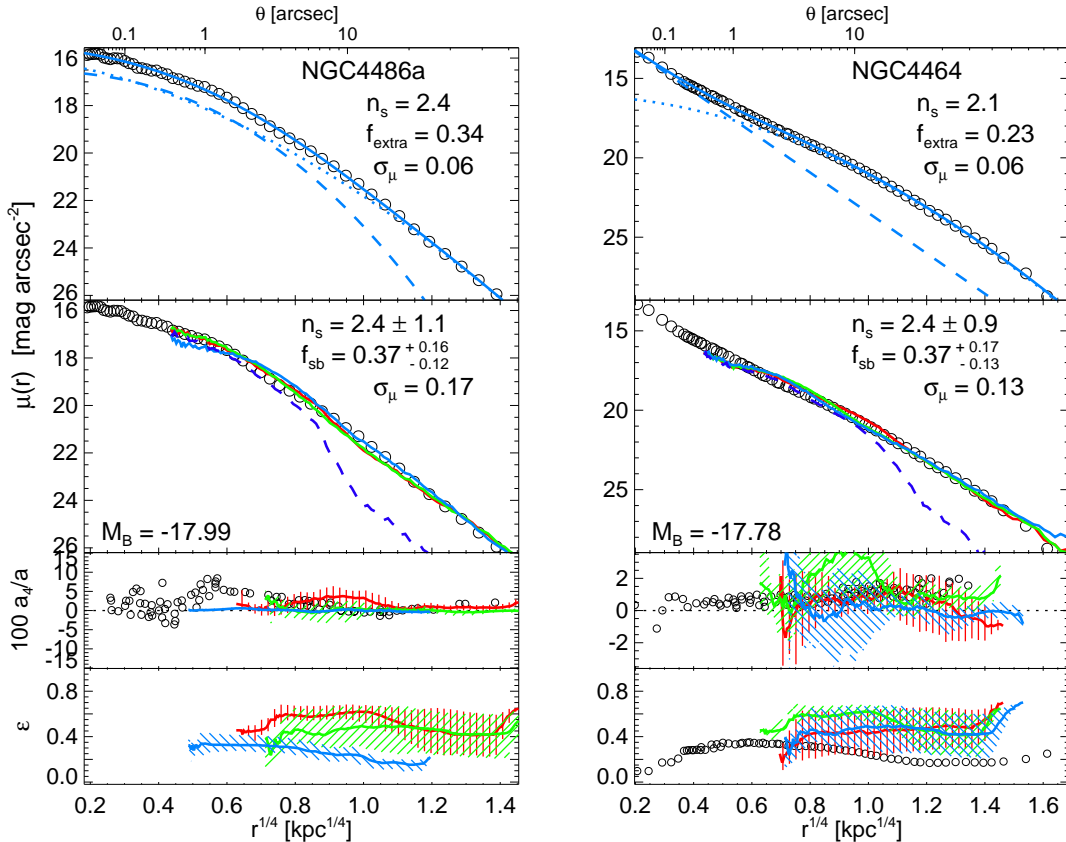


FIG. 9.— Additional low-mass ( $\sim 0.1\text{--}0.2M_*$ ) cusp ellipticals, but in this case without prominent stellar clusters in their nuclei. In this case our parameterized fitting is not misled and we recover similar starburst fractions to our simulations.

dent check of our decompositions. Unfortunately, there are still a number of degeneracies, and this requires detailed observations, but it has been attempted for several of the observed systems (Titus et al. 1997; Schweizer & Seitzer 1998; Schweizer 1996; Schweizer & Seitzer 2007; Reichardt et al. 2001; Michard 2006). Comparing our estimated  $f_{\text{extra}}$  or  $f_{\text{sb}}$  with these estimates for the mass fraction in the secondary (newly formed/starburst) stellar populations, we find a reasonable correlation. Although there are only a few objects for which sufficiently accurate stellar populations are available to allow this comparison, they all suggest that our fitted extra light component is indeed a good proxy for the mass fraction which was involved in the central, merger-driven starburst.

Having some confidence that our estimates of  $f_{\text{sb}}$  are reasonable, Figure 19 plots the inferred starburst mass fraction  $f_{\text{sb}}$  for the observed systems as a function of stellar mass. In the same manner that we have defined a best-fit  $f_{\text{sb}}$  from the best-fit simulations, we can also define a best-fit “initial” gas fraction (roughly the gas fraction  $\sim 1$  Gyr before the final merger), and show this as well. We emphasize though (for the reasons above regarding the efficiency of pre-merger gas consumption and expulsion) that this is a much less robust quantity. In either case there is a clear trend of increasing dissipation (increasing fractional mass required in a dissipational starburst component) at lower masses. The significance of the correlation is unambiguous ( $> 8\sigma$ ). We can conveniently approximate the trend in dissipational mass fraction as a function of stellar mass with the fitted function

$$\langle f_{\text{starburst}} \rangle \approx \left[ 1 + \left( \frac{M_*}{10^{9.15} M_\odot} \right)^{0.4} \right]^{-1}, \quad (3)$$

with roughly a constant factor  $\sim 2$  intrinsic scatter at each mass.

Admittedly, the estimation of this trend requires some comparison with our simulations, and one might argue that perhaps it is driven by some deficiency in them. However, we can repeat this exercise with the empirically fitted extra light component  $f_{\text{extra}}$ , and show the results in Figure 20. The trend seen in  $f_{\text{extra}}(M_*)$  is completely consistent with that in  $f_{\text{sb}}$ , but with a scatter larger by a factor  $\sim 2$  (exactly what we expect, based on the predicted and observed scatter in  $f_{\text{extra}}(f_{\text{sb}})$ ). Considering just the data in Figure 20, even given its increased scatter, the trend of decreasing extra light fraction with mass is significant at  $> 5\sigma$ . We have experimented with alternative, non-parametric (albeit less accurate) estimators based on e.g. the concentration indices or stellar populations of our simulations and observed systems, and obtain a similar answer. In short, even without reference to our simulations, however we derive an estimate of the dissipational component, it is difficult to escape the conclusion that it is more prominent in lower-mass ellipticals. This confirms a long-standing expectation of the merger hypothesis that if spirals are indeed the progenitors of ellipticals, more dissipation is required in lower mass systems in order to explain their densities and fundamental plane correlations (we examine this in more detail in Hopkins et al. 2008a).

This, in fact, should be expected. It is well-established that the gas fractions of spirals are strongly decreasing functions of mass, at any given redshift. To the extent that these are the progenitors of the cusp ellipticals, then, the amount of dissipation involved in the formation of ellipticals should reflect this trend. We therefore compare in Figure 19 the range of ob-

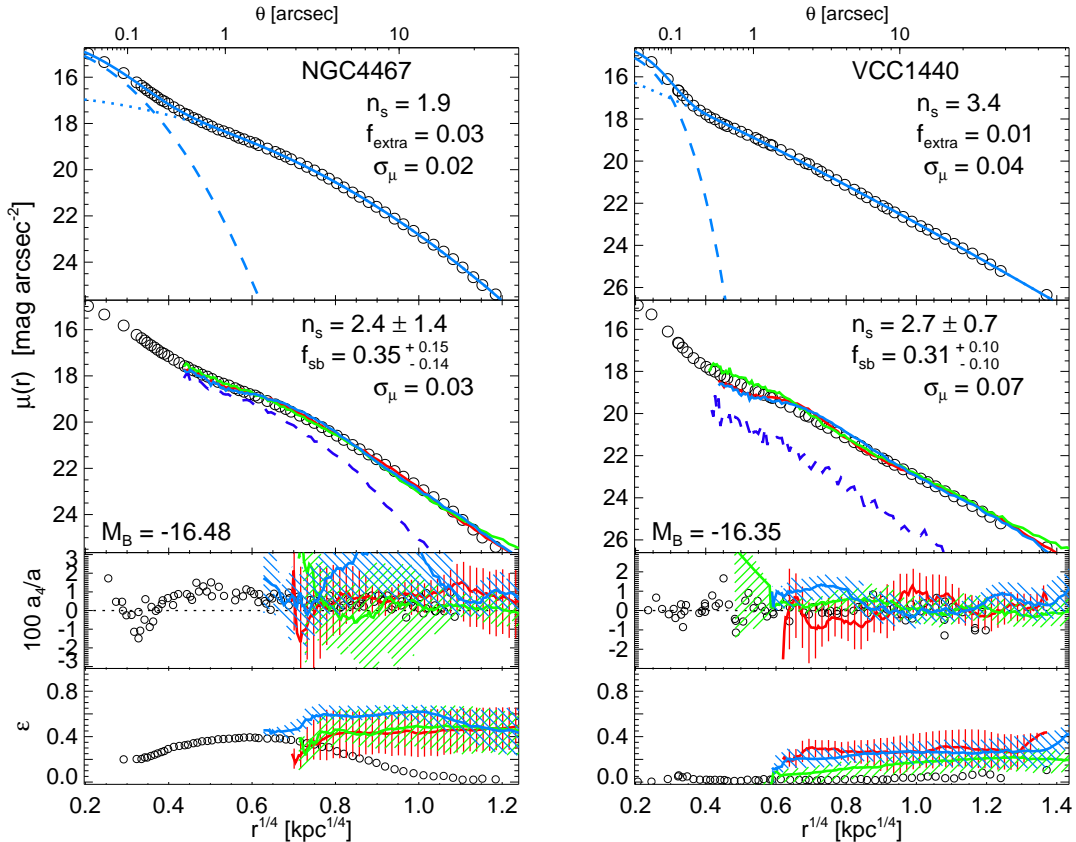


FIG. 10.— Very low-mass cusp ellipticals ( $\sim 0.03\text{--}0.1M_*$ ). Our simulations provide less good matches at these luminosities, where dwarf galaxies dominate the spheroid population (ellipticals at these masses are very rare). Robustly resolving the extra light in these very small systems probably requires  $\lesssim 10\text{pc}$  spatial resolution.

served gas fractions of spirals as a function of baryonic mass, estimated at  $z = 0$ ,  $z = 1$ , and  $z \sim 2\text{--}3$ . The gas fractions follow, at each redshift, a similar trend to that we find for the dissipational fractions of the observed ellipticals. They do, as expected for almost any reasonable cosmological history, increase systematically with redshift, and the typical disk gas fractions at  $z = 0$  and  $z \sim 2\text{--}3$  appear to roughly bracket the low and high end of the dispersion in the inferred elliptical progenitor gas fractions.

In other words, the distribution in progenitor gas fractions implied by the elliptical surface brightness profiles is, as a function of mass, exactly what would be predicted if one assumes that the progenitors were spirals, and that most of the systems were formed by a major merger sometime between a redshift of  $\sim 0\text{--}3$ <sup>12</sup>. Indeed, this is exactly what is inferred for the formation times of cusp ellipticals from both observations of the early-type or red galaxy mass functions (Bundy et al. 2006; Borch et al. 2006; Fontana et al. 2006; Hopkins et al. 2006c, 2008b), from direct stellar population synthesis studies (Trager et al. 2000; Thomas et al. 2005; Gallazzi et al. 2005), and by association of elliptical galaxy formation with the triggering of quasar activity (e.g. Hopkins et al. 2006a, 2007d, 2008f).

### 6.3. Size of the “Extra Light” Component

<sup>12</sup> Technically the post-merger elliptical mass is not exactly the mass of a single initial spiral, but correcting for this amounts to a small horizontal shift of the disk and elliptical points relative to one another in the figure (i.e. the disk points should be shifted by 0.3 dex to larger masses if all mergers are 1 : 1, or 0.1 dex for more likely 3 : 1 mergers), and does not change our comparison (in fact it makes the agreement slightly better).

The extra light components in simulations and cusp ellipticals also appear to follow a similar size-mass relation, shown in Figure 21. The correspondence is especially close if we consider simulations with initial gas fractions  $\sim 0.2\text{--}0.4$ , which tend to be the best analogs to the observed systems. This radius is the effective radius of the fitted inner extra light component, and is not the radius at which the system appears to deviate from the outer Sérsic law (but is more physically robust). We do not see simulations with extra light effective radii  $\ll 100\text{pc}$ , corresponding to the smallest extra light components seen in the very low-mass observed systems, but as discussed in Appendix B, this probably owes to our resolution limits.

In Paper I we show that the size-mass relation is driven by the condition that the gas collapsing into the central regions in the final starburst becomes self-gravitating, i.e. that  $(GM_{\text{extra}}/R_{\text{extra}}) \sim (GM_*/R_e)$  in terms of the extra light mass and effective radius. We show that the observations obey a similar condition, with (small) scatter and dynamic range similar to that in our simulated mergers. That observed systems follow a similar correlation suggests both that we are at least roughly capturing the most relevant physics determining the scales of extra light, and that we are not being severely biased by resolution effects over most of the mass range of interest.

## 7. IMPACT OF “EXTRA LIGHT” ON GALACTIC STRUCTURE

### 7.1. Galaxy Sizes and the Fundamental Plane

Figure 22 shows how, at fixed mass, the effective radius (of the entire elliptical profile) scales with extra light mass. We consider three mass bins, below, at, and above  $\sim M_*$ . In each, we plot  $R_e$  relative to that expected for the given stellar mass,

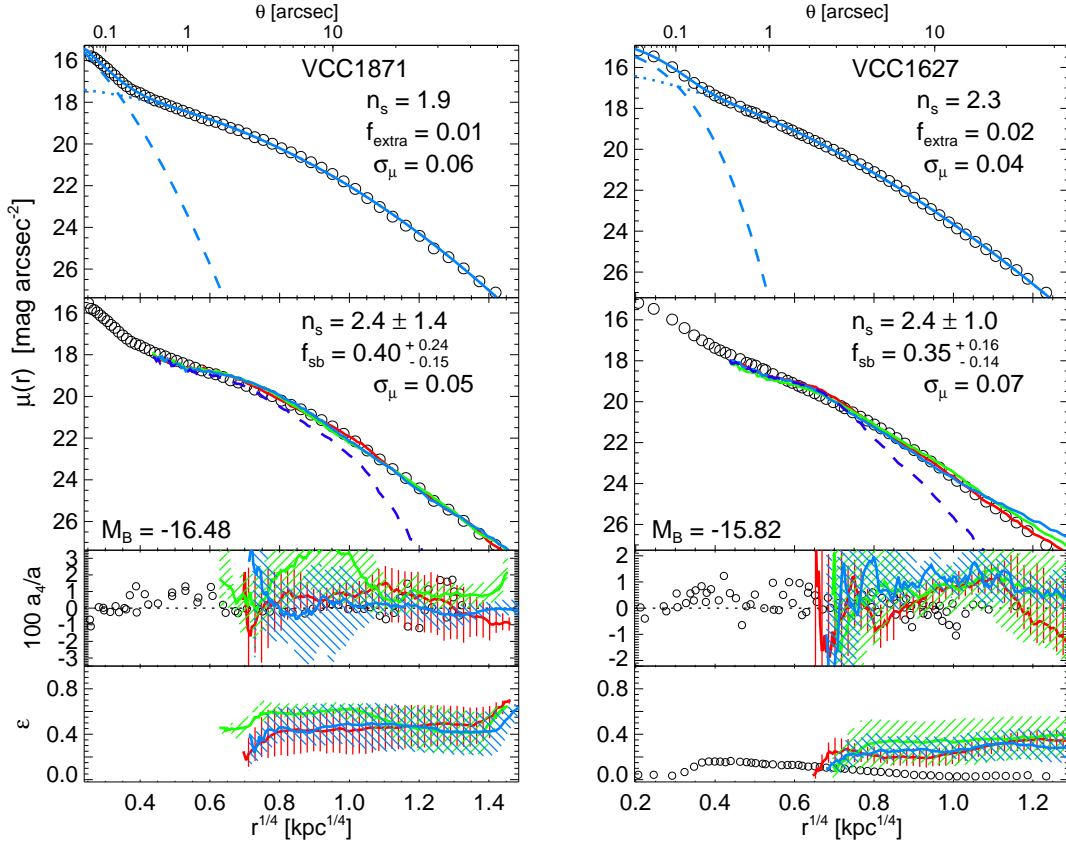


FIG. 11.— The lowest-luminosity cusp ellipticals in Virgo ( $\sim 0.01 M_*$ ). The comparison with our simulations is similar to Figure 10.

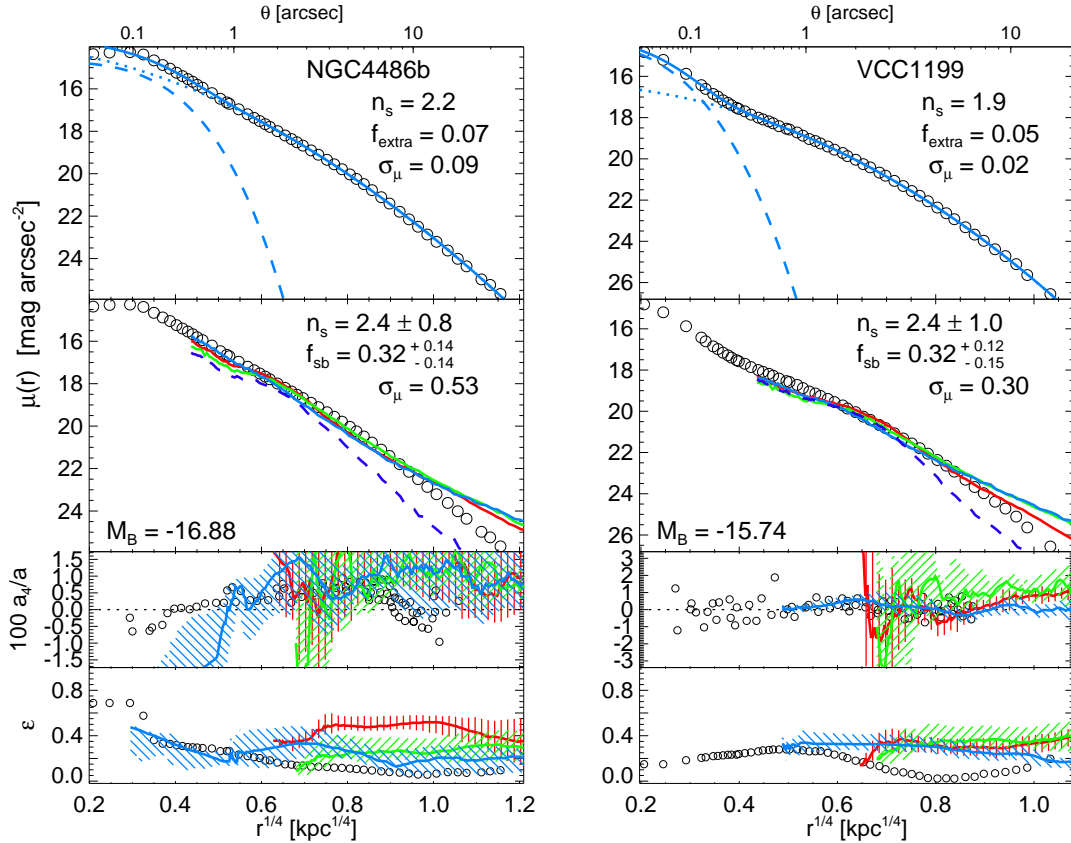


FIG. 12.— “Compact ellipticals.” None of our simulations are as compact as these objects (effective radii  $\sim 200$  pc).

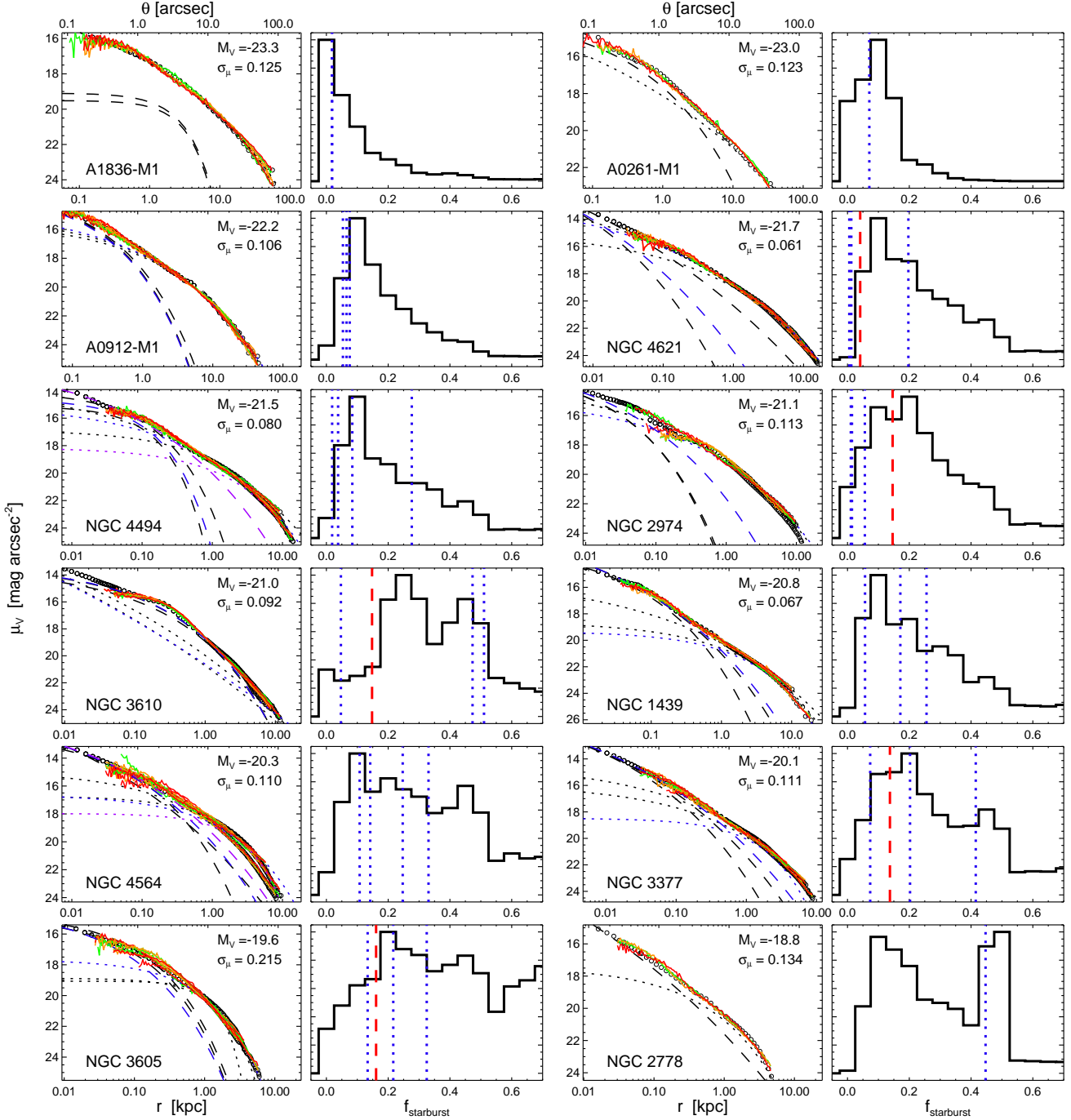


FIG. 13.— Observed surface brightness profiles of a subset of the confirmed cuspy ellipticals from the sample of Lauer et al. (2007a), with the best-matching two component parameterized fit (dashed and dotted lines) and best-fitting simulations (red, orange, and green lines), as in Figure 3. Where multiple sources of photometry are available, independent fits to each are shown. The objects are ranked from brightest to faintest in  $V$ -band (as shown). Profiles are shown over a constant angular scale (top axis; bottom axis shows physical radius in kpc). The corresponding (right) panel for each shows the distribution of physical starburst fractions for the simulations which provide a good fit to the observed profile (as described in the text), with the fitted (parameterized) extra light fraction (blue dotted line; one for each source of photometry). Where available, red dashed lines show the mass fraction of a secondary (recent) starburst population independently estimated from stellar population studies in other works. Our simulation resolution limits do not extend within the central  $\sim 30$ – $50$  pc, and their fits are not intended to describe these radii.



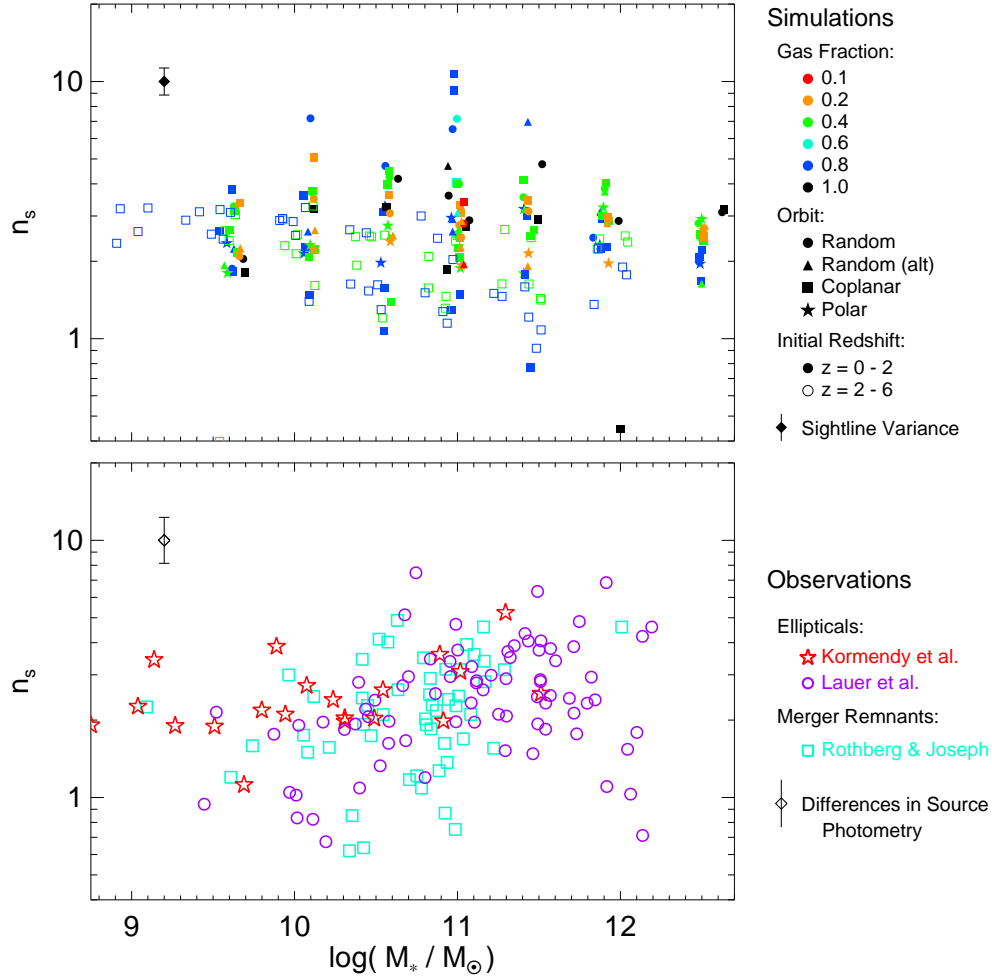


FIG. 14.— Outer Sérsic indices in cuspy ellipticals and simulated gas-rich merger remnants, using our two-component decomposition. Gas-rich merger remnants have characteristic  $n \sim 2-3$ , without a strong systematic dependence on mass or other properties. *Top*: Simulations: color encodes gas fraction, symbol encodes orbital parameters (the two “random” orbits are two different common random orbits, one somewhat closer to prograde, the other – “alt” – somewhat closer to polar), and filled/unfilled encodes the initial redshift of the simulations (as in plotted key). The plotted  $n_s$  is the median across  $\sim 100$  sightlines, typical sightline-to-sightline differences are shown as the filled plotted error bar. *Bottom*: Open colored points are observed systems: red stars are the cusps in the Virgo elliptical sample of Kormendy et al. (2008), purple circles the confirmed cusps in the local elliptical sample of Lauer et al. (2007a) (supplemented by the sample of Bender et al. (1988)), and cyan squares are the gas-rich merger remnants from Rothberg & Joseph (2004). Open plotted error shows the typical differences in  $n_s$  derived from different sources of photometry and/or different observed wavelengths. We use this point notation throughout.

as a function of the fitted extra light fraction. Specifically, we determine  $\langle R_e(M_*) \rangle$  from the sample of Shen et al. (2003), and take the ratio of the half mass radius of each system (determined directly from the light profile, or from the fits, it does not change the comparison) to that value. Our mass bins are small enough, however, that this makes little difference compared to just e.g. considering  $R_e$  in a given bin. There is a strong trend: at a given stellar mass, systems with larger extra light have systematically smaller  $R_e$  (they also have slightly larger velocity dispersion  $\sigma$ , although the scatter is larger there in both simulations and observations). In each case, the simulations and observed systems occupy a similar locus. We can also construct this plot with the starburst mass fraction  $f_{sb}$  of the best-fitting simulation as the independent variable, and find an even tighter correlation of the same nature.

This directly implies some structural change (some subtle non-homology, albeit not necessarily traditional structural or kinematic non-homology) in the fundamental plane tilt. At fixed mass, smaller systems are so because a larger fraction of their mass is formed in a central dissipational starburst. This dissipational starburst is compact, so even though the

pre-existing stars are scattered to large radii, the effective radius is smaller.

Given two progenitors of known size and mass, it is straightforward to predict the size of the remnant of a dissipationless merger, simply assuming energy conservation (see e.g. Barnes 1988); in the case of a dissipative merger, we can very crudely model the results in Figure 22 by assuming the non-extra light stars follow a Hernquist (1990) profile with effective radius  $R_e(f_{sb} = 0)$ , and the extra light is all at  $r = 0$ . More accurately, Covington et al. (2008) use the impulse approximation to estimate the energy loss in the gaseous component, followed by collapse in a self-gravitating starburst. This yields a detailed approximation as a function of e.g. initial structural and orbital parameters, but if we assume typical progenitor disks and parabolic orbits, it reduces to the remarkably simple approximation

$$R_e \approx \frac{R_e(f_{sb} = 0)}{1 + (f_{sb}/f_0)}, \quad (4)$$

where  $f_0 \approx 0.25-0.30$  and  $R_e(f_{sb} = 0)$  is the radius expected for a gas-free remnant. We plot this in Figure 22, with the



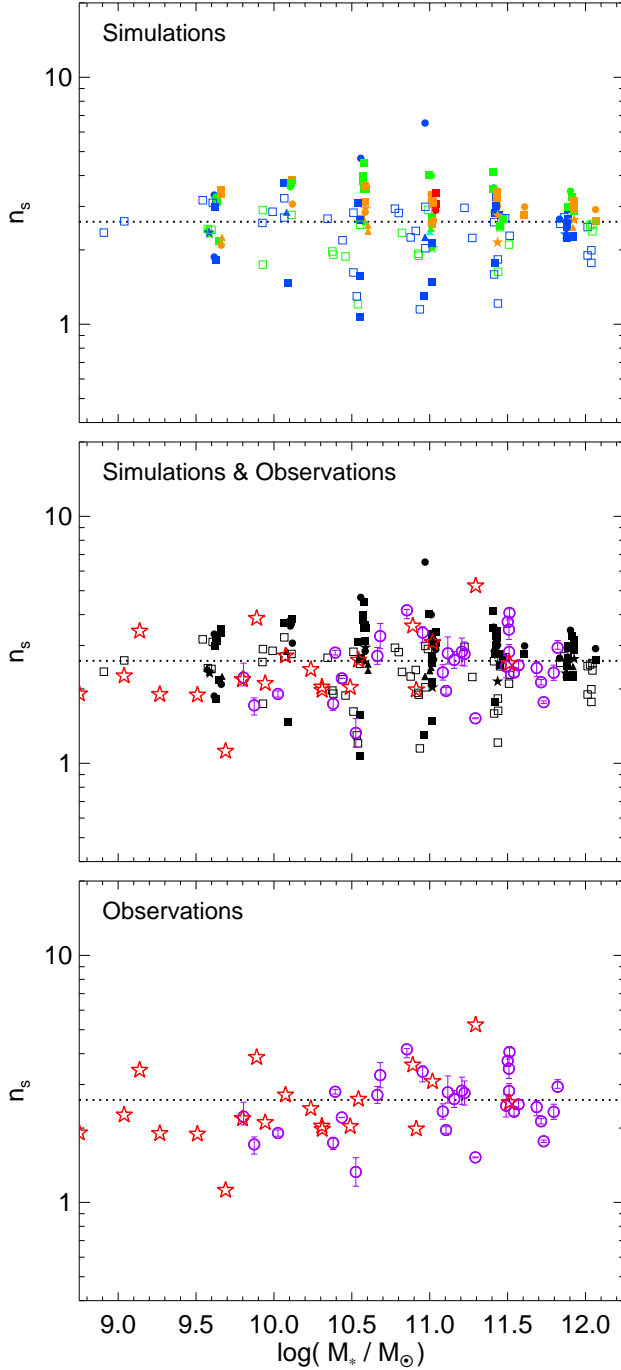


FIG. 15.— As Figure 14, but using a cleaned sample: we include only those galaxies for which  $\geq 3$  sources of photometry (or photometry in  $\geq 3$  bands) yield  $n_s$  values different by  $< 20\%$ . For the simulations, we plot only those with sightline-to-sightline variance less than this amount (usually eliminating those with significant tidal or unrelaxed features). Dotted line shows the median  $n_s \sim 2.6$ . The distribution and lack of dependence on mass is the same as Figure 14, but the results here are more robust.

scatter seen in the simulations. At all masses, in both simulated and observed cuspy ellipticals, more dissipational ellipticals are smaller in the manner predicted. In the absence of dissipation, the stellar light of observed systems would follow a uniform virial relation, but dissipation results in smaller  $R_e$  at fixed stellar mass, and (given the concentration of mass in this central starburst) therefore a higher baryon fraction inside  $R_e$  – i.e. changing the total  $M/L$  (total dark matter plus stellar

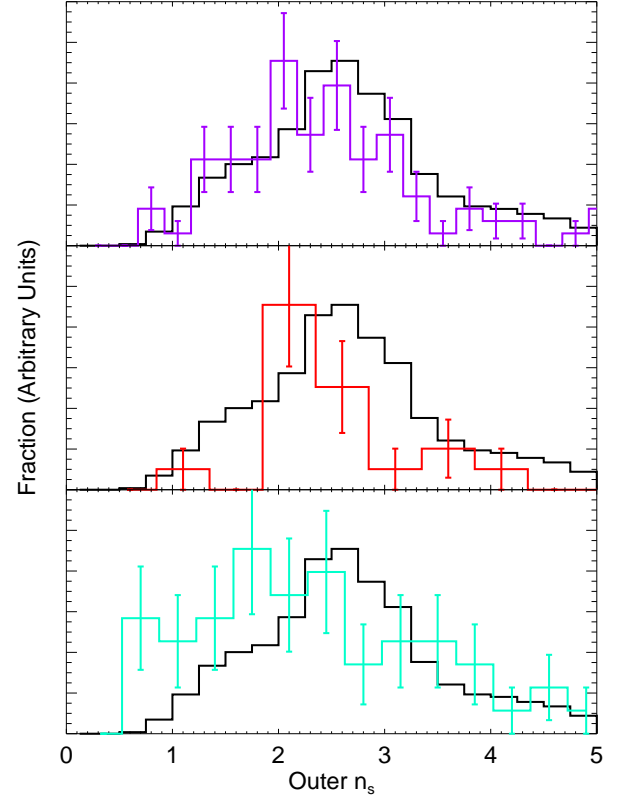


FIG. 16.— Distribution of outer Sérsic indices in cuspy ellipticals, using our two-component decomposition. Solid black line shows the result for our entire sample of simulations (each across  $\sim 100$  sightlines). Colored lines show the results for the observed samples of Lauer et al. (2007a) (top), Kormendy et al. (2008) (middle), and Rothberg & Joseph (2004) (bottom), with Poisson error bars. Rothberg & Joseph (2004) include some likely S0s, yielding a larger fraction of  $n = 1$  systems. Cuspy ellipticals have a fairly narrow range of  $n \sim 2.50 - 2.75 \pm 0.75$ , in good agreement with gas-rich merger simulations.

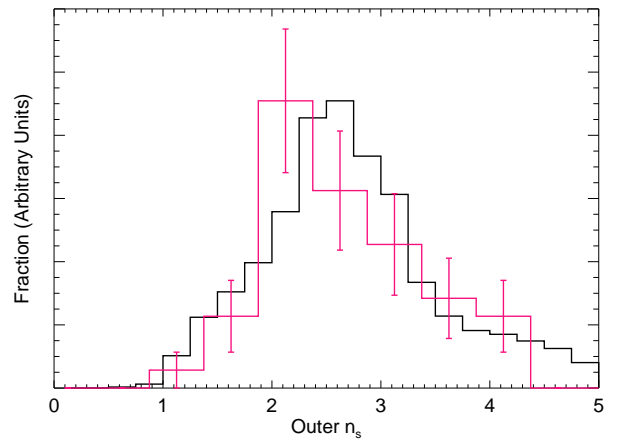


FIG. 17.— As Figure 16, but for the robust cleaned sample of Figure 15.

mass to stellar mass ratio) within  $R_e$  of the stellar light (see, e.g. Kormendy & Gebhardt 2001).

We directly illustrate this homology-breaking in Figures 23-25, by considering the light profiles of systems in Figure 22, along the correlation between  $R_e$  and  $f_{\text{extra}}$  at fixed stellar mass. We consider the  $\sim M_*$  mass bin (the other two give similar results, but have fewer observed systems), and identify four regions in the  $R_e - f_{\text{extra}}$  space along the mean

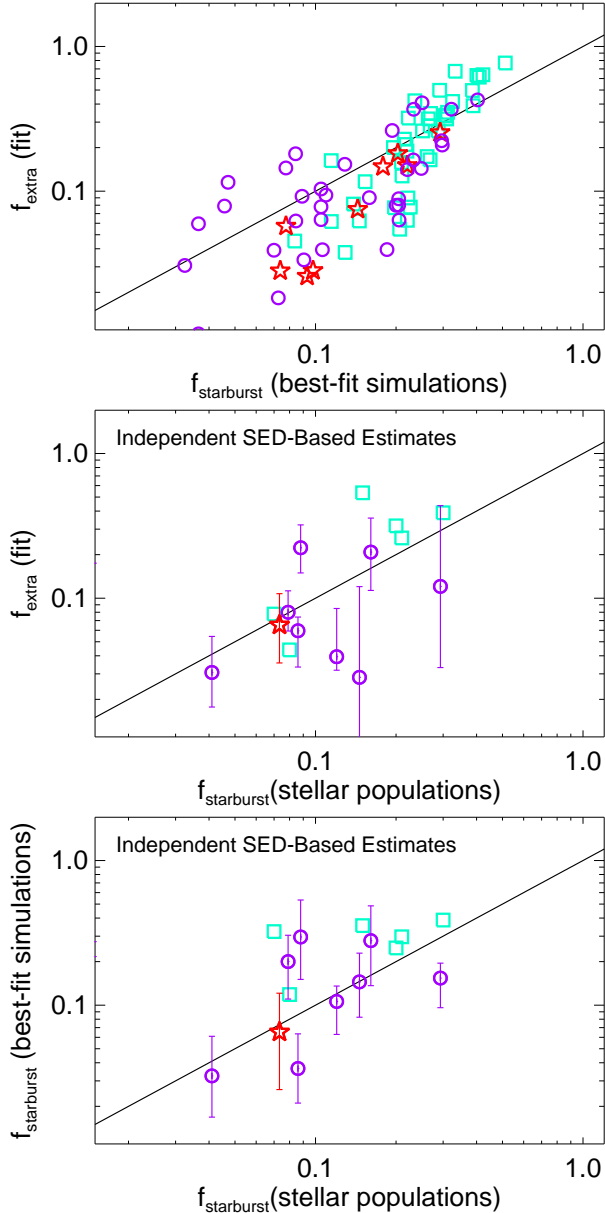


FIG. 18.— *Top*: Comparison of our estimated mass in the fitted extra light component ( $f_{\text{extra}}$ ) versus the starburst mass fraction in the best-fitting simulations ( $f_{\text{sb}}$ ; as in Figures 3-13). For clarity, we show only observations from our “cleaned” sample and where it would be possible for our simulations to resolve the extra light. In these cases, the two estimates agree well, with a factor  $\sim 2-3$  scatter in  $f_{\text{extra}}(f_{\text{sb}})$  (similar to what we expect from our simulations; see Figure 2). *Middle*:  $f_{\text{extra}}$  versus independent observational estimates of the mass fraction formed in a more recent starburst/star formation event, from two-component stellar population model fits to the observed SEDs (Titus et al. 1997; Schweizer 1996; Schweizer & Seitzer 1998, 2007; Reichardt et al. 2001; Michard 2006) *Bottom*: Same, but comparing the stellar population estimates to  $f_{\text{sb}}$  from the best-fitting simulations. More observations are needed to independently test our estimates, but the stellar population data independently suggests our decompositions are reasonable.

correlation, highlighted in Figure 23. We then plot the simulated (Figure 24) and observed (Figure 25) light profiles in each region. We also plot an  $n_s = 3$  Sérsic profile, which provides a good fit (in the mean) to most of the outer Sérsic profiles in this mass range.

It is clear in Figure 25 that both simulated and observed systems at fixed mass with the largest  $R_e$  show profiles close to a pure Sérsic law, with little evidence for any extra light

component in their centers (indeed, they have  $f_{\text{sb}} \lesssim 0.03$ ). The observed systems in this regime are still cusps, but the cusps tend to be prominent at very small radii and (in several cases) somewhat shallow, and contribute negligibly to the stellar mass. However, moving to smaller  $R_e$ , deviations from a Sérsic law at  $r \ll R_e$  become more prominent. That is not to say that these deviations are universal (that the extra light always takes the same shape/form), but there are increasingly prominent central light concentrations. If the systems were strictly homologous, there should be no differences in Figure 25. Since we have scaled each system at its  $R_e$ , they should be identical – instead, it appears that a central light concentration, formed in our simulations via gas dissipation, drives an important non-homology.

We discuss this in Hopkins et al. (2008a), where we show that this is sufficient to explain the tilt of the (stellar mass) fundamental plane. In that work, we demonstrate that the fitting of the central component in the light profile can be used as a direct observational test for the role of dissipation in the fundamental plane. Given a larger central light component, the effective radius of the stellar light profile must be smaller. Because the central regions of the galaxy are the most baryon-dominated, moving the effective radius inwards results in a different (larger) ratio of stellar to dynamical mass, i.e. driving tilt in the fundamental plane. We note that although this is technically non-homology (i.e. the profiles are not perfectly self-similar), it does not drive tilt in the sense of traditional structural or kinematic non-homology; i.e. the practical “homology assumption” that the true mass enclosed in  $R_e$  is proportional to the dynamical mass estimator  $\sigma^2 R_e / G$  remains true. Rather, the non-homology induced is a subtle effect that provides a tracer of dissipation, which changes the physical ratio of baryonic to dark matter within  $R_e$ .

## 7.2. Galaxy Shapes and Kinematics

Figure 26 shows how the shapes and global kinematic properties vary with extra light. We plot the rotation, isophotal shapes, and ellipticity of our simulations and the observed systems as a function of the fitted extra light fraction. Here, we consider the global properties of the galaxy – namely the rotation  $(V/\sigma)^*$  measured within  $R_e$ , and boxy/diskyness  $100a_4/a$ , and ellipticity  $\epsilon$  measured for the half-mass projected ( $R_e$ ) isophotal contour, for each of  $\sim 100$  lines-of-sight to the remnant uniformly sampling the unit sphere (i.e. representing the distribution across random viewing angles). The details of the fitting for our simulations are described in Cox et al. (2006b), and for the observations in Bender et al. (1987); Bender (1988); Bender et al. (1992); Faber et al. (1989); Simien & Prugniel (1997, 2002). We define rotation in the standard manner, relative to that of an oblate isotropic rotator, with the parameter  $(V/\sigma)^*$ , defined using the maximum circular velocity  $V_c$ , velocity dispersion within  $R_e$ , and ellipticity as (Kormendy 1982)

$$(V/\sigma)^* = (V/\sigma) / \sqrt{\epsilon/(1-\epsilon)}. \quad (9)$$

We exclude the coplanar merger simulations from our comparisons here: those simulations are idealized perfectly coplanar prograde orbits, and as such produce pathological orbit and phase structure (we do, however, include some more representative orbits in that are not far from coplanar).

In each sense, the simulations and observations occupy a similar locus. While there are no real correlations, there are some broad differences between the distributions for systems with

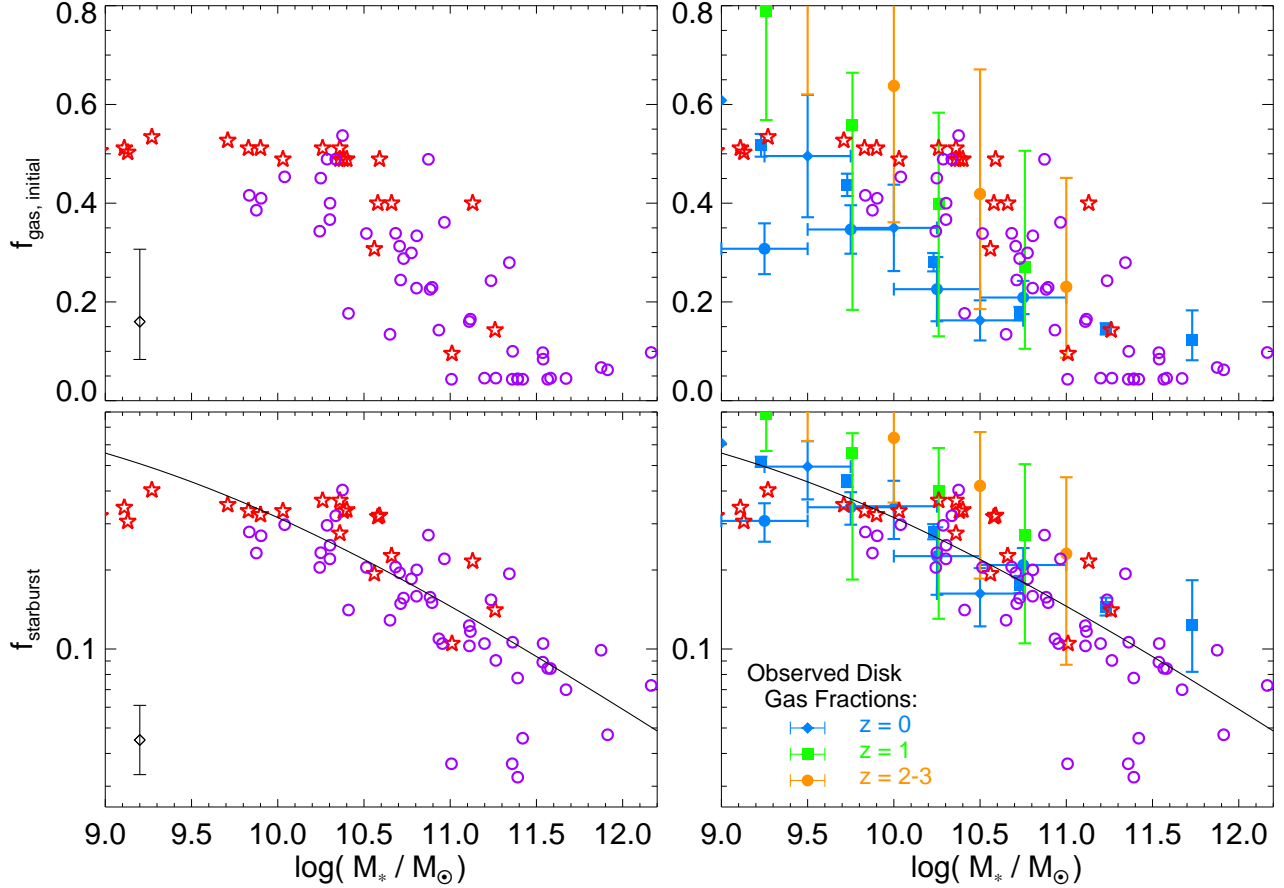


FIG. 19.— Inferred gas content (dissipational/starburst fraction) of elliptical-producing mergers as a function of stellar mass. Initial gas fraction (*top*) and physical final starburst mass fraction (*bottom*) corresponding to the best-fit simulations to each observed system in the samples of Lauer et al. (2007a) (circles) and Kormendy et al. (2008) (stars) are shown, with the typical 25–75% allowed range (error bar). Solid line shows the fit to the data (Equation 3). Colored points with error bars indicate the mean (and  $\pm 1\sigma$  range in) disk gas fractions at the same stellar mass, at  $z=0$  (Bell & de Jong 2001; Kannappan 2004; McGaugh 2005, blue diamonds, squares, and circles, respectively),  $z=1$  (Shapley et al. 2005, green squares), and  $z=2$  (Erb et al. 2006, orange circles). There is a clear trend of increasing dissipation required to explain elliptical profiles at lower masses (significant at  $> 8\sigma$ ), in good agreement with the observed trend in progenitor disk gas fractions over the redshift range where cusp ellipticals are formed, and with what is invoked to explain the observed densities and fundamental plane correlations of ellipticals (e.g. Kormendy 1989; Hernquist et al. 1993).

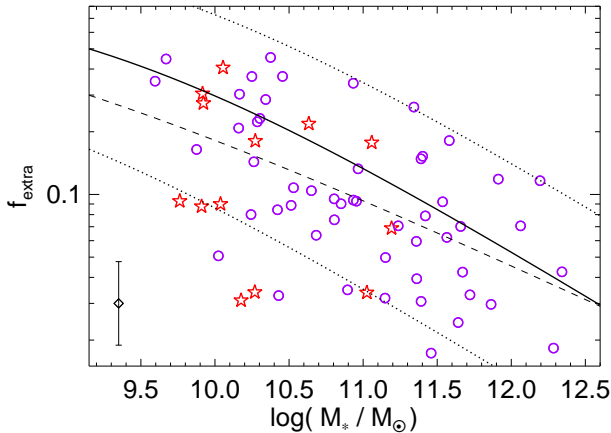


FIG. 20.— As Figure 19, but showing our empirically fitted  $f_{\text{extra}}$  as a function of stellar mass. The trend of increasing dissipation at lower masses is still clear and is consistent with that in Figure 19, but with an expected extra factor  $\sim 2-3$  scatter from the scatter in our purely empirical estimator. Solid line shows the best-fit from Figure 19, dotted lines show the  $\pm 1\sigma$  scatter expected based on the scatter in  $f_{\text{extra}}(f_{\text{sb}})$  (see Figure 2). Dashed line is a fit just to these data (statistically consistent with the solid line, and ruling out no dependence of dissipation on mass at  $> 5\sigma$  confidence).

significant or insignificant extra light components. Systems with small extra light fractions ( $f_{\text{sb}} \lesssim 0.1$ ) have a wide range of  $(V/\sigma)^*$ ,  $a_4/a$ , and  $\epsilon$  – they range from relatively slow rotation (albeit not as slow as many core elliptical slow rotators; see Emsellem et al. 2007) to rotationally supported objects  $(V/\sigma)^* \gtrsim 1$ , with both boxy and disk-like isophotal shapes ( $-2 \lesssim 100a_4/a \lesssim 2$ ), and a range in ellipticity from fairly spherical to highly flattened  $\epsilon \sim 0.5$ . Despite in some instances having e.g. slow rotation properties, these systems do not follow other trends of massive, cored slow rotators – they usually are not simultaneously slowly rotating, boxy, and round. This is similar to several observed systems, which generally show evidence for formation in a gas-rich merger but owing to sightline effects may be deviant in one of these properties.

At high extra light fractions, however, both our simulated systems and those observed tend to be more rapid rotators (fractionally more populating  $(V/\sigma)^* \gtrsim 0.4$ ), with less boxy isophotal shapes (typical  $-0.5 \lesssim 100a_4/a \lesssim 2$ ), and slightly rounder ellipticities ( $\epsilon \lesssim 0.4$ ; note they are still more elliptical than core galaxies, in agreement with observed trends). A more detailed analysis of the role of central mass concentrations and dissipation in shaping the orbital structure of gas-rich merger remnants will be the focus of Hoffman et al.

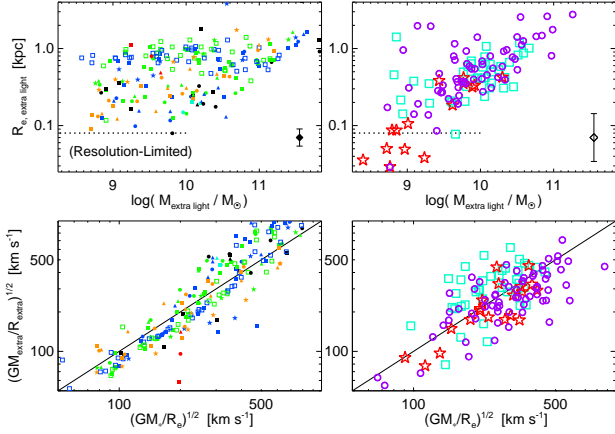


FIG. 21.— *Top*: Effective radius of the extra light component (*not* equivalent to the radius where it breaks from the outer Sérsic fit) as a function of extra light mass (points as in Figure 14). Simulations (*left*) and observations (*right*) are similar, especially if we restrict to simulations with initial gas fractions  $\sim 0.2-0.4$ . Resolution limits (see Appendix B) prevent us from simulating systems with  $R_{\text{extra}} \ll 100$  pc, but this is only important for the few very lowest-mass ellipticals ( $L \lesssim 0.01 L_*$ ; discussed in § 5). Filled diamond is typical sightline-to-sightline variance in the simulations, open diamond the source-to-source (or band-to-band) scatter in observed profile fits. *Bottom*: Effective velocity dispersion of the extra light component vs. that for the whole galaxy. Solid line shows  $(GM_{\text{extra}}/R_{\text{extra}}) = (GM_*/R_e)$  – the extra light collapses to the point where it is self-gravitating. The observed systems (*right*) follow a trend which agrees well with the simulations (*left*).

(2007). Briefly, however, these differences are physically expected, and follow what has been seen in earlier work (e.g. Barnes & Hernquist 1996; Naab et al. 2006a; Cox et al. 2006b; Oñorbe et al. 2006; Jesseit et al. 2007; Burkert et al. 2007): the central dissipational mass concentration in these systems is highly concentrated, and acts effectively like a point mass at the center of the galaxy to much of the material at  $R_e$ . When this becomes a large fraction of the galaxy mass ( $f_{\text{sb}} \gtrsim 0.1$ ), the potential becomes more spherical, which eliminates some of the phase space density that might otherwise support boxy and radial orbits (Binney & Petrou 1985; Hernquist et al. 1993; Naab et al. 2006a; Hoffman et al. 2007), and the central cusp can itself disrupt box orbits as they pass near the center (Gerhard & Binney 1985). This results in a larger fraction of rotationally supported tube orbits, diskier isophotal shapes, and (directly) a rounder overall system.

If we consider simulations with sufficiently large dissipational fractions ( $f_{\text{sb}} \gtrsim 0.1$ , similar to what we see in the observed systems), then, our gas-rich merger remnant simulations match well each of the distributions of  $\epsilon$ ,  $a_4/a$  and  $(V/\sigma)^*$  for cuspy ellipticals. This is demonstrated in much greater detail in Cox et al. (2006b). Here, we highlight that there is a significant difference in many of these properties between cusp and core ellipticals, as has been well established in previous studies (e.g. Bender et al. 1989; Faber et al. 1997). It is clear that our gas-rich merger simulations provide a good match to the observed distributions of  $(V/\sigma)^*$ ,  $a_4/a$ , and  $\epsilon$  in cuspy ellipticals, as we would expect, but they are not reproducing the more slowly rotating, boxy, round distributions characteristic of core ellipticals. This should also be borne in mind considering Figure 26: the lack of real correlations with extra light fraction appears to be true *within the cuspy population*; if core ellipticals are altered through subsequent spheroid-spheroid “dry” mergers, these properties can be modified (Naab et al. 2006b; Cox et al. 2008; Burkert et al. 2007), and it is expected that these processes will bring the predicted distributions into better agreement with those ob-

served in the cored population.

### 7.3. Nuclear Black Hole Masses

Figure 27 shows how the BH masses scale with extra light mass, both globally and at fixed stellar mass. We plot all of our simulations which include central BHs, and include the cusp ellipticals in our sample for which direct kinematic or maser measurements of a central BH have been possible (compiled from Magorrian et al. 1998; Merritt & Ferrarese 2001; Tremaine et al. 2002; Marconi & Hunt 2003; Häring & Rix 2004; Aller & Richstone 2007). For more details, we refer to Hopkins et al. (2007b). There is a correlation in simulations and observations between BH mass and extra light mass. However, this appears to be largely driven by the correlation between BH mass and total spheroid stellar mass, which has smaller dispersion and a weaker residual dependence on e.g. gas fraction or orbital properties. This is expected: if BH mass is actually sensitive to the depth of the central potential and spheroid binding energy, as argued from the nature of the fundamental plane-like correlation for BH masses and host properties demonstrated in Hopkins et al. (2007a,b) and Aller & Richstone (2007), then this is better correlated with the total stellar mass setting the potential than the few percent of the mass in the extra light component.

We might expect though, that at fixed total stellar mass, systems with larger extra light components, since this formed a more compact remnant, would have somewhat deeper potentials. Given the black hole fundamental plane (BHFP) in terms of stellar mass and  $R_e$  (i.e. scaling of BH mass with  $R_e$  or, equivalently,  $\sigma$  at fixed galaxy stellar mass, as in Hopkins et al. (2007a,b)), and the scaling of  $R_e$  with extra light fraction at fixed mass seen in Figure 22, we can estimate the dependence of BH mass on extra light fraction at fixed stellar mass. Figure 27 shows the residual of BH mass (i.e. BH mass relative to that expected at each stellar mass) as a function of extra light fraction, compared to this expectation. There is considerable scatter, but the simulations and few observed systems broadly follow the expected trend – namely that the cusp mass does not primarily drive  $M_{\text{BH}}$ , but that at fixed stellar mass, increasing dissipation builds more compact remnants which have higher binding energies and therefore, via the BHFP, larger BH masses.

## 8. IMPACT OF “EXTRA LIGHT” ON STELLAR POPULATIONS

If a significant fraction of gas dissipates to produce a central mass concentration, and this forms stars in a rapid central starburst, we should expect this to leave an imprint on stellar population gradients in the remnant (e.g. Mihos & Hernquist 1994b).

Figure 28 presents an illustrative example of these effects. We consider the elliptical NGC 3377, for which detailed stellar population gradients have been measured by Sánchez-Blázquez et al. (2007). The system is a clear cusp galaxy and rapid rotator with diskly isophotal shapes, and is included in our Kormendy et al. (2008) sample (Figure 5). From our comparison in Figure 5, we select the  $\sim 10$  simulations with the most similar surface brightness profiles. These generally fall within the range of those plotted in the figure, and all provide reasonably good fits to the observed surface brightness profile. For each simulation, we then extract the stellar populations as a function of radius, viewed from the same projection as that which provides the most similar sur-

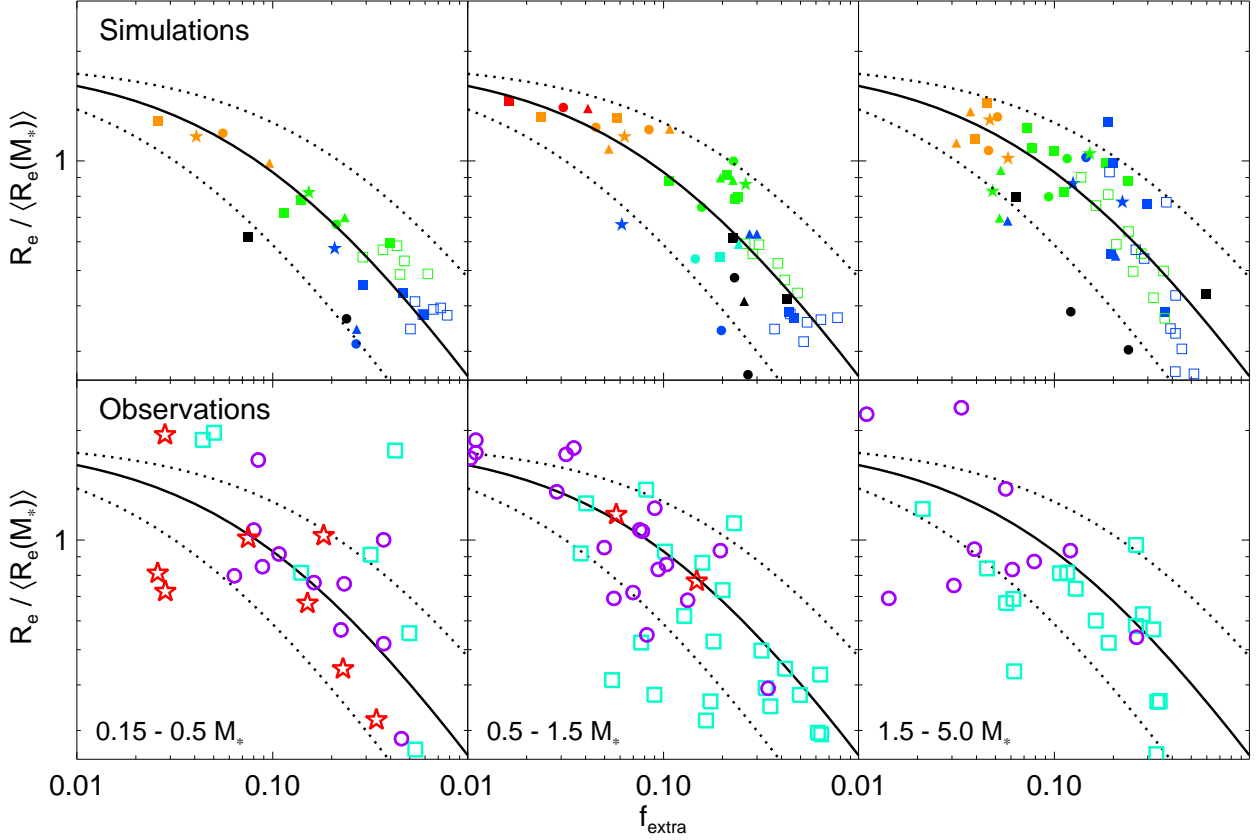


FIG. 22.— Effective radius  $R_e$  relative to the median value for all ellipticals of the same stellar mass, as a function of our fitted extra light fractions (the empirical tracer of the dissipational/starburst mass fraction). We compare simulated gas-rich merger remnants (top) with observed cusp ellipticals and gas-rich merger remnants (bottom), with points as in Figure 14. We show this in three bins of stellar mass (relative to  $M_* \approx 10^{11} M_\odot$ , or  $M_V^* = -21$ ). Solid (dotted) lines show the mean ( $\pm 1\sigma$ ) correlation, following the analytic solution for dissipational mergers and fits to our simulation in Covington et al. (2008). Simulations and observations exhibit the same behavior: systems with smaller  $R_e$  at fixed mass have systematically larger extra light fractions ( $> 6\sigma$  significance in the observations). This implies that, at fixed mass, systems are driven along the fundamental plane by the relative amount of dissipation involved in their formation.

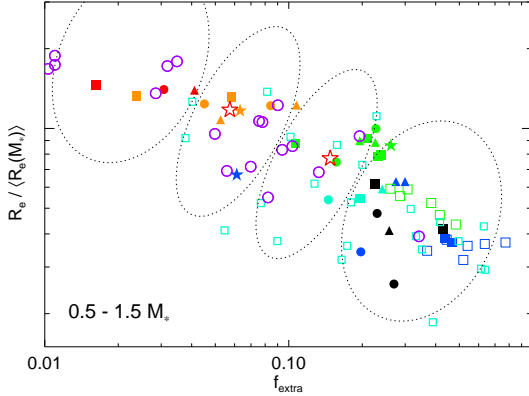


FIG. 23.— Center panels of Figure 22, with four regions along the correlation between effective radius and extra light fraction at fixed mass highlighted. The surface brightness profiles in these regions are shown in Figures 24 & 25.

face brightness profile to NGC 3377 (although the sightline-to-sightline variation is weak).

We model the emission from each star particle treating it as a single stellar population with the formation time and metallicity determined self-consistently from the star-forming gas in our simulations, and convolving with the stellar population models of Bruzual & Charlot (2003), assuming a Chabrier (2003) initial mass function. The observed stellar population parameters are effectively light-weighted in the optical SED, so as a rough proxy for this we extract, in each major-axis ra-

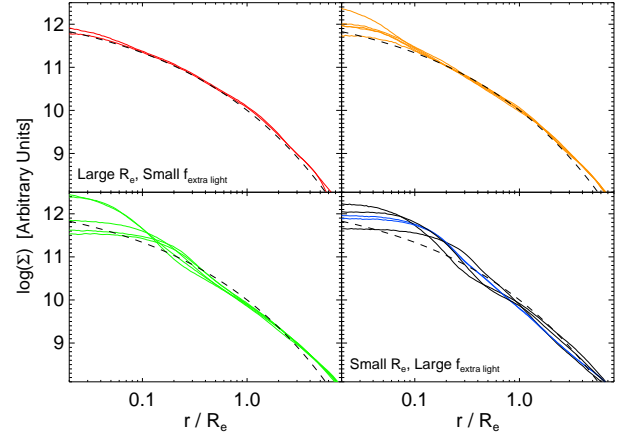


FIG. 24.— Light profiles of simulated systems with different  $R_e$  at fixed stellar mass. We plot all profiles from our simulations (colors denote simulation gas fractions as Figure 14) from each of the labeled regions in the  $R_e - f_{\text{sb}}$  space for the  $\sim M_*$  galaxy mass bin in Figure 23, in order from largest  $R_e$  (smallest  $f_{\text{sb}}$ ) to smallest  $R_e$  (largest  $f_{\text{sb}}$ ) (left to right, top to bottom). Similar results are obtained for the other mass ranges. The dashed black line shows a constant Sérsic profile, the same in each panel, for comparison. There is a substantial systematic difference: smaller  $R_e$  systems at fixed stellar mass have more prominent central mass concentrations, driven by dissipation in our simulations.

dial annulus, the  $B$ -band light weighted stellar population age and metallicity from the simulation. The  $g-z$  color is determined directly in each annulus.



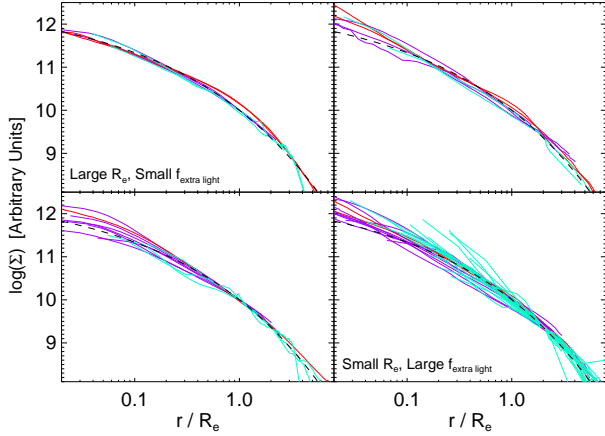


FIG. 25.— As Figure 25, but for the observed surface brightness profiles. Color denotes the observed sample as Figure 14.

Of course, doing this requires that we pick a definite time after the merger to view a simulation. We therefore show results for three representative times. First, just  $\sim 10^8$  yr after the final coalescence of the two galactic nuclei, when the object would likely be classified as a recent merger remnant. Second,  $\sim 3$  Gyr after the final merger, which is representative of younger  $\sim L_*$  cusp ellipticals. Specifically, we choose this time because the total light-weighted age, integrated over the whole galaxy, at this point matches that observationally inferred for NGC 3377 – i.e. when our comparisons are most appropriate. Third, we show the remnant after  $\sim 10$  Gyr, i.e. having evolved in isolation for nearly a Hubble time, comparable to the oldest observed ellipticals. At  $t = 3$  Gyr, we directly plot the observed age, metallicity, and color profiles from Sánchez-Blázquez et al. (2007). At the other times, we make the lowest-order reasonable corrections to highlight relative evolution in the shapes of the profiles: we add or subtract the appropriate age difference uniformly from the age profile, and likewise add or subtract the mean color difference expected for a single stellar population of the mean observed age and luminosity. Again, these leave the profile shapes unchanged – we merely shift them by the expected mean to compare with the shape changes predicted by our simulations.

At early times ( $t = 0.1$  Gyr), the gradients are strong. The stars formed in the central starburst are very young, and thus dominate the central light. Unsurprisingly, then, the age at the center of the galaxy is approximately just the time since the merger,  $\sim 0.1$  Gyr. This rises to  $\sim 3-5$  Gyr in the outermost regions, representative of the ages of the stars that were forming before the merger proper began. The central population is also the most metal rich, producing a similar strong metallicity gradient. The young, blue stellar populations of the center result in a strong color gradient with a blue core, common among young merger remnants (e.g. Schweizer & Seitzer 1992; Schweizer 1996; Rothberg & Joseph 2004; Yamauchi & Goto 2005).

The gradients in these quantities are most pronounced between  $\sim 0.05-0.1 R_e$  and  $\sim R_e$ : at much smaller or larger radii they tend to flatten. This intermediate region is the transition between dominance of the pre-merger stellar populations and central cusp – the gradients are primarily driven by the mean difference in stellar population parameters between the central starburst and outer old stellar components. This, in principle, allows arbitrarily strong gradients at the radii typically observed, but at larger radii, for example, violent re-

laxation mixes the old stars, washing out initial gradients and leading to a flattening in the total gradient. As predicted, these trends are typical in observed stellar population gradients (e.g. Mehlert et al. 2003; Sánchez-Blázquez et al. 2007; Reda et al. 2007).

By  $\sim 3$  Gyr after the merger, the age and metallicity gradients have weakened slightly. The apparent age gradient, quantified as e.g.  $d \log(\text{age})/d \log(r)$  is much weaker at this time, but largely for artificial reasons – adding a uniform  $\sim 3$  Gyr to the age of the system accounts for most of this, since it makes the difference in  $\log(\text{age})$  smaller. In terms of  $d(\text{age})/d \log(r)$ , the effects are more subtle, comparable to what is seen in the metallicity gradient. The gradients do, at this level, weaken slightly. This is because the now older central stellar populations have a lower  $L/M$ , more comparable to the old stars with which they are mixed. There is therefore slightly more mixing between the pre-merger and starburst populations. This can be seen in the metallicity gradients, which we would expect (to lowest order) to remain constant with time. Still, the effect is clearly second-order. These trends continue with time, as can be seen at the time  $\sim 10$  Gyr after the merger.

The color gradients evolve significantly with time, however. The inner regions are younger, which at early times (when they are very young,  $\lesssim 0.5$  Gyr) typically results in blue cores and a color gradient which becomes redder at larger radii (note, however, that at times very close to the merger, dust can reverse this trend). However, they are also more metal-rich, which tends to make them redder. After  $\sim 1$  Gyr, the effects of the age difference are much less prominent, and the color gradient becomes dominated by the metallicity gradient, resulting in *red* cores, and reversing the sense of the gradient. At even later times, the strength of this gradient (towards redder central regions) becomes stronger, although it remains relatively weak. We therefore expect that most ellipticals, even those which are relatively young, will have weak color gradients with red cores, as observed (Faber et al. 1989; Bender et al. 1993; Trager et al. 2000; Côté et al. 2006; Ferrarese et al. 2006). This should caution strongly against inferring too much from an observed color gradient, since the physical meanings and sense of the color gradients in typical simulations not only quantitatively depend on time and relative age, metallicity, and abundance gradients, but in fact usually reverse their meaning and behavior with time.

Because the star formation history depends on spatial location, mergers and dissipation can also induce gradients in e.g. the chemical abundance patterns and  $\alpha$ -enrichment of ellipticals. However, we do not show these explicitly for two reasons. First, our simulation code does not currently track separate enrichment by different species, so our estimates of such are based on crude analytic estimates (taking e.g. the star formation history in radial bins and estimating the  $\alpha$ -enrichment based on a closed-box model). Second, and more important, the effects are much more sensitive to the initial conditions and cosmological merger history. For example, one can imagine a situation where stars form over a fairly extended time period in the initial disks, leading to relatively high  $[\text{Fe}/\text{Mg}]$  at large radii. The merger then forms a rapid starburst in the center, which will preferentially be  $\alpha$ -enriched but not have time to self-enrich in heavier elements, leading to a decreasing  $\alpha$ -enrichment gradient. However, to the extent that *most* of the metal content of the central starburst often comes from the previous history of enrichment of that gas in the pre-merger disks (i.e. gas that enriched over long timescales), the additional effect of the starburst will be quite weak, leading to



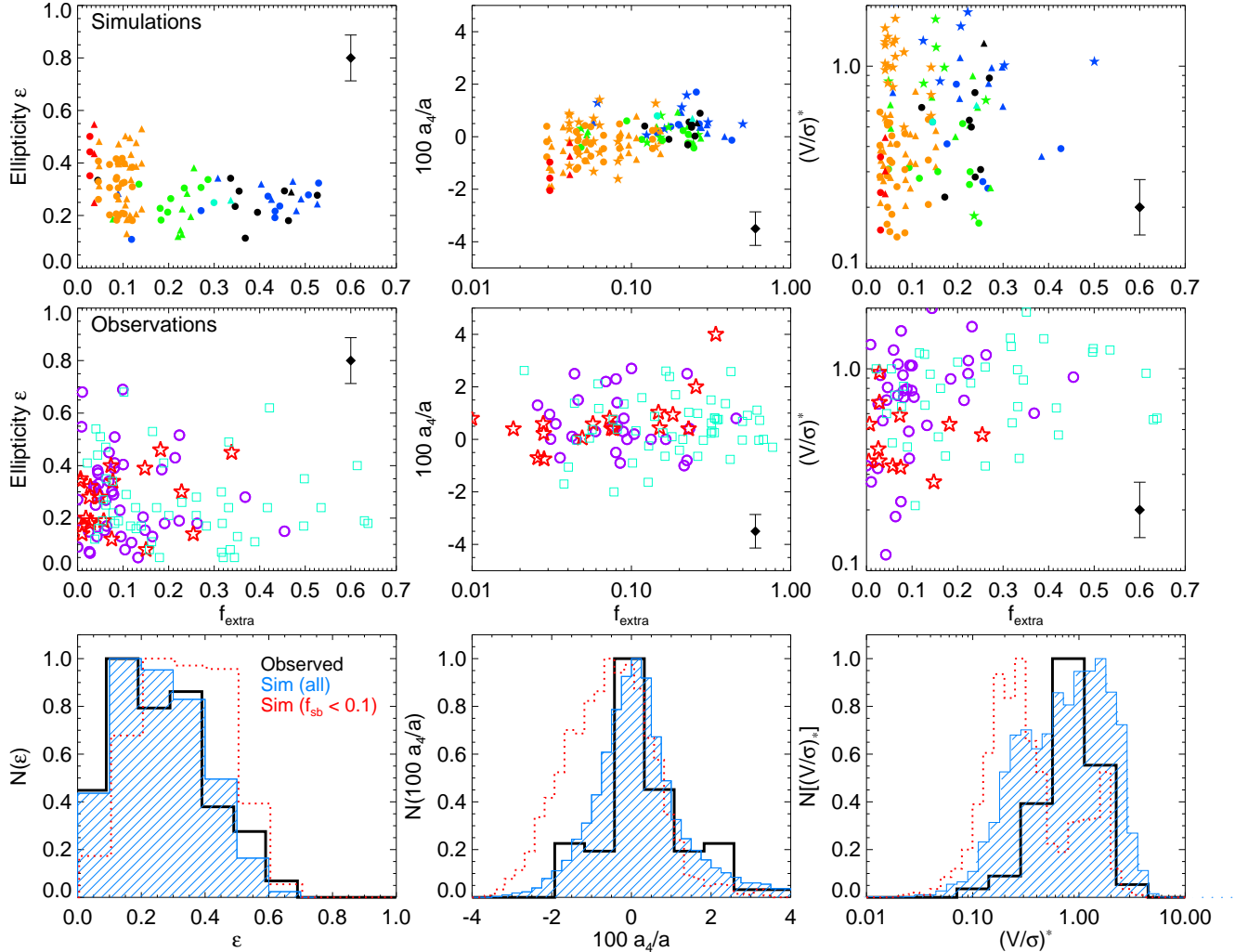


FIG. 26.— *Top*: Correlation between fitted extra light fraction (in both simulations and observed cuspy ellipticals, plotted as in Figure 14) and global kinematic properties of the galaxy: rotation  $(V/\sigma)^*$ , boxy/diskyness  $100 a_4/a$ , and ellipticity  $\epsilon$ . Median values across sightlines are plotted. Black points with error bars show the typical  $\sim 1\sigma$  sightline-to-sightline dispersion in each quantity from our simulations. *Bottom*: Histograms show the distribution in each property, for observed systems (thick black line), dissipational simulations which have similar moderate extra light fractions (blue shaded), and gas-poor (nearly dissipationless) simulations ( $f_{\text{sb}} < 0.1$ ; red dotted). The simulation distributions uniformly sample each simulation in solid angle over  $\sim 100$  lines-of-sight (including the large sightline-to-sightline dispersion in the top panels). Broadly, cuspy ellipticals and gas-rich merger remnants occupy a wider range in these parameters at low  $f_{\text{sb}}$ , but are uniformly rapid rotators, with slightly diskier isophotal shapes, and slightly rounder ellipticities at large  $f_{\text{sb}} \gtrsim 0.1$ . For more details, see Cox et al. (2006b).

gradients of only  $\sim 0.1$  in  $[\text{Fe}/\text{Mg}]$  over  $\sim 0.01 - 10 R_e$ .

Furthermore, one can also imagine a scenario in which the progenitor disks rapidly exhaust their gas in a short timescale leading to high  $\alpha$ -enrichment, retaining a relatively poor gas reservoir for the final merger. Because this gas is retained over long time periods, it enriches in Fe-elements from the older disk stellar populations, and after forming stars in the central starburst creates a gradient with the opposite sense (i.e. decreasing  $\alpha$ -enrichment with radius). Again, our estimates suggest the effect will be weak.

In either case, because the magnitude of the induced  $\alpha$ -enrichment gradients are comparable to those observed in spiral galaxies (e.g. Moorthy & Holtzman 2006; Ganda et al. 2007), the final prediction is much more sensitive to the initial conditions (unlike e.g. the induced total metallicity gradients, which are typically stronger than those in comparable disks). The mean or total  $\alpha$ -enrichment, on the other hand, depends of course primarily on the timescale for the formation of most of the stellar mass – which in almost all the cases of interest here means the pre-merger disks, which we are not

attempting to model. Further complicating matters, cosmological infall or accretion of new gas and minor mergers will play a (fractionally) larger role. For these reasons, a more comprehensive set of models is needed to say anything quantitative about  $\alpha$ -enrichment gradients, but it is nevertheless reassuring that the magnitude and sense (both positive and negative) of these possible induced gradients are in fact qualitatively similar to what is observed (e.g. Reda et al. 2007; Sánchez-Blázquez et al. 2007).

Figure 28 is instructive, but it is difficult to compare with all systems. We therefore globally compare gradient strengths by fitting the mean gradient in metallicity and age over the range  $\sim 0.1 - 1 R_e$  in each of our simulations, comparable to the range typically used observationally (e.g. Reda et al. 2007, and references therein). We consider the results extracted at a series of times after the merger similar to those in Figure 28.

Figure 29 shows how these gradient strengths compare to those in observed ellipticals (from Mehlert et al. 2003; Reda et al. 2007; Sánchez-Blázquez et al. 2007). We consider gradient strength as a function of extra light fraction, velocity

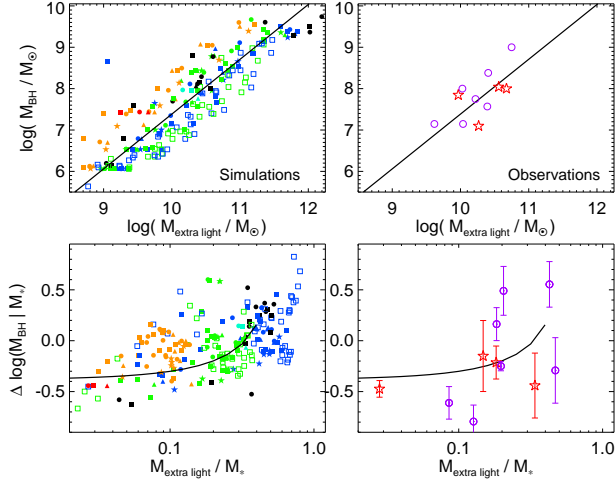


FIG. 27.— *Top*: BH mass as a function of fitted extra light mass, in our simulations (*left*) and observed systems that have direct BH mass measurements (*right*; only a small fraction of our sample have such BH masses measured). *Bottom*: Residual correlation of BH mass with extra light mass at fixed stellar mass (i.e.  $M_{\text{BH}}/\langle M_{\text{BH}}(M_*) \rangle$  versus  $M_{\text{extra}}/M_*$ ). Solid line is the expectation if systems obey the correlation between  $f_{\text{sb}}$  and  $R_e$  from Figure 22 and the black hole fundamental plane (Hopkins et al. 2007b). There is a significant  $M_{\text{BH}} - M_{\text{extra}}$  correlation, but it largely reflects the  $M_{\text{BH}} - M_*$  correlation or BHFP. At fixed stellar mass, the (weak) residual trend comes from the BHFP as increased dissipation builds a more compact remnant with deeper potential, and therefore larger BH.

dispersion, central stellar population age (averaged within an aperture of  $R_e/8$ , again comparable to typical observations), and central metallicity. There is a noticeable correlation between gradient strength and the excess light fraction; we expect this, since as noted above this central light drives most of the gradients. This also gives rise to a correlation between e.g. metallicity gradient and central metallicity, age gradient and central age, and different gradients themselves (stronger metallicity gradients tend to accompany stronger age gradients). There is not a strong dependence of gradient on mass, however (what there is is mostly driven by the mean dependence of extra light fraction on stellar mass). In each case, the observations occupy a similar locus to the simulations.

There have been some claims that the metallicities (Naab & Ostriker 2007) and metallicity gradients (Forbes et al. 2005) in ellipticals are too large/strong for them to be formed from mergers of present-day spirals. However, these arguments fail to account for the role of dissipation in increasing the central metallicity and giving rise to strong metallicity gradients in merger remnants. The left panels of Figure 29 demonstrate that, for moderate gas fractions, our simulations occupy a similar locus in both central metallicity and metallicity gradients to observed ellipticals. The metallicities typically quoted in stellar population studies are *central* metallicities, measured within  $\sim R_e/8$  (or within a central fiber in automated surveys such as SDSS). It therefore requires only a small amount of material to rapidly self-enrich in the central regions to explain these metallicities – our simulations even with  $\sim 5\%$  excess light fractions are able to do so (reaching  $[Z/H]_c \sim 0.5$  and  $d[Z/H]/d\log(r) \sim -0.6$ ). Since strong central metallicities often accompany strong metallicity gradients, the actual total metal mass of the galaxy (estimated from the combination of the surface density profile and metallicity profile) can easily be a factor  $\sim 3$  smaller than the metal mass that would be inferred if the system had a constant metallicity equal to the quoted central values.

We emphasize that the pre-merger stars in our simulations

are initialized to have a low uniform metallicity with no initial gradients (so that we can be sure any gradients we see are the result of the simulation dynamics, not artifacts of our initial conditions). Since more realistic initial disks will already have high metallicities  $\sim Z_\odot$  (similar, in fact, to ellipticals of the same mass; see e.g. Gallazzi et al. 2005), and metallicity gradients in the same sense as those produced in our simulations, the metallicities and metallicity gradients in our simulations are only lower bounds to the true values that can arise in dissipational mergers. Furthermore, recycling of metal-rich gas by stellar evolution (which we do not model here, but see e.g. Ciotti & Ostriker 2007) will subsequently enrich the system.

Since the behavior of the color gradients is somewhat more complex, we try and reduce it to the key qualitative element. Figure 30 shows the distribution in color difference at  $R_e/8$  and at  $R_e$ , a rough proxy for the color gradients, at various times after the merger. Observed distributions from samples of cusp ellipticals, with typical ages  $\sim 3 - 8$  Gyr, are also shown. The transition from initial blue cores shortly after the merger to red cores in relaxed ellipticals is obvious, as is the weakness of the color differences. The simulations and observations trace broadly the same distribution for post-merger times of  $\sim 3 - 10$  Gyr. We find a similar agreement comparing to the  $V - I$  color gradients in Lauer et al. (2005), and the  $V - R$  and  $V - I$  color gradients in Bender et al. (1988).

The weak color gradients in observed ellipticals are often used to justify the assumption of a constant *stellar* mass-to-light ratio as a function of radius, an assumption we have used in comparing our simulations and observed systems. In Figure 31, we test this assumption directly in our simulations. We consider two  $\sim L_*$  galaxy mergers, one relatively gas poor (a case which happens to provide a reasonable match to many of the observed ellipticals), and another otherwise equal but gas rich merger, both of which have typical color and stellar population gradients. We directly calculate the stellar mass-to-light ratios in narrow major-axis radial annuli in both  $K$ -band and  $B$ -band, at different times after the peak of the merger-induced starburst.

The  $M/L$  gradients reflect what is expected from the color gradients, and supports our assumption of nearly constant  $M/L$  with radius. At early times  $\ll 1$  Gyr, the central stellar populations are bright (associated with blue cores), and in  $B$ -band, nuclear dust obscuration makes the central  $M/L$  sensitive to viewing angle. This is a relevant for the recent merger remnants studied in Paper I (although they are observed in the  $K$ -band), and we discuss the implications for the youngest systems (with very large apparent  $f_{\text{extra}} \gtrsim 0.5$ ) therein. By  $\sim 2$  Gyr after the merger, however, the remnants have typical weak, red cores and  $M/L$  in optical bands such as  $B$  and  $V$  is usually constant as a function of radius to within  $\lesssim 20\%$ . At these ages, the parameters derived by fitting to optical profiles are identical to those obtained directly fitting the stellar mass profiles. The gradients in age (younger at the center) and metallicity (more metal rich at the center) have opposite effects in the optical, yielding negligible dependence of  $M/L$  on radius (in  $K$  band, the effects do not cancel; however among our observed samples only the recent merger remnants from Rothberg & Joseph (2004) are observed in  $K$ -band, so we refer to Paper I for more details). Reassuringly, this is similar to a purely empirical estimate based on the color-dependent  $M/L$  from Bell et al. (2003) and the observed color gradients. All of the ellipticals we study have estimated stellar population ages older than this threshold (and weak color gradients)

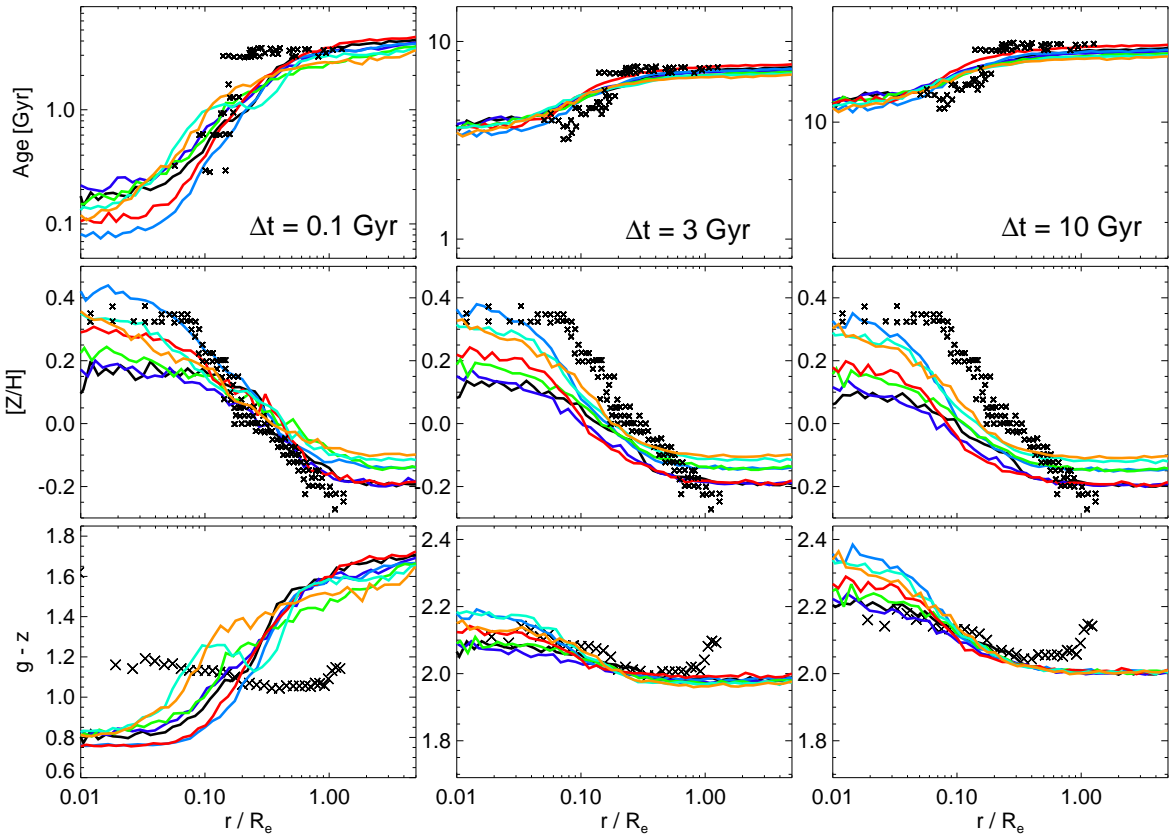


FIG. 28.— Comparison of the observed stellar population and color gradients (points) of NGC 3377 with those in the  $\sim 10$  simulations (lines) which most closely match its surface brightness profile (see Figure 5). The  $B$ -band light weighted parameters are plotted at three different times after the merger (labeled), with  $\Delta t = 3$  Gyr corresponding roughly to the observed mean stellar population ages in NGC 3377 (points there are plotted exactly as observed). At  $\Delta t = 0.1$  and 10 Gyr, in contrast, we have added the mean age offsets ( $-2.9$  Gyr and  $+7$  Gyr), and shifted the colors by the mean difference expected for passive evolution of a single stellar population with solar metallicity and the quoted age; this highlights the change in shape of the simulation gradients, as well as their normalizations. The simulated age and metallicity gradients fade slightly with time, as the difference in stellar populations becomes less prominent. At all times, however, the gradients are primarily driven by the mean difference in age and metallicity between the compact central starburst populations and the violently relaxed pre-merger populations. At early times, young, starburst populations often yield blue cores and a rising color gradient; at late times, the age effect weakens, and the enhanced metallicity of the starburst population dominates, reversing the color gradient (yielding red cores).

and are observed in these optical bands, so our results should be robust to stellar population effects.

Given the dependence of both gradient strength and effective radius (Figure 22) on dissipation, we would expect that systems with smaller  $R_e$  at fixed stellar mass (an indicator of greater dissipation) should exhibit somewhat stronger stellar population gradients. Figure 32 shows the predicted gradient strength versus effective radius from simulations and observed systems. We focus on the metallicity gradient: the color and age gradients evolve strongly with time, introducing much larger scatter and possibly even reversing the predicted trends here. There is a significant trend predicted, and the observations show some tentative evidence for such behavior, but more data are needed to determine this robustly (because there is a mean offset in the range of metallicity gradients at different masses, it is important to consider narrow ranges in observed stellar mass). To the extent that the strength of the metallicity gradients is an indicator of the degree of dissipation in the elliptical formation event, this prediction potentially provides a completely non-parametric means to search for non-homology (i.e. differential degrees of dissipation as a function of radius at fixed mass) along the fundamental plane.

## 9. DISCUSSION

We have studied the formation and properties of extra light and cusps in elliptical galaxies using a large library of both

numerical simulations and local observed cuspy ellipticals. We demonstrate the relation of these observed cusps to the prediction of Mihos & Hernquist (1994a) with our improved numerical models: namely, that tidal torques in major mergers of gas-rich disks channel gas into the central regions of the galaxy, where it forms a dense central starburst. The starburst leaves a central light excess with a high phase space density, making the remnant more compact and reconciling the densities of disks and elliptical galaxies. Improvements in spatial resolution (the “extra light” in previous numerical studies has generally been entirely unresolved), numerical treatments (see Appendix B), and models for star formation allow us to make detailed comparisons and for the first time demonstrate good agreement between the extra light and cusps in simulated gas-rich merger remnants and observed cusp ellipticals.

We argue that stars in these cuspy ellipticals (specifically, we intend this to represent those ellipticals formed immediately in gas-rich major mergers; not those which may have had subsequent gas-poor re-mergers) should be separated into at least two distinct populations. First, stars which are formed in the disks (or otherwise in extended distributions in progenitor galaxies) before the final merger and coalescence of the two galaxies. The final merger scatters these stellar orbits and they undergo violent relaxation. They dominate the light, even in highly gas-rich merger remnants, outside of  $\sim 0.5 - 1$  kpc, and form a Sérsic-law profile owing to their partial violent

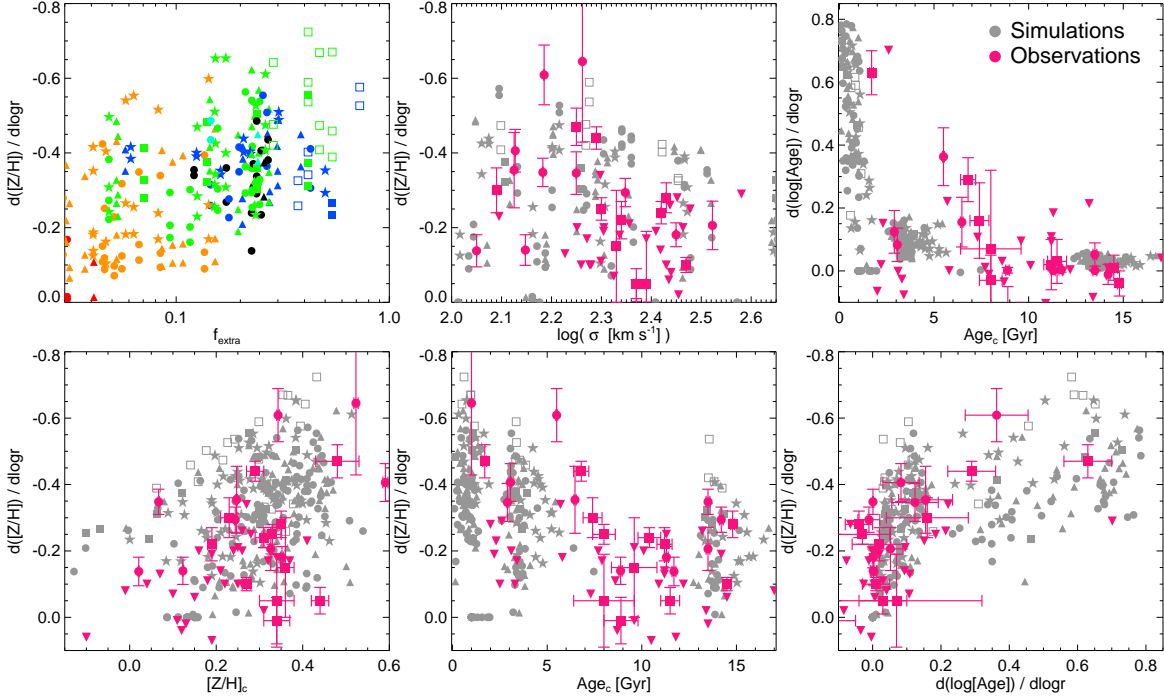


FIG. 29.— *Top Left*: Correlation between metallicity gradient ( $d[Z/H]/d\log r$ ) and extra light fraction ( $f_{\text{extra}}$ ) in our simulations (points as in Figure 14). *Remaining Panels*: Various correlations between metallicity gradients ( $d[Z/H]/d\log r$ ), age gradients ( $d\log(\text{Age})/d\log r$ ), central velocity dispersion  $\sigma$ , central light-weighted stellar population age ( $\text{Age}_c$ ), and central light-weighted stellar population metallicity ( $[Z/H]_c$ ). For clarity, the simulations are plotted in these panels as light grey points, and compared with observed ellipticals (magenta points; triangles, squares, and diamonds are from the samples of Mehlert et al. (2003); Reda et al. (2007); Sánchez-Blázquez et al. (2007), respectively). The correlation between gradient strength and the excess light fraction (*top left*) reflects the fact that the central light drives most of the gradients. This gives rise to the associated correlations shown in other panels. In each case, the observations occupy a similar locus to the simulations.

relaxation. Second, the starburst or dissipational population, formed in the central gas concentration in the final merger. This component is compact, and dominates the light inside a small radius  $\lesssim 0.5 - 1$  kpc. These stars *do not* undergo significant violent relaxation, but form in a nearly fixed background potential set by the dissipationless component of the galaxy. The size of the dissipational component is set primarily by the radius at which it becomes self-gravitating; the gas is then generally stable against further collapse (even with cooling) and rapidly forms stars.<sup>13</sup>

### 9.1. Comparing Simulations and Observations: Empirical Decomposition of Light Profiles

Observations and simulations have, in recent years, been driven to convergence on this multi-component description of elliptical light profiles, at least within the “cusp” population (Kormendy 1999; Kormendy et al. 2008; Côté et al. 2006, 2007; Ferrarese et al. 2006). In particular, the combination of ground-based and high-resolution *HST* photometry has allowed observers, from a purely phenomenological perspective, to recognize central extra light components beyond the inward extrapolation of an outer profile. The interpretation proposed herein has been advanced as the explanation for these central profile shapes, supported in a purely empirical manner by gradients in e.g. stellar populations, isophotal shapes, and stellar kinematics.

By applying observational methods to a large library of sim-

ulations, we can directly compare simulations with different degrees of dissipation to observed light profiles, in order to determine what is required in a merger-driven scenario in order to reproduce the observations. We find that in all cases of ellipticals of moderate masses  $\gtrsim 0.1 M_*$ , we have simulations which provide excellent matches to the observed systems (down to our resolution limits  $\sim 30 - 50$  pc), comparable to the typical point-to-point variance inherent in the simulation surface brightness profiles ( $\sigma_\mu \lesssim 0.1$ ). We can therefore further use this ensemble of simulations to test different means of decomposing observed profiles in order to calibrate a method which reliably and robustly recovers the appropriate *physical* decomposition in those simulations. We demonstrate (Figures 1 & 2) that an appropriately designed parametric fit to the total light profile recovers, on average, the correct (known physically in the simulations) decomposition of the light – the mass fraction and effective radius of both the physical starburst component and, separately, the outer dissipationless component.

The details of our methodology are discussed in § 4: essentially, we fit the surface brightness profiles to the sum of two Sérsic components, an inner and outer profile. The quantitative details of the decomposition are, of course, sensitive to the methodology and assumed functional forms; for this reason observations have often disagreed over the quantitative scales of extra light even for similar profiles (compare e.g. Côté et al. 2006; Kormendy et al. 2008). Fitting the entire light profile to a single Sérsic or a core-Sérsic law, for example, and comparing the central regions with the fit can yield physically meaningless values for the “extra light,” even though the result is, in a global sense, a formally good fit to the profile. Physically motivated models and simulated light pro-

<sup>13</sup> There is also a third component present in simulations but not prominent in light profile fitting: gas moved to large radii temporarily either by feedback or tidal effects, which settles into the relaxed remnant and re-forms small rotationally supported components (embedded disks, kinematically decoupled cores, etc.; e.g. Hernquist & Barnes 1991; Hopkins et al. 2008c).



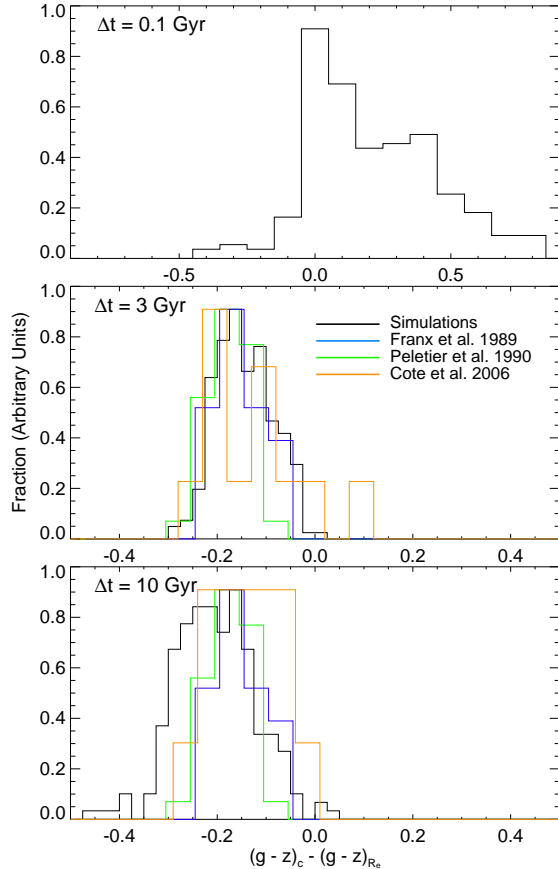


FIG. 30.— Color gradients (here the difference in mean color within  $R_e/8$  and  $R_e$ ) in simulations (black lines) at different times after the merger (labeled). We compare to the distribution for observed cusp elliptical samples (for the Côté et al. (2006) objects, we show the distribution for ellipticals  $< 6$  Gyr [*middle*] and  $> 6$  Gyr [*bottom*] old). Positive values indicate blue cores. For ages typical of cusp ellipticals, the remnants have relaxed to where metallicity gradients dominate the overall color gradient and yield red cores, albeit with generally weak gradients, with distributions similar to observed ellipticals of comparable ages.

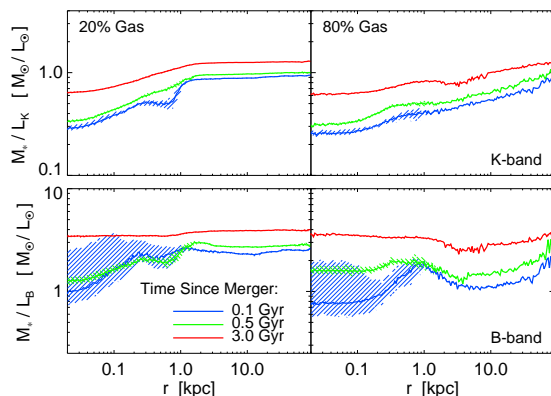


FIG. 31.— Mass-to-light ratio ( $M/L$ ) as a function of radius and time elapsed since the end of the merger-induced starburst, in  $K$ -band (*top*) and  $B$ -band (*bottom*), for relatively low gas fraction (*left*) and high gas fraction (*right*), otherwise equal “typical” ( $\sim L_*$ ) merger simulations. Shaded range shows the  $\sim 1\sigma$  range in  $M/L$  across different sightlines. At early times ( $\lesssim 1$  Gyr), young central stellar populations lead to a significant gradient (related to the strong “blue cores” in Figure 30). By  $\gtrsim 3$  Gyr (relevant for almost all the ellipticals in our sample), there is no significant dependence in optical bands, and only weak dependence in the near infrared (owing to the remaining metallicity gradients; for detailed discussion see Paper I).

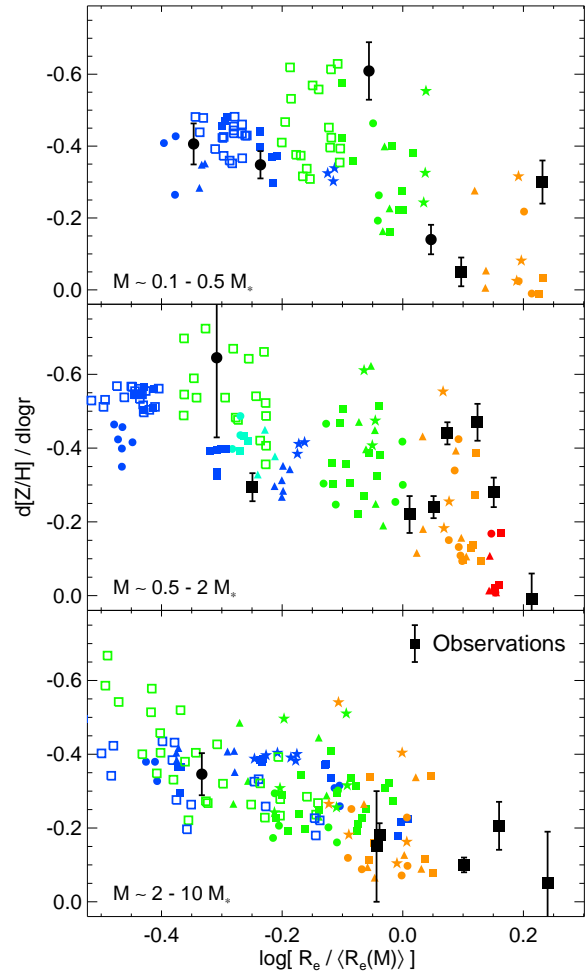


FIG. 32.— Correlation between metallicity gradient strength and effective radius (relative to the mean at each stellar mass), at fixed stellar mass (in the mass bins labeled). Our simulations are shown (point style as in Figure 14) along with the observed systems from Figure 29 (black circles and squares from Sánchez-Blázquez et al. (2007) and Reda et al. (2007), respectively). In the simulations, increased dissipation yields more compact remnants, with stronger stellar population gradients (unfortunately the color and age gradients are strongly sensitive to subsequent time evolution effects, so are less robust tracers of dissipation), predicting a correlation of the nature shown. Observations tentatively suggest the same, but more are needed to confirm this prediction of different degrees of dissipation along the fundamental plane.

files of the sort studied here are therefore necessary in order to make quantitative statements about extra light. Furthermore, a wide dynamic range is necessary; we find that the extra light is typically  $\sim 1 - 10\%$  of the galaxy light and becomes important within  $\sim 500$  pc ( $\sim 0.1 R_e$ ). The extra light component, as it becomes larger, typically blends in more smoothly with the outer profile, and does not necessarily appear as a sharp departure from the outer light profile. Therefore, simultaneous resolution of small scales  $\sim 100$  pc where the extra light dominates, and large scales  $\sim 20 - 100$  kpc where the shape of the outer, dissipationless component can be robustly determined, is a critical observational ingredient enabling these comparisons.

We apply this decomposition to our simulations and to a number of observed samples: including the combination of detailed elliptical surface brightness profiles over a wide dynamic range in Kormendy et al. (2008) and Lauer et al. (2007a), and a large sample of gas-rich merger remnants observed in Rothberg & Joseph (2004). The results from our fits are included in Tables 1 & 2 (see Figures 3-13 and Ap-

pendix A). For the observed ellipticals, we consider only those which are observed to have central cusps in high-resolution HST imaging, as opposed to those with central cores or mass deficits, as the latter are commonly believed to form in gas-poor spheroid-spheroid remergers, which we do not model here. We instead undertake a comparison of those objects and simulations of both gas-rich and gas-poor mergers in Hopkins et al. (2008h).

Applying these methods to observations, then, provides a powerful new diagnostic of the formation history of galaxies. In the physical context of the models considered here, it is not only possible to estimate (from the existence of some central component) whether or not the formation of a given galaxy requires some dissipation, but *to empirically, quantitatively estimate the degree of dissipation – i.e. “how gas-rich” was the history or progenitor of a given elliptical.* We extend this to develop a number of new probes of galaxy merger history, and corresponding predictions and tests of the merger hypothesis.

### 9.2. Predictions and Observations

(1) From either fitted extra light/dissipational component masses, or a direct comparison of simulations and observations, we find that *there is a clear trend of increasing dissipation in the profiles of less massive ellipticals* (Figures 19-20). The required initial gas fractions in mergers to form profiles that resemble the observed systems are a decreasing function of mass, and at all masses from  $M_* \sim 10^9 - 10^{12} M_\odot$  span a range bracketed by the typical observed gas fractions of spiral galaxies at the same mass, at  $z = 0$  (bracketing the low end of the required gas fractions) and  $z \sim 2 - 3$  (bracketing the high end). In terms of the mass fraction in the final dissipational or starburst component, the trend is even more clear (significance  $\gg 5\sigma$ ), and is reflected in the observed extra light components. The trend is given by Equation (3):

$$\langle f_{\text{starburst}} \rangle \sim \left[ 1 + \left( \frac{M_*}{10^{9.15} M_\odot} \right)^{0.4} \right]^{-1}.$$

We are able to, for the first time, observationally directly infer the degree of dissipation from the surface brightness profiles of observed ellipticals and use it to show that, in line with predictions from e.g. their fundamental plane correlations (Carlberg 1986; Gunn 1987; Lake 1989; Kormendy 1989; Hernquist et al. 1993), dissipation is more important in lower mass ellipticals, reflecting the increasingly gas-rich nature of lower-mass progenitor spirals.

(2) At a given mass, the degree of dissipation strongly influences the size of the remnant. In both observations and simulations *we demonstrate a tight correlation between effective (half-light) radius at a given stellar mass and the inferred dissipational/extra light fraction* (Figure 22). This owes to the compact nature of the central dissipational component – increasing the mass fraction in this component means that the half-light radius must be smaller. This is also reflected as an increasing velocity dispersion with extra light fraction at fixed mass, but this effect is weaker (because of the role of dark matter in setting the total mass and velocity dispersion).

This has important implications for the fundamental plane of elliptical galaxies – namely that dissipation is a key driver of systems on the fundamental plane (in terms of e.g. stellar mass, in optical bands there are obviously also substantial stellar population effects). Looking at  $\sim L_*$  ellipticals along

the sequence of increasing dissipational component and decreasing effective radius, we directly show how this relates to homology-breaking in ellipticals (Figures 24-25). Those with large effective radii and little dissipation at a given mass are well-described by a Sérsic law (with our mean Sérsic index  $n \sim 2.5 - 3$ ) over the range  $\sim 0.01 - 5 R_e$ . Those with smaller effective radii and large dissipational components typically show an excess at small radii, reflecting the concentration of starburst light owing to dissipation. This grows with smaller radii and larger dissipational components, from prominence only at small radii  $\ll 0.1 R_e$  to  $\sim 0.5 R_e$  in extreme systems.

We caution that there is not an obvious sense of the shape of this extra component – in some cases the whole profile could still be well-fitted by a single Sérsic law (albeit with a higher index  $n_s$ ). In others, there is only a small excess in the  $\mu - r$  plane, but it extends to large radii  $\sim 0.5 R_e$  and therefore contributes considerably to the mass. In yet others it is similar to more obvious extra light, and to that visible in our most extreme simulations, as a sharp departure from the outer Sérsic law at small radii. In any case, however, the tight correlation between dissipational component strength and size of the elliptical can be directly seen to relate to a subtle non-homology in the central surface brightness of the galaxies, in both the observations and our simulations.

(3) We find that the outer Sérsic indices of cusp ellipticals are nearly constant as a function of stellar mass or any other properties (with median  $\sim 2.5 - 3$  and scatter  $\sim 0.7$ ; Figures 14-17). We emphasize that, given our two component decomposition, this outer Sérsic index is only meaningful in the sense of reflecting those violently relaxed stellar populations which were present in the progenitors before the final merger (fitting the entire profile to a single Sérsic index can yield a very different result). This is because the dissipationless component is relaxed under the influence of gravity, and is therefore roughly self-similar across scales.

We note this constant Sérsic index distribution is relevant for *gas-rich merger remnants*. As we demonstrate in Hopkins et al. (2008h), subsequent gas-poor re-mergers will systematically raise the outer Sérsic indices, and pseudobulges or other low-mass bulges may have systematically lower indices (and together these may drive a systematic dependence of Sérsic index on mass, owing to the cosmological dependence of formation history on mass). This has been seen in the Virgo cusp elliptical sample of Kormendy et al. (2008), and each of our observed samples independently confirms our prediction, and together they show no dependence of Sérsic index over more than three orders of magnitude in stellar mass. Especially restricting to a sample of ellipticals which are observed in multiple bands and from multiple ground-based sources and considering only those results for which the fits (from different bands and instruments) do not disagree, we confirm both the predicted Sérsic index distribution and lack of dependence on other galaxy properties. This agreement further suggests that cusp ellipticals are the direct remnants of gas-rich major mergers, without substantial subsequent re-merging.

(4) Extra light fraction does not, in any predictive sense, correlate with the global kinematic properties (namely, ellipticity, isophotal shape  $a_4$ , and rotation  $(V/\sigma)^*$ ) of ellipticals in our simulations or in the observations. However, there is in a broad sense a change in these properties for large versus small extra light fractions (Figure 26). At small extra light fractions



$\lesssim 5-10\%$ , remnants are more similar to the known properties of dissipationless disk-disk mergers (e.g. Barnes 1988), with a wide range in rotation properties, isophotal shapes, and ellipticities. At substantial extra light fractions, however, the systems are (on average) somewhat rounder, and are more uniformly disky and rapidly rotating. The dissipational component itself makes the remnant potential more spherical, and is closely related to kinematic subsystems formed from gas that survives the merger which contribute to the rotation and isophotal shapes (see e.g. Cox et al. 2006b; Robertson et al. 2006b; Dekel & Cox 2006; Naab et al. 2006a; Burkert et al. 2007). A distribution of dissipational/extra light fractions like that observed yields remnants with a similar distribution in each of these properties to observed cusp ellipticals, in striking contrast with dissipationless simulations that have historically not been able to match these properties.

(5) Black hole mass appears to be roughly correlated with the mass in the extra light component, in both simulations and observations, but we show that this is largely a reflection of the tighter correlation between black hole mass and total host spheroid stellar or dynamical mass (Figure 27). This is not surprising: if black hole mass most tightly follows the central potential or binding energy of the bulge, as argued from recent observations favoring a black hole fundamental plane (Hopkins et al. 2007a,b; Aller & Richstone 2007), then this is largely set by the total mass of the system. The extra light mass represents a perturbation to the binding energy/velocity dispersion the system would have if dissipationless, and there is in simulations a weak residual trend along the expected lines, but it is sufficiently weak that the present observations are inconclusive.

(6) The dissipation of gas into the central regions of ellipticals in a central starburst gives rise to significant gradients in the stellar populations (Figure 28). Since they are formed at the end of the merger, from gas channeled to the center of the galaxy after being enriched by star formation throughout the progenitor disks, the central stellar populations tend to be younger and more metal rich. The detailed gradient structure in our simulations corresponds well to what is typically observed – with metallicity increasing and age decreasing relatively smoothly from  $\sim R_e$  to  $\sim 0.03-0.1R_e$ . We do occasionally find anomalous behavior resembling various observed systems – e.g. non-monotonic trends in the stellar populations – but these are generally rare, as is also observed.

At large radii, observations find generally weaker gradients – our simulations suggest that these are not driven by dissipation in the merger, but rather reflect pre-existing gradients in the initial disks. To be conservative, we have not included them here, but experiments suggest that they are not completely destroyed: it is well known, for example, that particles roughly preserve their ordering in binding energy in mergers (Barnes 1992), so given the trend in spirals towards less metal enrichment and older ages in their outer regions, we expect a smeared out version of these gradients to continue weakly into the outer regions of merger remnants, where the stars are primarily those violently relaxed from the initial disks. Over the range where observed gradients are typically fit, we quantify the gradient strengths in our simulations and find they are similar to those observed, as a function of system mass, age, and metallicity (Figure 29). Previous claims that mergers would only yield weak gradients in ellipticals ignored the importance of dissipation, which allows us to form systems

with metallicity gradients comparable to the most extreme observed ( $d[Z/H]/d\log r \sim -0.8$ ).

In general, the gradients are not strongly dependent on mass, but do depend somewhat on the degree of dissipation (Figure 29). They also evolve significantly with stellar population age, as suggested by observations – not only do the stars become uniformly older, but as they age after the merger, the difference in mass to light ratio between young stars formed in the starburst and older stars becomes less significant, so in any light-weighted stellar population the younger starburst stars become (relatively) less prominent, and the gradient weakly washes out (Figure 28). Of course, being driven by the central dissipational population, the gradient strengths are also correlated with central metallicity and with one another, albeit with large scatter (and for e.g. uniformly high metallicities or weak gradients, these correlations break down). All of these trends are in good agreement with present-day observed ellipticals.

Furthermore, the central stellar metallicities of ellipticals (both their mean and distribution about that mean) as a function of e.g. mass and velocity dispersion, are reproduced in our simulations, given only the assumption that the initial spirals have metallicities appropriate for the observed disk galaxy mass-metallicity relation – in fact, when the initial disk gas fractions are moderate ( $\gtrsim 20\%$ ), we obtain this result from the self-enrichment tracked in our code (which dominates the final total central metallicity) even if the initial gas and stars have zero metallicity (Figure 29). Given that we simultaneously reproduce the central metallicities, metallicity gradients, and surface brightness profiles of observed cusp ellipticals, the claim that these systems have too much mass in metals to be produced from the merger of local spirals (Naab & Ostriker 2007) does not stand up, at least insofar as we are restricting to *cuspy* ellipticals.

We also reproduce the typical observed color gradients of these ellipticals (Figures 28 & 30). We caution that while time evolution of even physical quantities such as the metallicity and age gradients is non-trivial, the color gradients are even more complex. Generally, though, systems have blue cores (are more blue towards their centers) for a short time after the merger, commonly taken as a signature of a recent merger or central starburst, owing to the young central starburst population. However, this population is also more metal rich, so the gradient rapidly weakens and after a short period,  $\sim$  Gyr, the metallicity difference becomes more important and the systems have red cores (are redder towards their centers). The gradients are fairly weak, a difference of  $\sim 0.1-0.2$  mag between the color within  $R_e/8$  and  $R_e$ , and the simulated distribution of color gradient strengths agrees well with that observed in samples of local ellipticals (especially if we restrict broadly to similar mean stellar ages).

(7) Since increasing the amount of dissipation at a given total mass tends both to yield smaller effective radii and stronger stellar population gradients, we predict that the two should be correlated (again, at fixed stellar mass - considering too wide a range in stellar mass will wash out this correlation, since the two scale differently in the mean with stellar mass; Figure 32). The trend is not predicted to be dramatic, but should be observable, and comparison with recent observations does suggest that systems with smaller effective radii for their mass do have uniformly higher metallicity gradient strengths. Future observations should be able to test this more robustly, using metallicity gradients (we caution that the age gradients and, especially, color gradients are too age-sensitive to be con-

straining in this sense).

To the extent that gas-rich progenitor disks (at least at low-moderate redshifts) are so because they have more extended star formation histories, this should also be reflected in the integrated stellar populations of the ellipticals. This is well known in an integrated sense – low mass ellipticals (which form from low-mass, gas-rich disks) tend to have more extended star formation histories with less  $\alpha$ -element enrichment (e.g. Trager et al. 2000; Thomas et al. 2005). At fixed mass, however, if systems undergo mergers over roughly the same time period (which is generally true for systems of the same mass), then those with smaller effective radii (and lower  $M_{\text{dyn}}/M_*$ ) should have formed with more dissipation from more gas rich disks, which presumably had more extended star formation histories. This should yield younger pre-merger stellar population ages and less  $\alpha$ -enriched stellar populations, relative to progenitors of the same mass which had shorter star formation histories and exhausted their gas supply before the merger. There is one important caveat – systems of the same mass might also have had more gas-rich progenitors because they underwent mergers at very early times (making them older and more  $\alpha$ -enriched), but cosmological estimates (e.g. Hopkins et al. 2008b) suggest that systems with such early mergers will usually have multiple subsequent mergers at later times, so they will grow significantly in mass and have their effective radii substantially modified by these additional processes (and may reflect the same trends as more typical systems by  $z \sim 0$ ). In any case, this latter process is not dominant at a given stellar mass. We study this in greater detail in Hopkins et al. (2008e).

### 9.3. Synopsis

We have developed a paradigm in which to understand the structure of (cusp or extra light) ellipticals, in which there are fundamentally two stellar components: the relic of a a dissipational central starburst and a more extended violently relaxed component (introduced and discussed in e.g. Mihos & Hernquist 1994a; Kormendy 1999; Cox et al. 2006b; Kormendy et al. 2008). We have shown that these components can be separated with observations of sufficient quality, and can be used to constrain the formation histories of ellipticals and infer physically meaningful properties in a hierarchical formation scenario. This allows us to demonstrate that dissipation is critical in understanding the properties of ellipticals, including (but not limited to) the structure of their surface brightness profiles, their sizes, ellipticities, isophotal shapes and rotation, age, color, and metallicity gradients (and their evolution), and the gas content and properties of their progenitors.

We have studied these properties and identified robust trends across a large library of simulations, in which we vary e.g. the galaxy masses, initial gas fractions, concentrations, halo masses, presence or absence of bulges, presence or absence of black holes, feedback parameters from supernovae and stellar winds, orbital parameters and disk inclinations, and mass ratios of the merging galaxies. This range of parameters allows us to identify the most important physics. Most of these choices, for example, affect the surface brightness profile, extra light mass and radius of the extra light, concentration and effective radius of the remnant, and even its ellipticity and isophotal shape only indirectly. Ultimately, what determines the structure of the remnant (insofar as the properties we have considered) is, to first order, how much mass is in the dissipationless (violently relaxed) component ver-

sus the dissipational/starburst component at the time of the final merger(s). Therefore, changing something like the orbital parameters or initial galaxy structure can alter the remnant substantially, but predominantly only insofar as it affects the amount of gas which will be available at the time of the final coalescence of the galaxy nuclei (i.e. how much mass ends up in the starburst component, as opposed to being violently relaxed in this final merger; see also Cox et al. 2006c). Moreover, merger-induced starbursts may not be the only source of dissipation (for example, stellar mass loss may replenish the gas supply and lead to new dissipational bursts, see e.g. Ciotti & Ostriker 2007), and the merger history and series of induced dissipational events may be more complex than a single idealized major merger (see e.g. Kobayashi 2004; Naab et al. 2007), but for our purposes, all dissipational star formation will appear similar when observed and have the same effects (we are essentially measuring the integrated amount of dissipation).

We have demonstrated that this makes predictions for how fundamental plane scalings arise, which we study further in Hopkins et al. (2008a). Given these decompositions, we can attempt to observationally test whether sufficient dissipation, as a function of stellar mass, could have occurred in the inner regions of ellipticals to explain the discrepancies between their central densities and those of their proposed progenitor spirals. We make a wide range of new predictions for the distributions of these properties and how they scale with the degree of dissipation, and how they should scale with each other and various other observational proxies for this degree of dissipation (which we define herein). We have predicted and shown (given these proxies) that dissipation is indeed more important (contributing a larger mass fraction) in low-mass ellipticals, in line with expectations based on how gas fractions are known to scale with disk mass. Testing all of these with better observations should be possible in the near future, with well-defined samples of ellipticals and continued improvements in mapping e.g. the surface brightness profiles, stellar populations and their gradients, and structural properties of ellipticals over a wide dynamic range.

To the extent that their parameter correlations and theoretical formation scenarios are similar, these conclusions should also generalize to “classical” bulges in disk-dominated galaxies (as opposed to “pseudo-bulges” formed in secular processes, which we do not model herein, and which may or may not show similar structure). We have excluded them from our observational study in this paper because the presence of a large disk greatly increases the uncertainties in profile fitting (and makes it difficult to robustly identify multi-component structure in the bulge), but emphasize that re-analyzing the S0 and early-type spiral galaxies in our observational samples demonstrates that they are in all cases consistent with our conclusions. Indeed, studies of the central profiles of classical bulges in S0-Sbc galaxies, in those cases with sufficient resolution and dynamic range and without much obstruction from the outer disk, have begun to see evidence for central two-component bulge structure with extra light components similar to those predicted here (consistent in their profile shapes, sizes, mass fractions, kinematics, isophotal shapes, stellar populations, and colors; see e.g. Balcells et al. 2007; Peletier et al. 2007). We emphasize that these are distinct from the nuclear star clusters seen in some bulges, discussed in Appendix C.

It is important to extend this study to central core ellipticals, increasingly believed to be shaped by subsequent gas-

poor (spheroid-spheroid) re-mergers, and we consider these objects in Hopkins et al. (2008h). However, since cuspy ellipticals dominate the  $\sim L_*$  population, most of the mass density in present-day ellipticals is contained in those cuspy objects that we study herein. We also strongly emphasize that, if core populations are indeed the re-mergers of initially cuspy ellipticals, then the extra light or dissipational components are *not* destroyed in these mergers. Indeed, most simulations suggest that the dense, central components are sufficiently tightly bound that they feel relatively little disturbance in a dry merger. Although black hole scouring may scatter stars from the central region and create such a core (e.g. Milosavljević et al. 2002), these stars represent only a small fraction of the extra light population. In other words, scouring will flatten the central power-law like behavior of cusps of extra light, but not fundamentally remove the  $\sim 500$  pc central light concentrations remaining from a dissipational starburst. Furthermore, the impact of scouring will be restricted to mass scales of order the black hole mass, which is only  $\sim 10^{-3}$  the stellar mass, much smaller than the typically masses of the extra light components inferred through our analysis (e.g. Hopkins et al. 2008h). Given this, it should be possible to generalize our modeling and constraints to much more complex merger histories than the idealized single major merger scenarios considered in our simulation study, provided we recognize that the dissipational and dissipationless components are really integral sums over the dissipational and dissipationless events in the formation history of a given elliptical. Of course, subsequent gas poor mergers may have a number of other effects on the structural properties of the galaxies, modifying many of the properties we have argued are initially set by or correlated with the degree of dissipation – therefore we have excluded core ellipticals from our observational samples, and wish to emphasize the importance of doing so in subsequent observational comparisons.

As we noted in Paper I, there is considerable room for progress in modeling the extra light component itself and structure of nuclear profiles at small radii ( $\ll 100$  pc), where observations are making rapid progress; however, modeling these radii in a meaningful sense requires not just improved numerical resolution but also the inclusion of new physics that will allow simulations to self-consistently form the structures that would be resolved (giant molecular clouds, star forming regions and star clusters, individual supernova remnants, the multiple gas-phases of the ISM and their exchange, etc.). It

is an important and ambitious goal that the next generation of studies move beyond the sub-resolution prescriptions necessary when modeling larger scales, and include realistic ISM structure important in galactic nuclei.

Here, and in previous work (e.g. Hopkins et al. 2006a,c, 2008b,f) we have developed a conceptual framework for understanding the origin of starbursts, quasar activity, supermassive black holes, and elliptical galaxies. In this paradigm, the various objects and phenomena we have examined are connected in an evolutionary sequence that is ultimately triggered by mergers between gas-rich disk galaxies. Previously, from observed correlations between supermassive black holes and properties of their hosts, we have argued that elliptical galaxies must have originated through a process that blends together gas- and stellar-dynamics. This is motivated by simple physical considerations implying that supermassive black holes are mainly assembled by gas accretion (e.g. Lynden-Bell 1969) in order to satisfy the Soltan (1982) constraint relating black hole growth to quasar activity, and the notion that elliptical galaxies were put together by violent relaxation (e.g. Lynden-Bell 1967) acting on stars. The results of our analysis applied to recent merger products (Hopkins et al. 2008d), cuspy ellipticals (this paper), and elliptical galaxies with cores (Hopkins et al. 2008h) indicate that the same blend of gas- and stellar-dynamics is further essential for understanding the structural properties of the galaxies that harbor supermassive black holes. Together, this provides further support to the idea that elliptical galaxies and supermassive black holes originate via a common physical process (mergers of gas-rich galaxies) and, given the Soltan (1982) constraint and the discovery of ULIRGs, quasars and starbursts, respectively, as well.

We thank Sandy Faber, Marijn Franx, and Barry Rothberg for helpful discussions and contributed data sets used in this paper. We also thank the anonymous referee whose comments greatly improved the presentation of the manuscript. This work was supported in part by NSF grants ACI 96-19019, AST 00-71019, AST 02-06299, and AST 03-07690, and NASA ATP grants NAG5-12140, NAG5-13292, and NAG5-13381. JK’s work was supported in part by NSF grant AST 06-07490. Support for TJC was provided by the W. M. Keck Foundation.

## REFERENCES

- Aller, M. C., & Richstone, D. O. 2007, ApJ, 665, 120  
 Balcells, M., Graham, A. W., & Peletier, R. F. 2007, ApJ, 665, 1084  
 Barnes, J. E. 1988, ApJ, 331, 699  
 —. 1992, ApJ, 393, 484  
 Barnes, J. E., & Hernquist, L. 1992, ARA&A, 30, 705  
 —. 1996, ApJ, 471, 115  
 Barnes, J. E., & Hernquist, L. E. 1991, ApJ, 370, L65  
 Bell, E. F., & de Jong, R. S. 2001, ApJ, 550, 212  
 Bell, E. F., McIntosh, D. H., Katz, N., & Weinberg, M. D. 2003, ApJS, 149, 289  
 Bell, E. F., et al. 2006, ApJ, 640, 241  
 Bender, R. 1988, A&A, 193, L7  
 Bender, R., Burstein, D., & Faber, S. M. 1992, ApJ, 399, 462  
 —. 1993, ApJ, 411, 153  
 Bender, R., Doebereiner, S., & Moellenhoff, C. 1987, A&A, 177, L53  
 —. 1988, A&AS, 74, 385  
 Bender, R., Saglia, R. P., & Gerhard, O. E. 1994, MNRAS, 269, 785  
 Bender, R., Surma, P., Doebereiner, S., Moellenhoff, C., & Madejsky, R. 1989, A&A, 217, 35  
 Bender, R., et al. 2007, ApJ, in preparation  
 Binggeli, B., Sandage, A., & Tammann, G. A. 1985, AJ, 90, 1681  
 Binggeli, B., Sandage, A., & Tareghi, M. 1984, AJ, 89, 64  
 Binney, J., & Petrou, M. 1985, MNRAS, 214, 449  
 Blanton, M. R., Eisenstein, D., Hogg, D. W., Schlegel, D. J., & Brinkmann, J. 2005, ApJ, 629, 143  
 Böker, T., Laine, S., van der Marel, R. P., Sarzi, M., Rix, H.-W., Ho, L. C., & Shields, J. C. 2002, AJ, 123, 1389  
 Böker, T., Sarzi, M., McLaughlin, D. E., van der Marel, R. P., Rix, H.-W., Ho, L. C., & Shields, J. C. 2004, AJ, 127, 105  
 Borch, A., et al. 2006, A&A, 453, 869  
 Bournaud, F., Jog, C. J., & Combes, F. 2005, A&A, 437, 69  
 Boylan-Kolchin, M., Ma, C.-P., & Quataert, E. 2005, MNRAS, 362, 184  
 Bruzual, G., & Charlot, S. 2003, MNRAS, 344, 1000  
 Bullock, J. S., Kolatt, T. S., Sigad, Y., Somerville, R. S., Kravtsov, A. V., Klypin, A. A., Primack, J. R., & Dekel, A. 2001, MNRAS, 321, 559  
 Bundy, K., et al. 2006, ApJ, 651, 120  
 Burkert, A., Naab, T., & Johansson, P. H. 2007, ApJ, in press  
 arXiv:0710.0663, 710

- Busha, M. T., Evrard, A. E., Adams, F. C., & Wechsler, R. H. 2005, *MNRAS*, 363, L11
- Caon, N., Capaccioli, M., & D'Onofrio, M. 1993, *MNRAS*, 265, 1013
- , 1994, *A&AS*, 106, 199
- Caon, N., Capaccioli, M., & Rampazzo, R. 1990, *A&AS*, 86, 429
- Carlberg, R. G. 1986, *ApJ*, 310, 593
- Carollo, C. M. 1999, *ApJ*, 523, 566
- Carollo, C. M., Stiavelli, M., de Zeeuw, P. T., & Mack, J. 1997, *AJ*, 114, 2366
- Carollo, C. M., Stiavelli, M., & Mack, J. 1998, *AJ*, 116, 68
- Chabrier, G. 2003, *PASP*, 115, 763
- Ciotti, L., & Ostriker, J. P. 2007, *ApJ*, 665, 1038
- Côté, P., et al. 2006, *ApJS*, 165, 57
- , 2007, *ApJ*, 671, 1456
- Covington, M., Dekel, A., Cox, T. J., Jonsson, P., & Primack, J. R. 2008, *MNRAS*, 384, 94
- Cox, T., et al. 2008, *ApJ*, in preparation
- Cox, T. J., Di Matteo, T., Hernquist, L., Hopkins, P. F., Robertson, B., & Springel, V. 2006a, *ApJ*, 643, 692
- Cox, T. J., Dutta, S. N., Di Matteo, T., Hernquist, L., Hopkins, P. F., Robertson, B., & Springel, V. 2006b, *ApJ*, 650, 791
- Cox, T. J., Jonsson, P., Primack, J. R., & Somerville, R. S. 2006c, *MNRAS*, 373, 1013
- Crane, P., et al. 1993, *AJ*, 106, 1371
- Dasyra, K. M., et al. 2006, *ApJ*, 638, 745
- , 2007, *ApJ*, 657, 102
- Davé, R., Hernquist, L., Katz, N., & Weinberg, D. H. 1999, *ApJ*, 511, 521
- Davis, L. E., Cawson, M., Davies, R. L., & Illingworth, G. 1985, *AJ*, 90, 169
- de Vaucouleurs, G. 1948, *Annales d'Astrophysique*, 11, 247
- Dekel, A., & Cox, T. J. 2006, *MNRAS*, 370, 1445
- Di Matteo, T., Springel, V., & Hernquist, L. 2005, *Nature*, 433, 604
- Doyon, R., Wells, M., Wright, G. S., Joseph, R. D., Nadeau, D., & James, P. A. 1994, *ApJ*, 437, L23
- Emsellem, E., et al. 2007, *MNRAS*, 379, 401
- Erb, D. K., Steidel, C. C., Shapley, A. E., Pettini, M., Reddy, N. A., & Adelberger, K. L. 2006, *ApJ*, 646, 107
- Faber, S. M. 1973, *ApJ*, 179, 423
- Faber, S. M., Tremaine, S., Ajhar, E. A., Byun, Y.-I., Dressler, A., Gebhardt, K., Grillmair, C., Kormendy, J., Lauer, T. R., & Richstone, D. 1997, *AJ*, 114, 1771
- Faber, S. M., Wegner, G., Burstein, D., Davies, R. L., Dressler, A., Lynden-Bell, D., & Terlevich, R. J. 1989, *ApJS*, 69, 763
- Ferrarese, L., & Merritt, D. 2000, *ApJ*, 539, L9
- Ferrarese, L., van den Bosch, F. C., Ford, H. C., Jaffe, W., & O'Connell, R. W. 1994, *AJ*, 108, 1598
- Ferrarese, L., et al. 2006, *ApJS*, 164, 334
- Fontana, A., et al. 2006, *A&A*, 459, 745
- Forbes, D. A., Sánchez-Blázquez, P., & Proctor, R. 2005, *MNRAS*, 361, L6
- Gallazzi, A., Charlot, S., Brinchmann, J., White, S. D. M., & Tremonti, C. A. 2005, *MNRAS*, 362, 41
- Ganda, K., et al. 2007, *MNRAS*, 380, 506
- Gebhardt, K., et al. 2000, *ApJ*, 539, L13
- Geha, M., Guhathakurta, P., & van der Marel, R. P. 2002, *AJ*, 124, 3073
- Genzel, R., Tacconi, L. J., Rigopoulou, D., Lutz, D., & Tecza, M. 2001, *ApJ*, 563, 527
- Gerhard, O. E., & Binney, J. 1985, *MNRAS*, 216, 467
- Goto, T. 2005, *MNRAS*, 357, 937
- Graham, A. W. 2001, *AJ*, 121, 820
- Graham, A. W., Erwin, P., Trujillo, I., & Asensio Ramos, A. 2003, *AJ*, 125, 2951
- Gunn, J. E. 1987, in *Nearly Normal Galaxies. From the Planck Time to the Present*, ed. S. M. Faber, 455–464
- Häring, N., & Rix, H.-W. 2004, *ApJ*, 604, L89
- Harris, W. E. 1996, *AJ*, 112, 1487
- Harris, W. E., Harris, G. L. H., Holland, S. T., & McLaughlin, D. E. 2002, *AJ*, 124, 1435
- Hernquist, L. 1989, *Nature*, 340, 687
- , 1990, *ApJ*, 356, 359
- , 1992, *ApJ*, 400, 460
- , 1993a, *ApJ*, 404, 717
- , 1993b, *ApJ*, 409, 548
- Hernquist, L., & Barnes, J. E. 1991, *Nature*, 354, 210
- Hernquist, L., & Mihos, J. C. 1995, *ApJ*, 448, 41
- Hernquist, L., & Spergel, D. N. 1992, *ApJ*, 399, L117
- Hernquist, L., Spergel, D. N., & Heyl, J. S. 1993, *ApJ*, 416, 415
- Hibbard, J. E., & Yun, M. S. 1999, *ApJ*, 522, L93
- Hoffman, L., et al. 2007, *ApJ*, in preparation
- Hopkins, P. F., Cox, T. J., & Hernquist, L. 2008a, *ApJ*, accepted, arXiv:0806.3974 [astro-ph], 806
- Hopkins, P. F., Cox, T. J., Kereš, D., & Hernquist, L. 2008b, *ApJS*, 175, 390
- Hopkins, P. F., Cox, T. J., Younger, J. D., & Hernquist, L. 2008c, *ApJ*, accepted, arXiv:0806.1739 [astro-ph], 806
- Hopkins, P. F., & Hernquist, L. 2006, *ApJS*, 166, 1
- Hopkins, P. F., Hernquist, L., Cox, T. J., Di Matteo, T., Martini, P., Robertson, B., & Springel, V. 2005a, *ApJ*, 630, 705
- Hopkins, P. F., Hernquist, L., Cox, T. J., Di Matteo, T., Robertson, B., & Springel, V. 2006a, *ApJS*, 163, 1
- Hopkins, P. F., Hernquist, L., Cox, T. J., Dutta, S. N., & Rothberg, B. 2008d, *ApJ*, 679, 156
- Hopkins, P. F., Hernquist, L., Cox, T. J., Keres, D., & Wuyts, S. 2008e, *ApJ*, accepted, arXiv:0807.2868 [astro-ph], 807
- Hopkins, P. F., Hernquist, L., Cox, T. J., & Kereš, D. 2008f, *ApJS*, 175, 356
- Hopkins, P. F., Hernquist, L., Cox, T. J., Robertson, B., Di Matteo, T., & Springel, V. 2006b, *ApJ*, 639, 700
- Hopkins, P. F., Hernquist, L., Cox, T. J., Robertson, B., & Krause, E. 2007a, *ApJ*, 669, 45
- , 2007b, *ApJ*, 669, 67
- Hopkins, P. F., Hernquist, L., Cox, T. J., Robertson, B., & Springel, V. 2006c, *ApJS*, 163, 50
- Hopkins, P. F., Hernquist, L., Cox, T. J., Younger, J. D., & Besla, G. 2008g, *ApJ*, accepted, arXiv:0806.2861 [astro-ph], 806
- Hopkins, P. F., Hernquist, L., Martini, P., Cox, T. J., Robertson, B., Di Matteo, T., & Springel, V. 2005b, *ApJ*, 625, L71
- Hopkins, P. F., Lauer, T. R., Cox, T. J., Hernquist, L., & Kormendy, J. 2008h, *ApJ*, in press, arXiv:0806.2325 [astro-ph], 806
- Hopkins, P. F., Lidz, A., Hernquist, L., Coil, A. L., Myers, A. D., Cox, T. J., & Spergel, D. N. 2007c, *ApJ*, 662, 110
- Hopkins, P. F., Richards, G. T., & Hernquist, L. 2007d, *ApJ*, 654, 731
- James, P., Bate, C., Wells, M., Wright, G., & Doyon, R. 1999, *MNRAS*, 309, 585
- Jedrzejewski, R. I. 1987, *MNRAS*, 226, 747
- Jedrzejewski, R. I., Davies, R. L., & Illingworth, G. D. 1987, *AJ*, 94, 1508
- Jesseit, R., Naab, T., Peletier, R. F., & Burkert, A. 2007, *MNRAS*, 376, 997
- Joseph, R. D., & Wright, G. S. 1985, *MNRAS*, 214, 87
- Kannappan, S. J. 2004, *ApJ*, 611, L89
- Katz, N., Weinberg, D. H., & Hernquist, L. 1996, *ApJS*, 105, 19
- King, I. R. 1978, *ApJ*, 222, 1
- Kobayashi, C. 2004, *MNRAS*, 347, 740
- Kormendy, J. 1977a, *ApJ*, 214, 359
- , 1977b, *ApJ*, 218, 333
- Kormendy, J. 1982, in *Saas-Fee Advanced Course 12: Morphology and Dynamics of Galaxies*, ed. L. Martinet & M. Mayor, 113–288
- , 1985a, *ApJ*, 292, L9
- , 1985b, *ApJ*, 295, 73
- Kormendy, J. 1987a, in *IAU Symposium, Vol. 127, Structure and Dynamics of Elliptical Galaxies*, ed. P. T. de Zeeuw, 17–34
- Kormendy, J. 1987b, in *Nearly Normal Galaxies. From the Planck Time to the Present*, ed. S. M. Faber, 163–174
- , 1989, *ApJ*, 342, L63
- Kormendy, J. 1999, in *Astronomical Society of the Pacific Conference Series, Vol. 182, Galaxy Dynamics - A Rutgers Symposium*, ed. D. R. Merritt, M. Valluri, & J. A. Sellwood, 124–+
- Kormendy, J., Dressler, A., Byun, Y. I., Faber, S. M., Grillmair, C., Lauer, T. R., Richstone, D., & Tremaine, S. 1994, in *Dwarf Galaxies*, ed. G. Meylan & P. Prugniel, 147–+
- Kormendy, J., Fisher, D. B., Cornell, M. E., & Bender, R. 2008, *ApJ*, in press
- Kormendy, J., & Freeman, K. C. 2004, in *IAU Symposium, Vol. 220, Dark Matter in Galaxies*, ed. S. Ryder, D. Pisano, M. Walker, & K. Freeman, 377–+
- Kormendy, J., & Gebhardt, K. 2001, in *AIP Conf. Proc. 586: 20th Texas Symposium on relativistic astrophysics*, ed. J. C. Wheeler & H. Martel, 363–+
- Kormendy, J., Gebhardt, K., Fisher, D. B., Drory, N., Macchetto, F. D., & Sparks, W. B. 2005, *AJ*, 129, 2636
- Kormendy, J., & Richstone, D. 1995, *ARA&A*, 33, 581
- Kormendy, J., & Sanders, D. B. 1992, *ApJ*, 390, L53
- Laine, S., van der Marel, R. P., Lauer, T. R., Postman, M., O'Dea, C. P., & Owen, F. N. 2003, *AJ*, 125, 478
- Lake, G. 1989, *AJ*, 97, 1312
- Lake, G., & Dressler, A. 1986, *ApJ*, 310, 605
- Lauer, T. R. 1985, *ApJS*, 57, 473
- Lauer, T. R., Ajhar, E. A., Byun, Y.-I., Dressler, A., Faber, S. M., Grillmair, C., Kormendy, J., Richstone, D., & Tremaine, S. 1995, *AJ*, 110, 2622

- Lauer, T. R., et al. 1991, *ApJ*, 369, L41  
— 1992, *AJ*, 104, 552  
— 2005, *AJ*, 129, 2138  
— 2007a, *ApJ*, 664, 226  
— 2007b, *ApJ*, 662, 808
- Liu, Y., Zhou, X., Ma, J., Wu, H., Yang, Y., Li, J., & Chen, J. 2005, *AJ*, 129, 2628
- Lynden-Bell, D. 1967, *MNRAS*, 136, 101  
— 1969, *Nature*, 223, 690
- Magorrian, J., et al. 1998, *AJ*, 115, 2285
- Malin, D. F., & Carter, D. 1980, *Nature*, 285, 643  
— 1983, *ApJ*, 274, 534
- Mandelbaum, R., Seljak, U., Kauffmann, G., Hirata, C. M., & Brinkmann, J. 2006, *MNRAS*, 368, 715
- Marconi, A., & Hunt, L. K. 2003, *ApJ*, 589, L21
- Martini, P., & Ho, L. C. 2004, *ApJ*, 610, 233
- Matthews, L. D., et al. 1999, *AJ*, 118, 208
- McDermid, R. M., et al. 2006, *MNRAS*, 373, 906
- McGaugh, S. S. 2005, *ApJ*, 632, 859
- Mehlert, D., Thomas, D., Saglia, R. P., Bender, R., & Wegner, G. 2003, *A&A*, 407, 423
- Merritt, D., & Ferrarese, L. 2001, *ApJ*, 547, 140
- Michard, R. 2006, *A&A*, 449, 519
- Mihos, J. C., & Hernquist, L. 1994a, *ApJ*, 437, L47  
— 1994b, *ApJ*, 427, 112  
— 1994c, *ApJ*, 437, 611  
— 1994d, *ApJ*, 431, L9  
— 1996, *ApJ*, 464, 641
- Milosavljević, M. 2004, *ApJ*, 605, L13
- Milosavljević, M., Merritt, D., Rest, A., & van den Bosch, F. C. 2002, *MNRAS*, 331, L51
- Moorthy, B. K., & Holtzman, J. A. 2006, *MNRAS*, 371, 583
- Naab, T., Jesseit, R., & Burkert, A. 2006a, *MNRAS*, 372, 839
- Naab, T., Johansson, P. H., Ostriker, J. P., & Efstathiou, G. 2007, *ApJ*, 658, 710
- Naab, T., Khochfar, S., & Burkert, A. 2006b, *ApJ*, 636, L81
- Naab, T., & Ostriker, J. P. 2007, *MNRAS*, in press [astro-ph/0702535]
- Naab, T., & Trujillo, I. 2006, *MNRAS*, 369, 625
- Navarro, J. F., Frenk, C. S., & White, S. D. M. 1996, *ApJ*, 462, 563
- Oñorbe, J., Domínguez-Tenreiro, R., Sáiz, A., Artal, H., & Serna, A. 2006, *MNRAS*, 373, 503
- O’Shea, B. W., Nagamine, K., Springel, V., Hernquist, L., & Norman, M. L. 2005, *ApJS*, 160, 1
- Ostriker, J. P. 1980, *Comments on Astrophysics*, 8, 177
- Peletier, R. F., Davies, R. L., Illingworth, G. D., Davis, L. E., & Cawson, M. 1990, *AJ*, 100, 1091
- Peletier, R. F., et al. 2007, *MNRAS*, 379, 445
- Phillips, A. C., Illingworth, G. D., MacKenty, J. W., & Franx, M. 1996, *AJ*, 111, 1566
- Postman, M., & Lauer, T. R. 1995, *ApJ*, 440, 28
- Prugniel, P., & Simien, F. 1997, *A&A*, 321, 111
- Quillen, A. C., Bower, G. A., & Stritzinger, M. 2000, *ApJS*, 128, 85
- Ravindranath, S., Ho, L. C., Peng, C. Y., Filippenko, A. V., & Sargent, W. L. W. 2001, *AJ*, 122, 653
- Reda, F. M., Proctor, R. N., Forbes, D. A., Hau, G. K. T., & Larsen, S. S. 2007, *MNRAS*, 377, 1772
- Reichardt, C., Jimenez, R., & Heavens, A. F. 2001, *MNRAS*, 327, 849
- Rest, A., van den Bosch, F. C., Jaffe, W., Tran, H., Tsvetanov, Z., Ford, H. C., Davies, J., & Schafer, J. 2001, *AJ*, 121, 2431
- Robertson, B., Bullock, J. S., Cox, T. J., Di Matteo, T., Hernquist, L., Springel, V., & Yoshida, N. 2006a, *ApJ*, 645, 986
- Robertson, B., Cox, T. J., Hernquist, L., Franx, M., Hopkins, P. F., Martini, P., & Springel, V. 2006b, *ApJ*, 641, 21
- Robertson, B., Hernquist, L., Cox, T. J., Di Matteo, T., Hopkins, P. F., Martini, P., & Springel, V. 2006c, *ApJ*, 641, 90
- Rothberg, B., & Joseph, R. D. 2004, *AJ*, 128, 2098  
— 2006a, *AJ*, 131, 185  
— 2006b, *AJ*, 132, 976
- Sánchez-Blázquez, P., Forbes, D. A., Strader, J., Brodie, J., & Proctor, R. 2007, *MNRAS*, 377, 759
- Sanders, D. B., & Mirabel, I. F. 1996, *ARA&A*, 34, 749
- Sargent, A. I., Sanders, D. B., & Phillips, T. G. 1989, *ApJ*, 346, L9
- Sargent, A. I., Sanders, D. B., Scoville, N. Z., & Soifer, B. T. 1987, *ApJ*, 312, L35
- Schweizer, F. 1980, *ApJ*, 237, 303  
— 1982, *ApJ*, 252, 455  
— 1996, *AJ*, 111, 109
- Schweizer, F. 1998, in *Saas-Fee Advanced Course 26: Galaxies: Interactions and Induced Star Formation*, ed. R. C. Kennicutt, Jr., F. Schweizer, J. E. Barnes, D. Friedli, L. Martinet, & D. Pfenniger, 105–+
- Schweizer, F., & Seitzer, P. 1992, *AJ*, 104, 1039  
— 1998, *AJ*, 116, 2206  
— 2007, *AJ*, 133, 2132
- Scoville, N. Z., Sanders, D. B., Sargent, A. I., Soifer, B. T., Scott, S. L., & Lo, K. Y. 1986, *ApJ*, 311, L47
- Seth, A. C., Dalcanton, J. J., Hodge, P. W., & Debattista, V. P. 2006, *AJ*, 132, 2539
- Shapley, A. E., Coil, A. L., Ma, C.-P., & Bundy, K. 2005, *ApJ*, 635, 1006
- Shen, S., Mo, H. J., White, S. D. M., Blanton, M. R., Kauffmann, G., Voges, W., Brinkmann, J., & Csabai, I. 2003, *MNRAS*, 343, 978
- Shier, L. M., & Fischer, J. 1998, *ApJ*, 497, 163
- Simien, F., & Prugniel, P. 1997, *A&AS*, 122, 521  
— 2002, *A&A*, 384, 371
- Soifer, B. T., et al. 1984a, *ApJ*, 278, L71  
— 1984b, *ApJ*, 283, L1
- Soltan, A. 1982, *MNRAS*, 200, 115
- Springel, V. 2005, *MNRAS*, 364, 1105
- Springel, V., Di Matteo, T., & Hernquist, L. 2005a, *ApJ*, 620, L79  
— 2005b, *MNRAS*, 361, 776
- Springel, V., & Hernquist, L. 2002, *MNRAS*, 333, 649  
— 2003, *MNRAS*, 339, 289  
— 2005, *ApJ*, 622, L9
- Tacconi, L. J., Genzel, R., Lutz, D., Rigopoulou, D., Baker, A. J., Iserlohe, C., & Tecza, M. 2002, *ApJ*, 580, 73
- Thomas, D., Maraston, C., Bender, R., & Mendes de Oliveira, C. 2005, *ApJ*, 621, 673
- Titus, T. N., Spillar, E. J., & Johnson, P. 1997, *AJ*, 114, 958
- Toomre, A. 1977, in *Evolution of Galaxies and Stellar Populations*, ed. B. M. Tinsley & R. B. Larson, 401
- Toomre, A., & Toomre, J. 1972, *ApJ*, 178, 623
- Trager, S. C., Faber, S. M., Worthey, G., & González, J. J. 2000, *AJ*, 119, 1645
- Tremaine, S., et al. 2002, *ApJ*, 574, 740
- Trujillo, I., Asensio Ramos, A., Rubiño-Martín, J. A., Graham, A. W., Aguerri, J. A. L., Cepa, J., & Gutiérrez, C. M. 2002, *MNRAS*, 333, 510
- van Dokkum, P. G. 2005, *AJ*, 130, 2647
- Vitvitska, M., Klypin, A. A., Kravtsov, A. V., Wechsler, R. H., Primack, J. R., & Bullock, J. S. 2002, *ApJ*, 581, 799
- Walcher, C. J., Böker, T., Charlot, S., Ho, L. C., Rix, H.-W., Rossa, J., Shields, J. C., & van der Marel, R. P. 2006, *ApJ*, 649, 692
- Walcher, C. J., et al. 2005, *ApJ*, 618, 237
- White, S. D. M., & Rees, M. J. 1978, *MNRAS*, 183, 341
- Woods, D. F., Geller, M. J., & Barton, E. J. 2006, *AJ*, 132, 197
- Yamauchi, C., & Goto, T. 2005, *MNRAS*, 359, 1557
- Young, P. J., Westphal, J. A., Kristian, J., Wilson, C. P., & Landauer, F. P. 1978, *ApJ*, 221, 721
- Younger, J. D., Hopkins, P. F., Cox, T. J., & Hernquist, L. 2008, *ApJ*, in press, arXiv:0804.2672 [astro-ph], 804



TABLE 1  
 FITS TO CUSP ELLIPTICALS

Name (1)	Ref. (2)	$N_{\text{phot}}$ (3)	$M_*$ (4)	$M_V$ (5)	$\sigma$ (6)	$R_e$ (7)	$\epsilon$ (8)	$100a_a/a$ (9)	$(v/\sigma)^*$ (10)	$n_s$ (fit) (11)	$n_s$ (sim) (12)	$f_e$ (fit) (13)	$f_{sb}$ (sim) (14)
NGC 0596	2	4	10.89	-20.90	164	3.24	0.07	1.30	0.67	7.50 <sup>+0.59</sup> <sub>-0.74</sub>	3.29 <sup>+1.38</sup> <sub>-0.47</sub>	0.035 <sup>+0.009</sup> <sub>-0.005</sub>	0.185 <sup>+0.125</sup> <sub>-0.097</sub>
NGC 0636	3	3	10.80	-20.83	156	3.81	0.13	0.80	1.04	3.39 <sup>+0.18</sup> <sub>-0.31</sub>	3.07 <sup>+2.05</sup> <sub>-0.63</sub>	0.090 <sup>+0.005</sup> <sub>-0.005</sub>	0.159 <sup>+0.105</sup> <sub>-0.061</sub>
NGC 0821*	2	2	11.36	-21.71	209	3.63	0.38	2.50	0.70	3.38 <sup>+1.57</sup> <sub>-1.57</sub>	3.02 <sup>+0.80</sup> <sub>-0.14</sub>	0.228 <sup>+0.193</sup> <sub>-0.193</sub>	0.154 <sup>+0.182</sup> <sub>-0.064</sub>
NGC 1172	2	1	10.46	-20.13	113	4.37	0.09	-	-	29.92	2.64 <sup>+0.11</sup> <sub>-0.11</sub>	0.001	0.106 <sup>+0.166</sup> <sub>-0.035</sub>
NGC 1199*	3	3	10.95	-21.49	207	3.23	0.23	-	0.49	1.96 <sup>+0.06</sup> <sub>-0.06</sub>	2.58 <sup>+1.60</sup> <sub>-0.80</sub>	0.106 <sup>+0.012</sup> <sub>-0.015</sub>	0.105 <sup>+0.126</sup> <sub>-0.061</sub>
NGC 1400	3	2	9.88	-18.45	250	0.67	0.13	0.00	-	1.91 <sup>+0.06</sup> <sub>-0.06</sub>	2.82 <sup>+8.00</sup> <sub>-0.31</sub>	0.164 <sup>+0.001</sup> <sub>-0.001</sub>	0.232 <sup>+0.114</sup> <sub>-0.095</sub>
NGC 1426	2	3	10.83	-20.78	153	3.63	0.31	0.01	-	5.26 <sup>+0.31</sup> <sub>-0.35</sub>	3.51 <sup>+0.31</sup> <sub>-0.63</sub>	0.001 <sup>+0.001</sup> <sub>-0.001</sub>	0.186 <sup>+0.159</sup> <sub>-0.096</sub>
NGC 1427	2	2	10.83	-20.79	170	3.16	0.29	-	-	2.12 <sup>+1.31</sup> <sub>-1.31</sub>	3.32 <sup>+0.10</sup> <sub>-0.31</sub>	0.251 <sup>+0.199</sup> <sub>-0.199</sub>	0.149 <sup>+0.159</sup> <sub>-0.061</sub>
NGC 1439	2	3	10.85	-20.82	159	4.07	0.15	-	0.32	3.47 <sup>+1.11</sup> <sub>-1.56</sub>	3.30 <sup>+0.39</sup> <sub>-0.89</sub>	0.114 <sup>+0.142</sup> <sub>-0.057</sub>	0.126 <sup>+0.205</sup> <sub>-0.094</sub>
NGC 2314*	3	2	11.34	-21.95	290	3.37	0.18	-	1.17	2.02 <sup>+0.59</sup> <sub>-0.59</sub>	5.32 <sup>+3.07</sup> <sub>-2.64</sub>	0.269 <sup>+0.059</sup> <sub>-0.059</sub>	0.194 <sup>+0.132</sup> <sub>-0.097</sub>
NGC 2434	2	1	11.14	-21.33	229	3.63	0.07	-	-	4.72	2.76 <sup>+1.13</sup> <sub>-0.12</sub>	0.001	0.138 <sup>+0.136</sup> <sub>-0.048</sub>
NGC 2534*	3	1	10.43	-20.25	-	22.67	-	-	-	1.98	4.67 <sup>+0.23</sup> <sub>-0.23</sub>	0.033	0.054 <sup>+0.053</sup> <sub>-0.017</sub>
NGC 2693*	3	2	11.58	-22.59	279	6.65	-	-	-	1.77 <sup>+0.02</sup> <sub>-0.02</sub>	4.57 <sup>+0.11</sup> <sub>-0.21</sub>	0.181 <sup>+0.001</sup> <sub>-0.001</sub>	0.084 <sup>+0.098</sup> <sub>-0.048</sub>
NGC 2768*	3	2	11.01	-21.56	198	6.78	0.68	-	0.28	2.63 <sup>+0.21</sup> <sub>-0.21</sub>	2.55 <sup>+3.91</sup> <sub>-0.89</sub>	0.011 <sup>+0.004</sup> <sub>-0.004</sub>	0.037 <sup>+0.066</sup> <sub>-0.007</sub>
NGC 2778	2	1	9.67	-18.75	166	1.62	0.20	3.50	2.00	2.15	4.62 <sup>+1.83</sup> <sub>-1.83</sub>	0.447	0.230 <sup>+0.125</sup> <sub>-0.115</sub>
NGC 2974	2,3	5	11.00	-21.09	143	4.07	0.30	0.50	1.54	4.06 <sup>+0.77</sup> <sub>-0.48</sub>	3.06 <sup>+0.63</sup> <sub>-0.63</sub>	0.049 <sup>+0.007</sup> <sub>-0.034</sub>	0.158 <sup>+0.142</sup> <sub>-0.103</sub>
NGC 3193	3	2	10.51	-20.30	205	1.81	-	0.30	0.80	2.73 <sup>+0.21</sup> <sub>-0.21</sub>	4.15 <sup>+0.91</sup> <sub>-1.97</sub>	0.089 <sup>+0.010</sup> <sub>-0.010</sub>	0.205 <sup>+0.097</sup> <sub>-0.097</sub>
NGC 3309*	3	3	11.39	-22.24	266	6.67	0.15	-	-	1.97 <sup>+0.46</sup> <sub>-0.46</sub>	2.66 <sup>+1.92</sup> <sub>-0.70</sub>	0.148 <sup>+0.031</sup> <sub>-0.031</sub>	0.077 <sup>+0.104</sup> <sub>-0.046</sub>
NGC 3311*	3	3	11.91	-23.14	210	12.15	0.11	-	-	1.36 <sup>+0.00</sup> <sub>-0.58</sub>	4.47 <sup>+0.27</sup> <sub>-2.56</sub>	0.086 <sup>+0.073</sup> <sub>-0.002</sub>	0.047 <sup>+0.055</sup> <sub>-0.001</sub>
NGC 3377	1,2,3	6	10.42	-20.07	141	2.24	0.50	0.50	0.72	1.96 <sup>+0.67</sup> <sub>-0.50</sub>	3.27 <sup>+0.73</sup> <sub>-0.50</sub>	0.133 <sup>+0.064</sup> <sub>-0.051</sub>	0.221 <sup>+0.123</sup> <sub>-0.115</sub>
NGC 3605	2	3	10.16	-19.61	120	1.58	0.34	-0.90	0.74	1.31 <sup>+0.28</sup> <sub>-0.66</sub>	3.04 <sup>+2.08</sup> <sub>-0.95</sub>	0.175 <sup>+0.150</sup> <sub>-0.041</sub>	0.283 <sup>+0.176</sup> <sub>-0.165</sub>
NGC 3610	2,3	6	10.93	-21.16	163	1.45	0.52	2.50	1.10	4.78 <sup>+7.11</sup> <sub>-3.60</sub>	3.04 <sup>+0.40</sup> <sub>-0.87</sub>	0.342 <sup>+0.099</sup> <sub>-0.012</sub>	0.273 <sup>+0.133</sup> <sub>-0.126</sub>
NGC 3818*	3	2	10.24	-19.69	206	1.61	0.39	2.30	0.93	2.81 <sup>+0.06</sup> <sub>-0.06</sub>	3.54 <sup>+1.13</sup> <sub>-1.13</sub>	0.080 <sup>+0.005</sup> <sub>-0.005</sub>	0.205 <sup>+0.152</sup> <sub>-0.096</sub>
NGC 3894*	3	1	11.15	-21.70	-	4.63	-	-	-	2.07	3.20 <sup>+0.86</sup> <sub>-0.47</sub>	0.050	0.036 <sup>+0.069</sup> <sub>-0.008</sub>
NGC 3904*	3	2	10.93	-21.07	215	3.05	-	0.00	0.36	2.34 <sup>+0.17</sup> <sub>-0.17</sub>	6.06 <sup>+2.84</sup> <sub>-4.04</sub>	0.094 <sup>+0.009</sup> <sub>-0.009</sub>	0.109 <sup>+0.140</sup> <sub>-0.019</sub>
NGC 3923*	3	3	11.36	-22.00	216	5.92	-	-	-	2.90 <sup>+0.12</sup> <sub>-0.26</sub>	2.76 <sup>+0.71</sup> <sub>-2.76</sub>	0.057 <sup>+0.007</sup> <sub>-0.002</sub>	0.037 <sup>+0.070</sup> <sub>-0.007</sub>
NGC 3962*	3	1	10.85	-21.04	211	10.31	-	-	-	3.74	4.72 <sup>+0.08</sup> <sub>-2.22</sub>	0.090	0.105 <sup>+0.122</sup> <sub>-0.049</sub>
NGC 4125	3	2	11.39	-22.53	229	4.97	-	0.95	0.93	2.33 <sup>+0.09</sup> <sub>-0.09</sub>	3.65 <sup>+0.24</sup> <sub>-1.31</sub>	0.031 <sup>+0.003</sup> <sub>-0.003</sub>	0.032 <sup>+0.069</sup> <sub>-0.004</sub>
NGC 4318	1	1	9.83	-16.26	101	0.59	0.34	0.40	-	1.12	2.36 <sup>+0.42</sup> <sub>-0.17</sub>	0.077	0.336 <sup>+0.168</sup> <sub>-0.146</sub>
NGC 4382*	1,2,3	4	11.26	-22.43	196	8.43	0.19	0.59	0.33	3.89 <sup>+1.11</sup> <sub>-1.35</sub>	3.11 <sup>+0.63</sup> <sub>-0.80</sub>	0.034 <sup>+0.008</sup> <sub>-0.010</sub>	0.090 <sup>+0.086</sup> <sub>-0.054</sub>
NGC 4387	1,2,3	5	9.95	-19.11	84	1.46	0.43	-1.00	0.70	2.04 <sup>+0.97</sup> <sub>-0.22</sub>	2.42 <sup>+0.97</sup> <sub>-2.42</sub>	0.007 <sup>+0.002</sup> <sub>-0.002</sub>	0.287 <sup>+0.148</sup> <sub>-0.147</sub>
NGC 4434	1	1	10.59	-19.55	118	1.44	0.08	0.44	-	2.62	2.87 <sup>+0.05</sup> <sub>-0.46</sub>	0.150	0.323 <sup>+0.137</sup> <sub>-0.111</sub>
NGC 4458	1	1	10.36	-18.89	85	1.34	0.12	0.41	0.32	2.72	2.87 <sup>+0.84</sup> <sub>-0.09</sub>	0.075	0.276 <sup>+0.128</sup> <sub>-0.135</sub>
NGC 4459	1	1	10.56	-20.88	168	3.30	0.18	0.22	0.96	3.09	3.68 <sup>+0.14</sup> <sub>-0.67</sub>	0.028	0.194 <sup>+0.135</sup> <sub>-0.096</sub>
NGC 4464	1	1	10.26	-18.40	120	0.55	0.30	0.40	-	2.11	2.36 <sup>+0.69</sup> <sub>-0.17</sub>	0.228	0.368 <sup>+0.170</sup> <sub>-0.134</sub>
NGC 4467	1	1	9.71	-16.87	67	0.39	0.32	0.60	0.35	1.89	2.36 <sup>+1.26</sup> <sub>-0.17</sub>	0.028	0.355 <sup>+0.152</sup> <sub>-0.130</sub>
NGC 4473	1	1	11.13	-20.82	192	3.14	0.39	1.03	0.28	3.60	2.92 <sup>+0.59</sup> <sub>-0.27</sub>	0.148	0.216 <sup>+0.130</sup> <sub>-0.101</sub>
NGC 4476*	3	3	10.25	-19.85	41	1.57	0.28	-	0.60	1.19 <sup>+0.26</sup> <sub>-0.37</sub>	2.59 <sup>+1.89</sup> <sub>-0.76</sub>	0.355 <sup>+0.114</sup> <sub>-0.066</sub>	0.233 <sup>+0.113</sup> <sub>-0.096</sub>
NGC 4478	1,3	3	10.29	-19.77	149	1.15	0.19	-0.80	0.95	2.21 <sup>+0.00</sup> <sub>-0.18</sub>	2.89 <sup>+0.90</sup> <sub>-1.29</sub>	0.223 <sup>+0.003</sup> <sub>-0.195</sub>	0.296 <sup>+0.206</sup> <sub>-0.130</sub>
NGC 4486a	1	1	10.36	-18.84	154	0.50	0.45	4.00	-	2.40	2.41 <sup>+0.99</sup> <sub>-0.08</sub>	0.338	0.368 <sup>+0.158</sup> <sub>-0.120</sub>
NGC 4486b	1	1	9.90	-17.70	200	0.19	0.40	0.80	0.59	2.18	2.41 <sup>+0.69</sup> <sub>-0.08</sub>	0.073	0.325 <sup>+0.135</sup> <sub>-0.144</sub>
NGC 4494	2,3	7	11.24	-21.50	155	3.72	0.15	0.30	1.24	1.97 <sup>+0.63</sup> <sub>-0.07</sub>	3.06 <sup>+1.51</sup> <sub>-1.64</sub>	0.071 <sup>+0.007</sup> <sub>-0.018</sub>	0.117 <sup>+0.144</sup> <sub>-0.027</sub>
NGC 4515	1	1	10.03	-18.52	90	0.87	0.14	2.00	0.47	3.87	2.48 <sup>+0.79</sup> <sub>-0.76</sub>	0.254	0.336 <sup>+0.133</sup> <sub>-0.087</sub>
NGC 4551	1,2	5	10.02	-19.08	100	1.25	0.32	-0.70	0.55	1.85 <sup>+0.24</sup> <sub>-0.58</sub>	2.79 <sup>+0.59</sup> <sub>-1.19</sub>	0.040 <sup>+0.025</sup> <sub>-0.014</sub>	0.300 <sup>+0.155</sup> <sub>-0.132</sub>
NGC 4564	2,3	7	10.53	-19.66	153	2.75	0.45	2.20	1.05	1.62 <sup>+0.75</sup> <sub>-0.47</sub>	3.13 <sup>+1.60</sup> <sub>-2.04</sub>	0.108 <sup>+0.087</sup> <sub>-0.029</sub>	0.141 <sup>+0.235</sup> <sub>-0.050</sub>
NGC 4621	1,2,3	7	11.26	-21.41	237	6.51	0.34	1.50	0.81	3.23 <sup>+1.51</sup> <sub>-0.75</sub>	3.06 <sup>+1.70</sup> <sub>-0.18</sub>	0.053 <sup>+0.005</sup> <sub>-0.044</sub>	0.140 <sup>+0.168</sup> <sub>-0.050</sub>
NGC 4660	2	2	10.46	-19.41	191	1.05	0.40	2.70	1.04	1.88 <sup>+0.41</sup> <sub>-0.38</sub>	2.87 <sup>+0.56</sup> <sub>-0.32</sub>	0.402 <sup>+0.161</sup> <sub>-0.161</sub>	0.323 <sup>+0.179</sup> <sub>-0.140</sub>
NGC 4697	2,3	4	11.23	-21.49	165	5.13	0.41	1.40	0.78	3.51 <sup>+0.38</sup> <sub>-2.05</sub>	2.87 <sup>+0.92</sup> <sub>-0.74</sub>	0.001 <sup>+0.010</sup> <sub>-0.001</sub>	0.103 <sup>+0.140</sup> <sub>-0.068</sub>
NGC 4742	2,3	4	10.30	-19.79	93	1.24	-	0.41	1.62	2.06 <sup>+0.33</sup> <sub>-0.08</sub>	3.28 <sup>+3.09</sup> <sub>-0.61</sub>	0.232 <sup>+0.012</sup> <sub>-0.045</sub>	0.249 <sup>+0.100</sup> <sub>-0.066</sub>
NGC 5018*	3	2	11.36	-22.29	223	4.17	0.25	-	-	4.07 <sup>+0.15</sup> <sub>-0.15</sub>	2.72 <sup>+0.57</sup> <sub>-2.72</sub>	0.040 <sup>+0.005</sup> <sub>-0.005</sub>	0.106 <sup>+0.124</sup> <sub>-0.039</sub>
NGC 5127*	3	1	11.15	-21.87	-	8.32	-	-	-	2.90	2.30 <sup>+1.76</sup> <sub>-0.20</sub>	0.032	0.046 <sup>+0.057</sup> <sub>-0.016</sub>
NGC 5444*	3	3	11.20	-21.91	221	5.46	-	-	-	2.94 <sup>+2.03</sup> <sub>-1.03</sub>	3.13 <sup>+1.58</sup> <sub>-0.50</sub>	0.078 <sup>+0.005</sup> <sub>-0.078</sub>	0.105 <sup>+0.117</sup> <sub>-0.068</sub>
NGC 5576	3	3	10.81	-20.82	187	3.52	0.30	-0.50	0.22	3.90 <sup>+1.06</sup> <sub>-0.96</sub>	3.06 <sup>+0.56</sup> <sub>-0.56</sub>	0.082 <sup>+0.018</sup> <sub>-0.018</sub>	0.200 <sup>+0.113</sup> <sub>-0.098</sub>
NGC 5638*	3	3	10.65	-20.60	159	1.99	0.08	0.20	0.72	1.33 <sup>+0.38</sup> <sub>-0.58</sub>	4.01 <sup>+2.06</sup> <sub>-1.66</sub>	0.169 <sup>+0.070</sup> <sub>-0.070</sub>	0.129 <sup>+0.178</sup> <sub>-0.038</sub>
NGC 5812	3,4	4	10.97	-21.12	204	2.63	0.05	0.00	0.52	3.17 <sup>+0.08</sup> <sub>-0.63</sub>	3.86 <sup>+0.94</sup> <sub>-1.40</sub>	0.133 <sup>+0.022</sup> <sub>-0.004</sub>	0.221 <sup>+0.106</sup> <sub>-0.106</sub>
NGC 5831	3	3	10.68	-20.42	166	2.56	0.17	-	0.19	3.47 <sup>+0.30</sup> <sub>-1.06</sub>	3.40 <sup>+4.40</sup> <sub>-2.00</sub>	0.054 <sup>+0.021</sup> <sub>-0.001</sub>	0.205 <sup>+0.140</sup> <sub>-0.103</sub>
NGC 5845	3	3	10.38	-19.46	251	0.51	0.15	0.80	0.91	1.18 <sup>+0.34</sup> <sub>-0.02</sub>	2.59 <sup>+6.31</sup> <sub>-1.91</sub>	0.455 <sup>+0.027</sup> <sub>-0.077</sub>	0.404 <sup>+0.123</sup> <sub>-0.117</sub>
NGC 6482*	3	2	11.57	-22.76	287	4.51	0.27	-	-	2.13 <sup>+0.05</sup> <sub>-0.32</sub>	3.57 <sup>+0.90</sup> <sub>-1.47</sub>	0.062 <sup>+0.001</sup> <sub>-0.001</sub>	0.084 <sup>+0.120</sup> <sub>-0.055</sub>
NGC 6487*	3	3	11.54	-23.11	-	12.91	-	-	-	2.26 <sup>+0.92</sup> <sub>-0.02</sub>	4.95 <sup>+3.44</sup> <sub>-3.05</sub>	0.101 <sup>+0.002</sup> <sub>-0.018</sub>	0.089 <sup>+0.046</sup> <sub>-0.043</sub>
NGC 7562	3	2	11.42	-22.27	243	6.01	0.29	-	-	2.49 <sup>+0.10</sup> <sub>-0.10</sub>	2.95 <sup>+0.33</sup> <sub>-0.48</sub>	0.079 <sup>+0.009</sup> <sub>-0.009</sub>	0.046 <sup>+0.073</sup> <sub>-0.017</sub>
NGC 7626	3	3	11.67	-22.62	234	8.81	0.13	0.11	0.12	2.94 <sup>+0.20</sup> <sub>-0.04</sub>	3.39 <sup>+1.00</sup> <sub>-1.43</sub>	0.042 <sup>+0.001</sup> <sub>-0.007</sub>	0.070 <sup>+0.056</sup> <sub>-0.038</sub>
VCC 1199	1	1	8.97	-15.52	69	0.17	0.28	0.05	-	1.91	2.42 <sup>+0.68</sup> <sub>-0.34</sub>	0.049	0.322 <sup>+0.120</sup> <sub>-0.149</sub>
VCC 1440	1	1	9.13										

TABLE 1 — *Continued*

Name (1)	Ref. (2)	$N_{\text{phot}}$ (3)	$M_*$ (4)	$M_V$ (5)	$\sigma$ (6)	$R_e$ (7)	$\epsilon$ (8)	$100a_4/a$ (9)	$(v/\sigma)^*$ (10)	$n_s$ (fit) (11)	$n_s$ (sim) (12)	$f_e$ (fit) (13)	$f_{sb}$ (sim) (14)
VCC 1627	1	1	9.11	-16.43	—	0.30	0.20	0.40	—	2.26	2.42 <sup>+0.68</sup> <sub>-0.34</sub>	0.018	0.346 <sup>+0.158</sup> <sub>-0.142</sub>
VCC 1871	1	1	9.27	-17.33	51	0.61	0.14	0.80	—	1.90	2.36 <sup>+1.26</sup> <sub>-0.17</sub>	0.010	0.403 <sup>+0.239</sup> <sub>-0.155</sub>
UGC 10638	2	1	11.90	-22.66	—	14.79	—	—	—	4.83	2.53 <sup>+0.97</sup> <sub>-0.36</sub>	0.001	0.088 <sup>+0.093</sup> <sub>-0.042</sub>
ESO 462-15	2	2	11.99	-22.83	289	7.24	0.27	—	—	2.65 <sup>+1.14</sup> <sub>-1.14</sub>	3.13 <sup>+1.47</sup> <sub>-0.61</sub>	0.141 <sup>+0.140</sup> <sub>-0.140</sub>	0.099 <sup>+0.127</sup> <sub>-0.067</sub>
IC 2738	2	1	11.64	-22.21	—	23.09	—	—	—	6.33	3.09 <sup>+0.15</sup> <sub>-0.18</sub>	0.024	0.090 <sup>+0.092</sup> <sub>-0.029</sub>
A0147-M1*	2	1	11.86	-22.60	—	11.34	—	—	—	3.86	3.54 <sup>+0.18</sup> <sub>-0.47</sub>	0.030	0.078 <sup>+0.063</sup> <sub>-0.017</sub>
A0160-M1*	2	1	12.19	-23.18	—	21.72	—	—	—	1.54	2.64 <sup>+0.57</sup> <sub>-0.11</sub>	0.116	0.047 <sup>+0.058</sup> <sub>-0.002</sub>
A0189-M1	2	1	11.46	-21.89	—	9.33	—	—	—	3.69	2.59 <sup>+0.02</sup> <sub>-0.27</sub>	0.017	0.090 <sup>+0.099</sup> <sub>-0.054</sub>
A0261-M1	2	1	12.06	-22.95	—	22.91	—	—	—	6.85	3.09 <sup>+0.15</sup> <sub>-0.92</sub>	0.071	0.090 <sup>+0.078</sup> <sub>-0.043</sub>
A0419-M1	2	1	11.40	-21.79	—	8.13	—	—	—	2.11	2.59 <sup>+0.02</sup> <sub>-0.27</sub>	0.153	0.098 <sup>+0.096</sup> <sub>-0.061</sub>
A0912-M1	2	3	11.66	-22.24	—	9.55	—	—	—	3.08 <sup>+0.24</sup> <sub>-0.24</sub>	2.59 <sup>+0.10</sup> <sub>-0.25</sub>	0.065 <sup>+0.011</sup> <sub>-0.011</sub>	0.105 <sup>+0.116</sup> <sub>-0.045</sub>
A1308-M1*	2	1	12.34	-23.44	—	26.66	—	—	—	4.60	3.09 <sup>+0.15</sup> <sub>-0.56</sub>	0.043	0.077 <sup>+0.058</sup> <sub>-0.030</sub>
A1836-M1*	2	2	12.29	-23.34	—	22.05	—	—	—	4.23 <sup>+0.13</sup> <sub>-0.13</sub>	2.82 <sup>+0.45</sup> <sub>-0.83</sub>	0.018 <sup>+0.001</sup> <sub>-0.001</sub>	0.073 <sup>+0.045</sup> <sub>-0.027</sub>
A1983-M1*	2	1	11.72	-22.35	—	7.41	—	—	—	3.79	3.06 <sup>+0.33</sup> <sub>-0.05</sub>	0.033	0.105 <sup>+0.120</sup> <sub>-0.051</sub>

Compiled and fitted parameters for the confirmed cusp ellipticals in our observed samples. Columns show: (1) Object name. (2) Source for surface brightness profiles, where 1 =Kormendy et al. (2008), 2 =Lauer et al. (2007a), 3 =Bender et al. (1988), 4 =Rothberg & Joseph (2004). (3) Total number of different surface brightness profiles in our combined samples for the given object. (4) Stellar mass [ $\log M_*/M_\odot$ ]. (5)  $V$ -band absolute magnitude. (6) Velocity dispersion [km/s]. (7) Effective (half-light) radius of the *total* light profile [kpc]. (8) Ellipticity. (9) Boxy/diskyness. (10) Rotation. (11) Outer Sérsic index  $n_s$  of the two-component best-fit profile. Where multiple profiles are available for the same object, we show the median and minimum/maximum range of fitted  $n_s$  values. (12) Range of outer Sérsic indices fit in the same manner to the best-fit simulations, at  $t \approx 1 - 3$  Gyr after the merger when the system has relaxed. (13) Fraction of light in the inner or “extra light” component of the fits. Where multiple profiles are available for the same object, we show the median and minimum/maximum range of fitted values. (14) Fraction of light from stars produced in the central, merger-induced starburst in the best-fit simulations ( $\pm$  the approximate interquartile range allowed). This list includes all systems morphologically classified as ellipticals in Kormendy et al. (2008) (all are E0-E4), or (where not in that sample) Lauer et al. (2007a) (all are E or E/BCG).

\* Systems with ambiguous or uncertain cusp status. These are systems for which different sources disagree on their cusp/core status, or for which observations of the central regions are unavailable/ambiguous but for which some other evidence (e.g. stellar populations, gas/dust content, or kinematics) suggest a gas-rich merger origin. We include them here for completeness, but our conclusions are insensitive to their inclusion/exclusion, and they are not generally shown in our analysis.

TABLE 2  
 FITS TO RECENT MERGER REMNANTS

Name (1)	Ref. (2)	$N_{\text{phot}}$ (3)	$M_*$ (4)	$M_K$ (5)	$\sigma$ (6)	$R_e$ (7)	$\epsilon$ (8)	$100a_4/a$ (9)	$(v/\sigma)^*$ (10)	$n_s$ (fit) (11)	$n_s$ (sim) (12)	$f_e$ (fit) (13)	$f_{sb}$ (sim) (14)
NGC 34	4	1	11.09	-24.61	201	0.84	0.11	1.36	1.41	3.49	4.62 <sup>+0.50</sup> <sub>-1.83</sub>	0.389	0.388 <sup>+0.120</sup> <sub>-0.098</sub>
NGC 455	4	1	11.10	-24.64	234	3.33	0.21	-0.41	1.08	2.02	3.20 <sup>+1.61</sup> <sub>-0.10</sub>	0.200	0.194 <sup>+0.105</sup> <sub>-0.089</sub>
NGC 828	4	1	11.40	-25.36	–	3.51	0.41	1.70	–	3.60	3.65 <sup>+0.24</sup> <sub>-1.30</sub>	0.189	0.231 <sup>+0.154</sup> <sub>-0.128</sub>
NGC 1210	4	1	10.72	-23.72	247	2.43	0.08	0.25	0.46	1.92	3.32 <sup>+0.31</sup> <sub>-0.31</sub>	0.158	0.231 <sup>+0.117</sup> <sub>-0.108</sub>
NGC 1614	4	1	11.15	-24.74	146	1.69	0.13	0.76	1.91	2.29	3.30 <sup>+0.39</sup> <sub>-0.64</sub>	0.351	0.300 <sup>+0.107</sup> <sub>-0.110</sub>
NGC 2418	4	1	11.38	-25.31	288	4.81	0.16	-0.25	0.66	2.10	3.29 <sup>+1.38</sup> <sub>-0.77</sub>	0.128	0.168 <sup>+0.169</sup> <sub>-0.077</sub>
NGC 2623	4	1	10.93	-24.22	191	1.32	0.24	2.39	0.37	4.88	5.32 <sup>+0.07</sup> <sub>-2.64</sub>	0.173	0.300 <sup>+0.095</sup> <sub>-0.126</sub>
NGC 2655	4	1	10.72	-23.70	169	1.14	0.19	0.05	1.00	2.44	2.76 <sup>+1.13</sup> <sub>-0.12</sub>	0.055	0.322 <sup>+0.126</sup> <sub>-0.110</sub>
NGC 2744	4	1	10.36	-22.83	–	3.44	0.51	-6.42	–	1.75	2.36 <sup>+0.69</sup> <sub>-0.46</sub>	0.050	0.128 <sup>+0.208</sup> <sub>-0.052</sub>
NGC 2782	4	1	10.77	-23.83	196	3.30	0.26	1.03	0.85	1.74	4.67 <sup>+0.45</sup> <sub>-1.73</sub>	0.229	0.210 <sup>+0.126</sup> <sub>-0.101</sub>
NGC 2914	4	1	10.64	-23.51	186	1.39	0.35	0.68	1.26	0.62	2.53 <sup>+0.97</sup> <sub>-0.36</sub>	0.498	0.244 <sup>+0.113</sup> <sub>-0.107</sub>
NGC 3256	4	1	11.14	-24.72	241	1.79	0.19	1.35	0.41	1.85	4.57 <sup>+0.11</sup> <sub>-2.61</sub>	0.090	0.299 <sup>+0.163</sup> <sub>-0.129</sub>
NGC 3310 <sup>†</sup>	4	1	10.04	-22.07	–	0.70	0.22	-2.00	–	1.59	2.55 <sup>+5.91</sup> <sub>-0.89</sub>	0.078	0.323 <sup>+0.132</sup> <sub>-0.129</sub>
NGC 3597	4	1	10.72	-23.72	174	0.83	0.40	1.11	0.95	0.64	3.06 <sup>+1.12</sup> <sub>-0.63</sub>	0.614	0.358 <sup>+0.169</sup> <sub>-0.133</sub>
NGC 3656	4	1	10.72	-23.70	132	2.55	0.12	-1.70	–	3.45	2.94 <sup>+0.42</sup> <sub>-0.70</sub>	0.038	0.195 <sup>+0.093</sup> <sub>-0.085</sub>
NGC 3921	4	1	11.31	-25.13	222	3.45	0.21	0.99	1.02	2.48	4.15 <sup>+0.97</sup> <sub>-1.92</sub>	0.261	0.297 <sup>+0.120</sup> <sub>-0.085</sub>
NGC 4004 <sup>†</sup>	4	1	10.38	-22.89	33	3.17	0.62	2.58	0.47	1.50	2.66 <sup>+1.92</sup> <sub>-0.70</sub>	0.422	0.194 <sup>+0.143</sup> <sub>-0.139</sub>
NGC 4194	4	1	10.51	-23.21	116	0.57	0.24	0.91	1.24	1.57	3.64 <sup>+1.10</sup> <sub>-1.74</sub>	0.535	0.355 <sup>+0.199</sup> <sub>-0.091</sub>
NGC 4441	4	1	10.42	-22.98	139	1.53	0.17	0.87	0.94	2.47	3.27 <sup>+0.73</sup> <sub>-0.50</sub>	0.140	0.194 <sup>+0.133</sup> <sub>-0.081</sub>
NGC 5018	4	1	11.32	-25.15	222	2.62	0.25	1.17	0.74	3.14	2.53 <sup>+2.39</sup> <sub>-0.44</sub>	0.062	0.194 <sup>+0.126</sup> <sub>-0.086</sub>
NGC 6052 <sup>†</sup>	4	1	10.65	-23.55	80	4.82	0.44	1.38	0.60	0.85	3.54 <sup>+0.92</sup> <sub>-1.13</sub>	0.044	0.118 <sup>+0.190</sup> <sub>-0.050</sub>
NGC 6598	4	1	11.46	-25.51	–	6.08	0.16	-0.03	–	3.39	3.20 <sup>+0.86</sup> <sub>-0.47</sub>	0.045	0.103 <sup>+0.102</sup> <sub>-0.067</sub>
NGC 7135	4	1	10.82	-23.95	277	4.36	0.18	0.39	0.82	4.13	6.06 <sup>+2.84</sup> <sub>-4.04</sub>	0.081	0.166 <sup>+0.077</sup> <sub>-0.146</sub>
NGC 7252	4	1	11.19	-24.84	166	2.53	0.07	0.24	1.42	1.27	2.76 <sup>+3.31</sup> <sub>-2.76</sub>	0.316	0.249 <sup>+0.146</sup> <sub>-0.124</sub>
NGC 7585	4	1	11.24	-24.98	211	4.45	0.29	0.33	0.21	2.41	4.72 <sup>+0.88</sup> <sub>-2.22</sub>	0.107	0.141 <sup>+0.178</sup> <sub>-0.043</sub>
NGC 7727	4	1	10.93	-24.23	231	2.28	0.24	-1.63	1.18	2.63	3.02 <sup>+0.80</sup> <sub>-0.14</sub>	0.127	0.249 <sup>+0.120</sup> <sub>-0.049</sub>
UGC 6	4	1	10.84	-24.01	220	1.40	0.19	-0.04	0.56	2.10	2.92 <sup>+0.39</sup> <sub>-0.27</sub>	0.630	0.345 <sup>+0.124</sup> <sub>-0.115</sub>
UGC 2238 <sup>†</sup>	4	1	11.08	-24.58	–	1.42	0.53	2.60	–	1.09	2.87 <sup>+0.05</sup> <sub>-0.46</sub>	0.165	0.315 <sup>+0.122</sup> <sub>-0.150</sub>
UGC 4079	4	1	10.75	-23.78	–	3.65	0.54	-1.06	–	2.28	2.87 <sup>+0.84</sup> <sub>-0.09</sub>	0.040	0.103 <sup>+0.124</sup> <sub>-0.066</sub>
UGC 4635	4	1	11.13	-24.71	251	2.48	0.34	0.76	0.65	2.90	3.68 <sup>+0.14</sup> <sub>-0.67</sub>	0.077	0.270 <sup>+0.133</sup> <sub>-0.142</sub>
UGC 5101	4	1	11.46	-25.50	287	1.07	0.18	0.62	1.29	4.60	2.36 <sup>+0.26</sup> <sub>-0.17</sub>	0.318	0.359 <sup>+0.088</sup> <sub>-0.152</sub>
UGC 8058*	4	1	12.31	-27.55	–	0.82	0.05	-0.30	–	4.60	3.51 <sup>+0.31</sup> <sub>-0.63</sub>	0.769	0.447 <sup>+0.200</sup> <sub>-0.157</sub>
UGC 9829 <sup>†</sup>	4	1	11.24	-24.96	134	6.61	0.41	2.62	1.00	1.37	2.59 <sup>+1.89</sup> <sub>-0.78</sub>	0.021	0.117 <sup>+0.157</sup> <sub>-0.034</sub>
UGC 10607	4	1	11.34	-25.20	211	1.59	0.24	0.26	0.99	1.69	2.36 <sup>+0.42</sup> <sub>-0.17</sub>	0.332	0.302 <sup>+0.102</sup> <sub>-0.139</sub>
UGC 10675	4	1	11.17	-24.80	177	1.46	0.18	0.72	0.57	2.18	3.11 <sup>+0.63</sup> <sub>-0.80</sub>	0.638	0.368 <sup>+0.139</sup> <sub>-0.105</sub>
UGC 11905	4	1	11.05	-24.51	222	1.89	0.24	-0.76	0.64	1.21	2.42 <sup>+0.97</sup> <sub>-2.42</sub>	0.417	0.300 <sup>+0.113</sup> <sub>-0.089</sub>
AM 0318-230	4	1	11.29	-25.09	–	3.64	0.17	-0.04	–	2.27	3.54 <sup>+0.15</sup> <sub>-0.47</sub>	0.283	0.264 <sup>+0.104</sup> <sub>-0.135</sub>
AM 0612-373	4	1	11.52	-25.65	303	4.71	0.11	-0.64	0.80	1.55	2.64 <sup>+0.57</sup> <sub>-0.11</sub>	0.163	0.102 <sup>+0.081</sup> <sub>-0.065</sub>
AM 0956-282	4	1	9.39	-20.50	–	2.18	–	–	–	2.25	2.59 <sup>+0.02</sup> <sub>-0.27</sub>	0.210	0.221 <sup>+0.106</sup> <sub>-0.085</sub>
AM 1158-333	4	1	10.26	-22.61	–	1.41	0.30	1.50	–	2.99	3.09 <sup>+0.15</sup> <sub>-0.92</sub>	0.316	0.307 <sup>+0.114</sup> <sub>-0.086</sub>
AM 1255-430	4	1	11.22	-24.93	243	5.18	0.28	-0.65	0.33	0.87	2.59 <sup>+0.02</sup> <sub>-0.10</sub>	0.261	0.248 <sup>+0.168</sup> <sub>-0.139</sub>
AM 1300-233	4	1	11.11	-24.65	–	4.28	0.68	-0.90	–	1.92	2.59 <sup>+1.10</sup> <sub>-0.25</sub>	0.102	0.118 <sup>+0.122</sup> <sub>-0.044</sub>
AM 1419-263	4	1	11.23	-24.94	260	3.61	0.27	0.38	0.43	3.15	3.09 <sup>+0.13</sup> <sub>-0.18</sub>	0.057	0.114 <sup>+0.121</sup> <sub>-0.037</sub>
AM 2038-382	4	1	11.13	-24.70	257	1.77	0.17	-0.03	1.21	2.51	3.09 <sup>+0.15</sup> <sub>-0.45</sub>	0.497	0.355 <sup>+0.112</sup> <sub>-0.196</sub>
AM 2055-425	4	1	11.29	-25.08	185	2.09	0.05	0.75	0.88	0.75	2.82 <sup>+0.29</sup> <sub>-0.45</sub>	0.344	0.248 <sup>+0.133</sup> <sub>-0.122</sub>
AM 2246-490	4	1	11.47	-25.52	267	4.16	0.05	0.31	0.54	2.82	3.06 <sup>+0.83</sup> <sub>-0.05</sub>	0.320	0.197 <sup>+0.122</sup> <sub>-0.092</sub>
Arp 156	4	1	11.59	-25.81	288	6.95	0.17	1.59	1.20	3.14	3.13 <sup>+1.47</sup> <sub>-0.61</sub>	0.116	0.168 <sup>+0.065</sup> <sub>-0.082</sub>
Arp 187	4	1	11.36	-25.25	–	4.37	0.47	2.11	–	3.93	3.07 <sup>+2.03</sup> <sub>-0.63</sub>	0.062	0.141 <sup>+0.093</sup> <sub>-0.064</sub>
Arp 193	4	1	11.00	-24.40	172	1.58	0.49	0.82	0.65	1.17	3.02 <sup>+0.80</sup> <sub>-0.44</sub>	0.332	0.296 <sup>+0.120</sup> <sub>-0.142</sub>
Arp 230	4	1	9.91	-21.75	–	1.08	0.35	9.68	–	1.20	2.64 <sup>+0.70</sup> <sub>-0.11</sub>	0.063	0.335 <sup>+0.167</sup> <sub>-0.141</sub>
IC 5298	4	1	11.22	-24.92	193	1.91	0.08	0.81	0.36	1.62	2.57 <sup>+1.61</sup> <sub>-0.79</sub>	0.335	0.299 <sup>+0.119</sup> <sub>-0.106</sub>
Mrk 1014*	4	1	12.31	-28.16	–	1.00	–	–	–	3.86	2.82 <sup>+8.00</sup> <sub>-2.82</sub>	0.674	0.263 <sup>+0.129</sup> <sub>-0.155</sub>

As Table 1, but for the recent merger remnant sample of Rothberg & Joseph (2004). Note that we show the  $K$ -band as opposed to  $V$ -band absolute magnitudes. Systems marked (\*) are excluded from our comparison in this paper owing to contamination from a central AGN. Systems marked (†) should be regarded with caution, as unrelaxed or prominent disk/bar features make our fits unreliable. Some of the best-fit simulation parameters ( $n_s(\text{sim})$  and  $f_{sb}(\text{sim})$ ) are slightly different from those in Paper I owing to an expanded set of simulations, but it makes no difference for our comparisons.

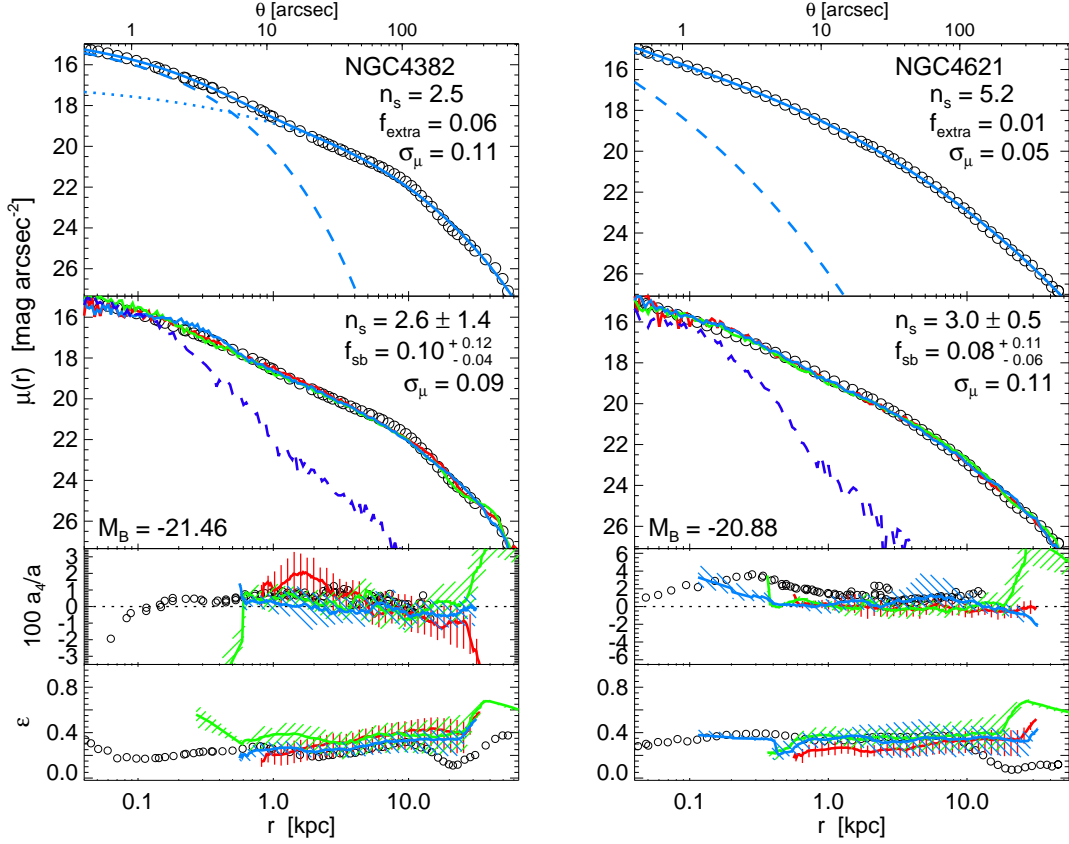


FIG. 33.— As Figure 3, but in log-log space. Surface brightness profiles are shown for cuspy ellipticals in the Virgo cluster. Open circles show the observations, from Kormendy et al. (2008). These are the highest-mass cusp or extra light ellipticals in Virgo<sup>9</sup> ( $\sim 2M_*$ ). *Top*: Observed V-band surface brightness profile with our two component best-fit model (solid, dashed, and dotted lines show the total, inner/extra light component, and outer/pre-starburst component). The best-fit outer Sérsic index, extra light fraction, and variance about the fit are shown. *Middle*: Colored lines show the corresponding surface brightness profiles from the three simulations in our library which correspond most closely to the observed system (shown outside the gravitational softening length,  $\sim 30$  pc). Dashed line shows the profile of the starburst light in the best-matching simulation. The range of outer Sérsic indices in the simulations (i.e. across sightlines for these objects) and range of starburst mass fractions which match the observed profile are shown, with the variance of the observations about the best-fit simulation<sup>10</sup>. *Bottom*: Observed disk/boxy-ness ( $a_d$ ) and ellipticity profiles, with the median (solid) and 25–75% range (shaded) corresponding profile from the best-fitting simulations above. Note that these are not fitted for in any sense. Figures 34–41 show the other cusp ellipticals in the sample, ranked from most to least massive.

## APPENDIX

## A. FITS TO THE SAMPLE OF KORMENDY ET. AL. 2008

In Figures 33–41 we reproduce Figures 3–12, but with profiles shown in log-log projection as opposed to  $r^{1/4}$  projection.

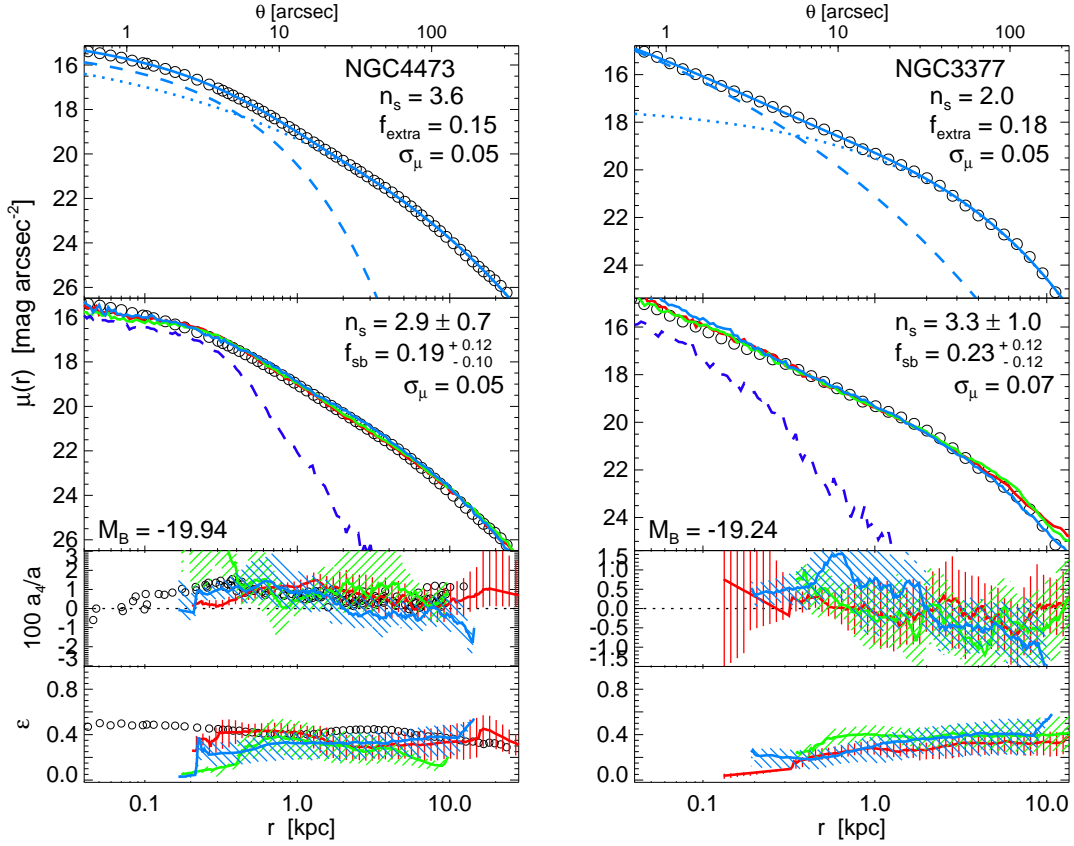


FIG. 34.— The next most massive cusp ellipticals ( $\sim 1 M_*$ ). Note that NGC 3377 is not a Virgo member. (As Figure 5, but in log-log space.)

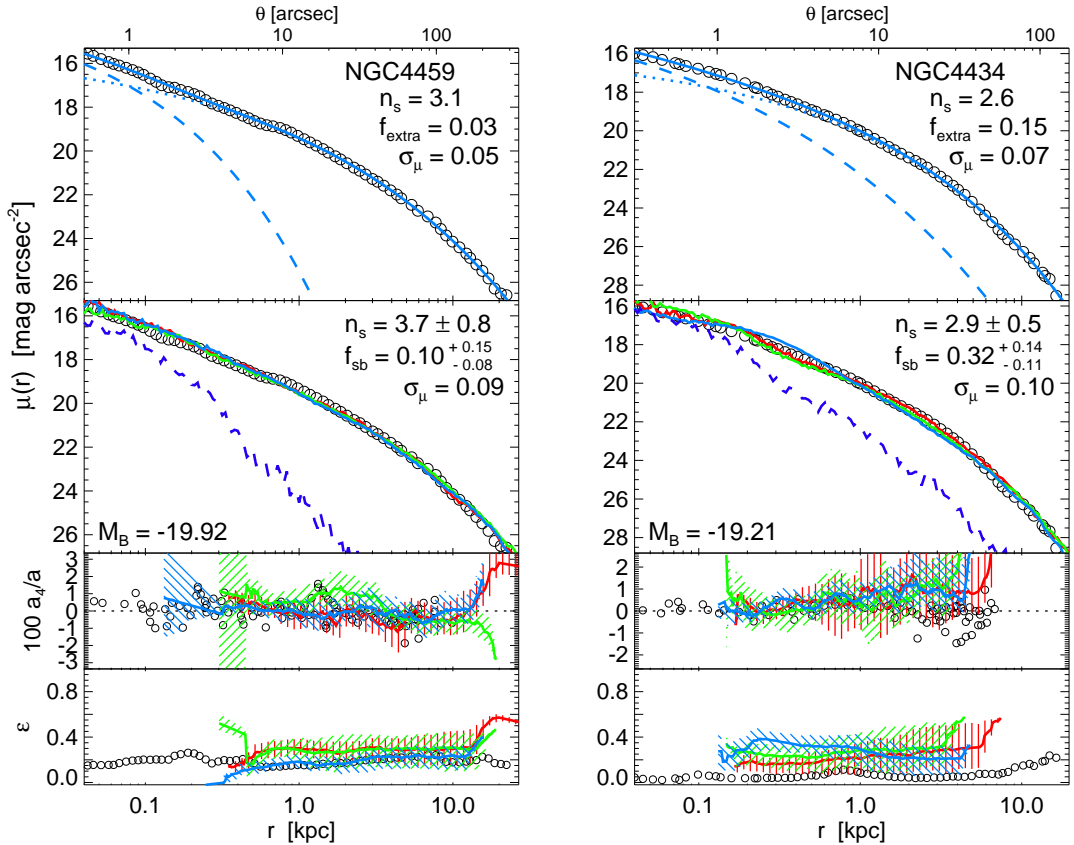


FIG. 35.— The next most massive cusp ellipticals ( $\sim 0.5 M_*$ ). (As Figure 6, but in log-log space.)



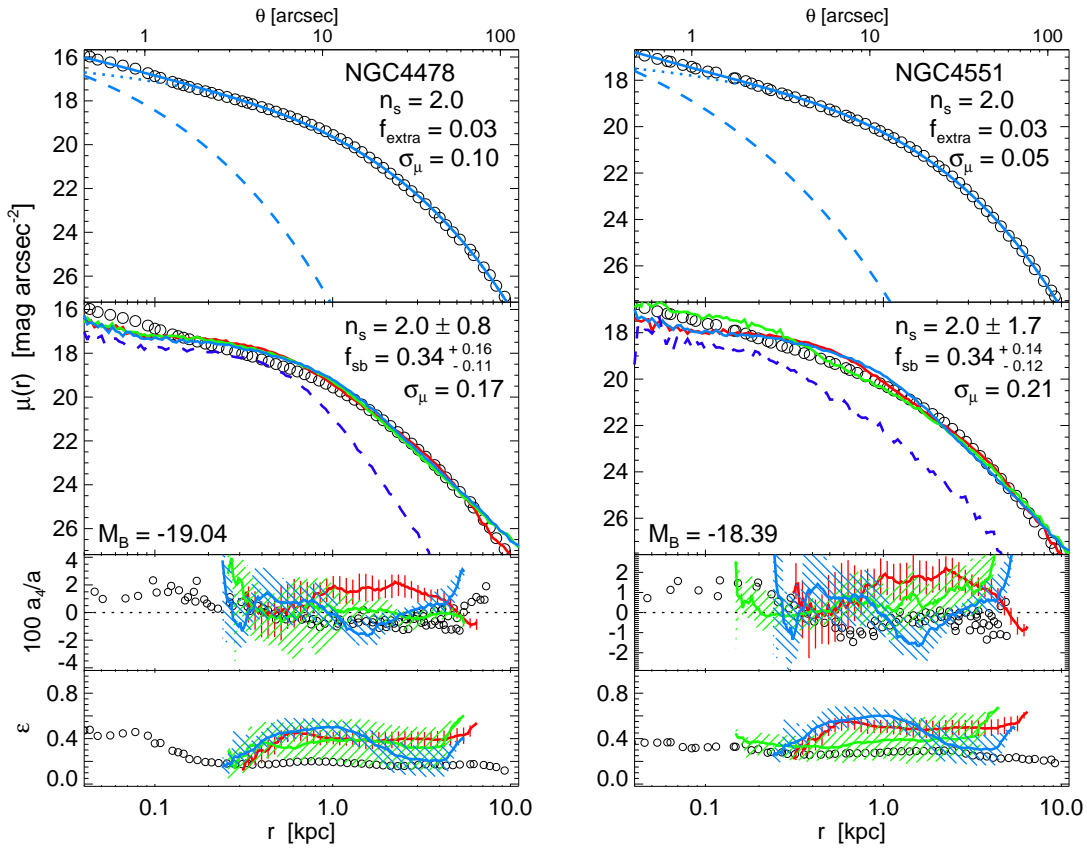


FIG. 36.— Lower-mass cusp ellipticals ( $\sim 0.2\text{--}0.3M_*$ ). Our simulations reproduce the observed outer profiles and kinematic properties of such galaxies, but do not resolve the stellar cluster nuclei at small radii. The extra light recovered by our two-component fits therefore can be misleading at such low mass. (As Figure 7, but in log-log space.)

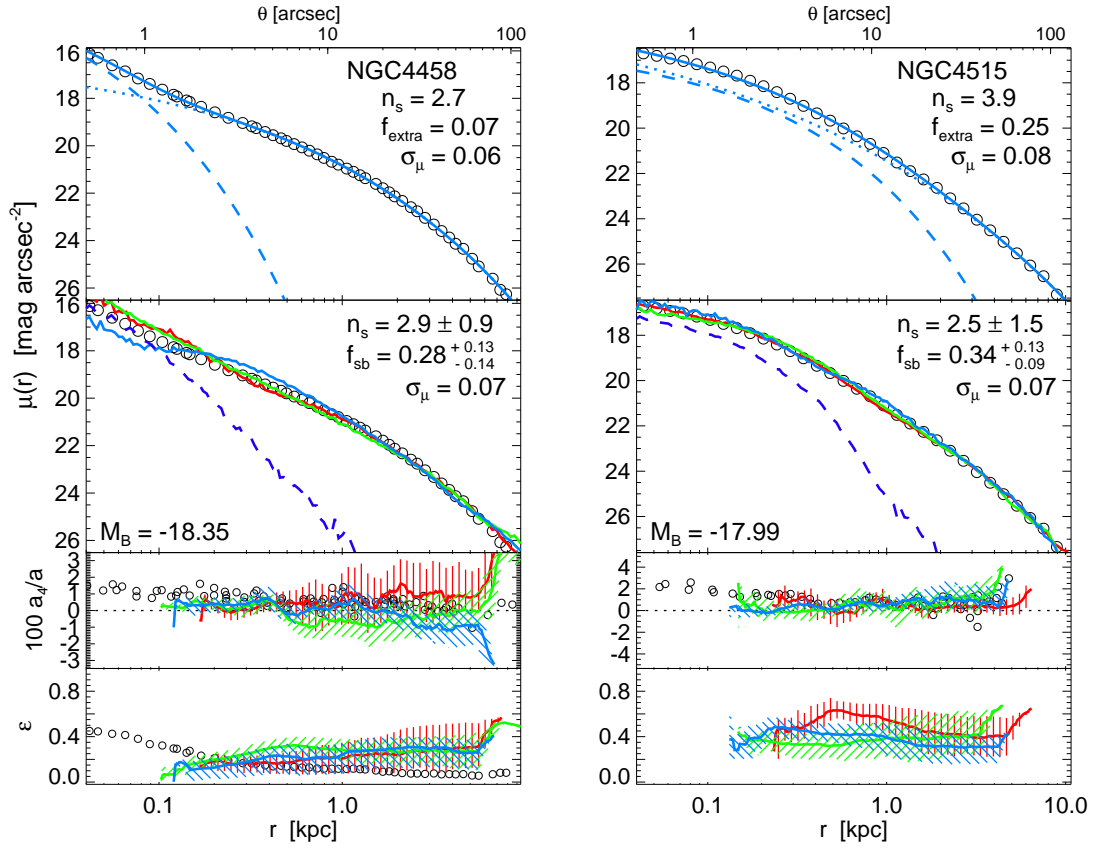


FIG. 37.— Additional low-mass ( $\sim 0.2M_*$ ) cusp ellipticals. Our fits perform better in this case. (As Figure 8, but in log-log space.)

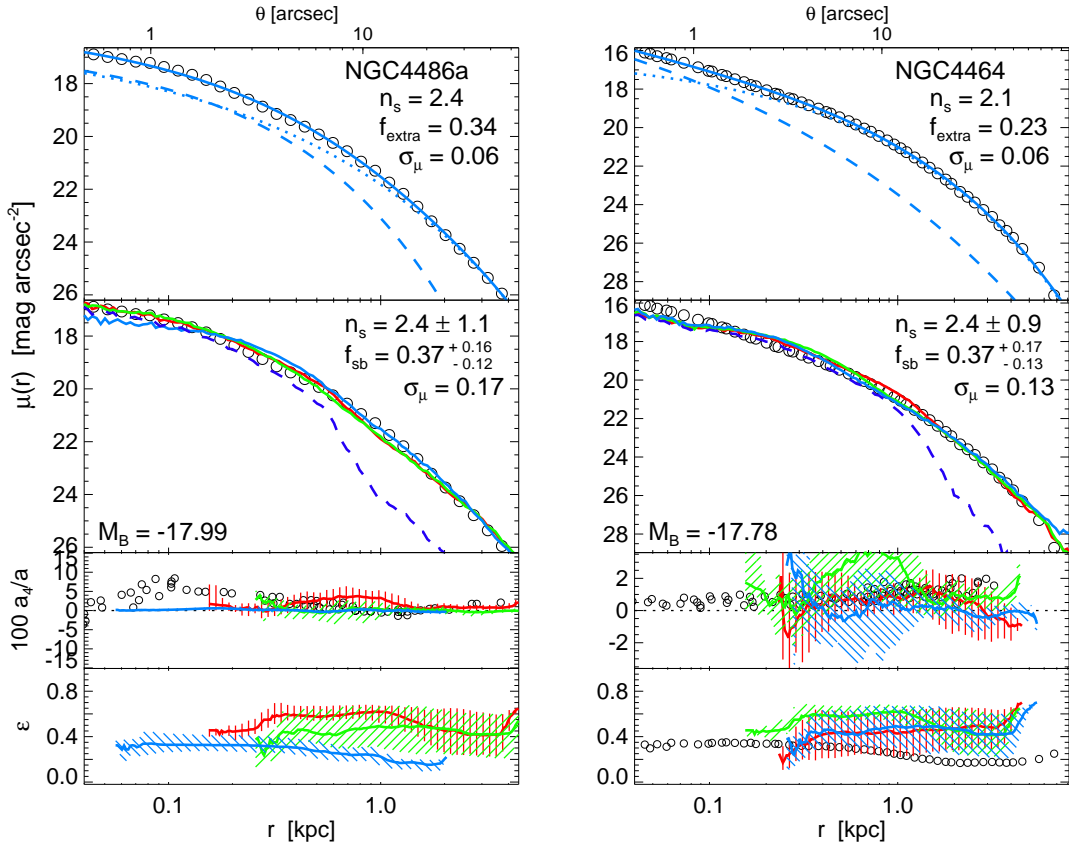


FIG. 38.— Additional low-mass ( $\sim 0.1\text{--}0.2M_*$ ) cusp ellipticals, but in this case without prominent stellar clusters in their nuclei. In this case our parameterized fitting is not misled and we recover similar starburst fractions to our simulations. (As Figure 9, but in log-log space.)

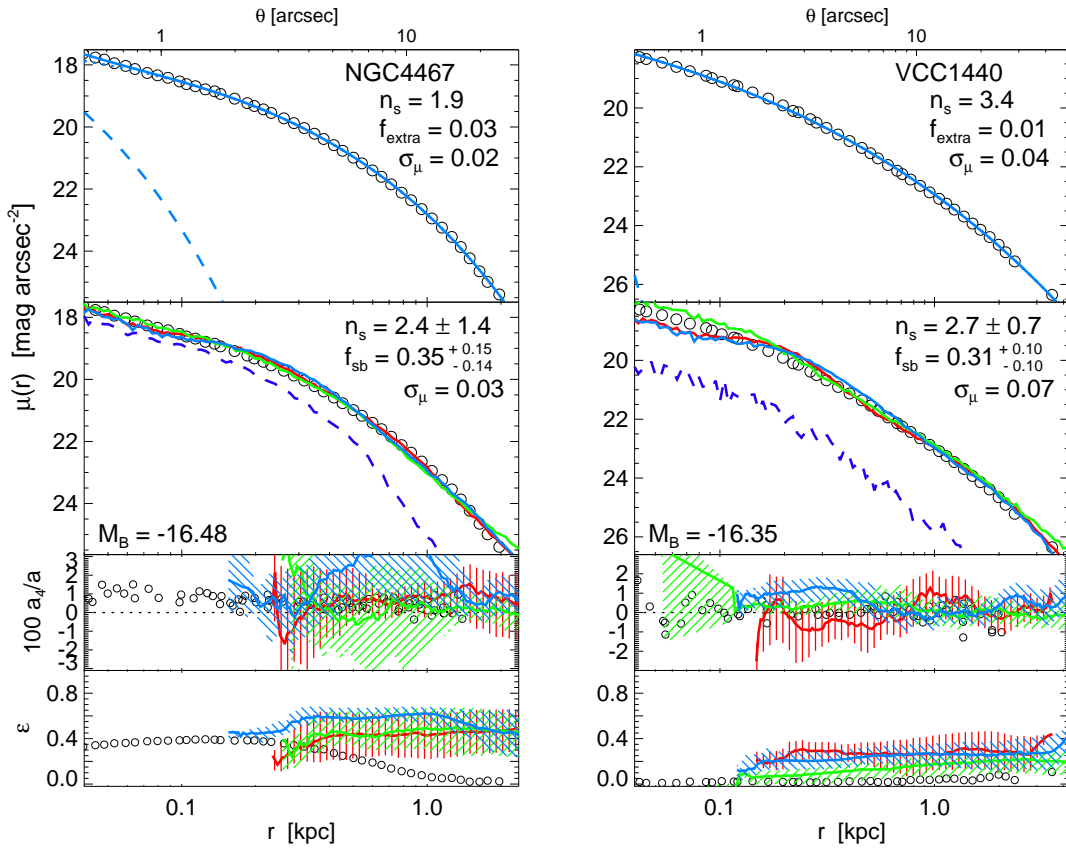


FIG. 39.— Very low-mass cusp ellipticals ( $\sim 0.03\text{--}0.1M_*$ ). Our simulations provide less good matches at these luminosities, where dwarf galaxies dominate the spheroid population (ellipticals at these masses are very rare). Robustly resolving the extra light in these very small systems probably requires  $\lesssim 10\text{pc}$  spatial resolution. (As Figure 10, but in log-log space.)

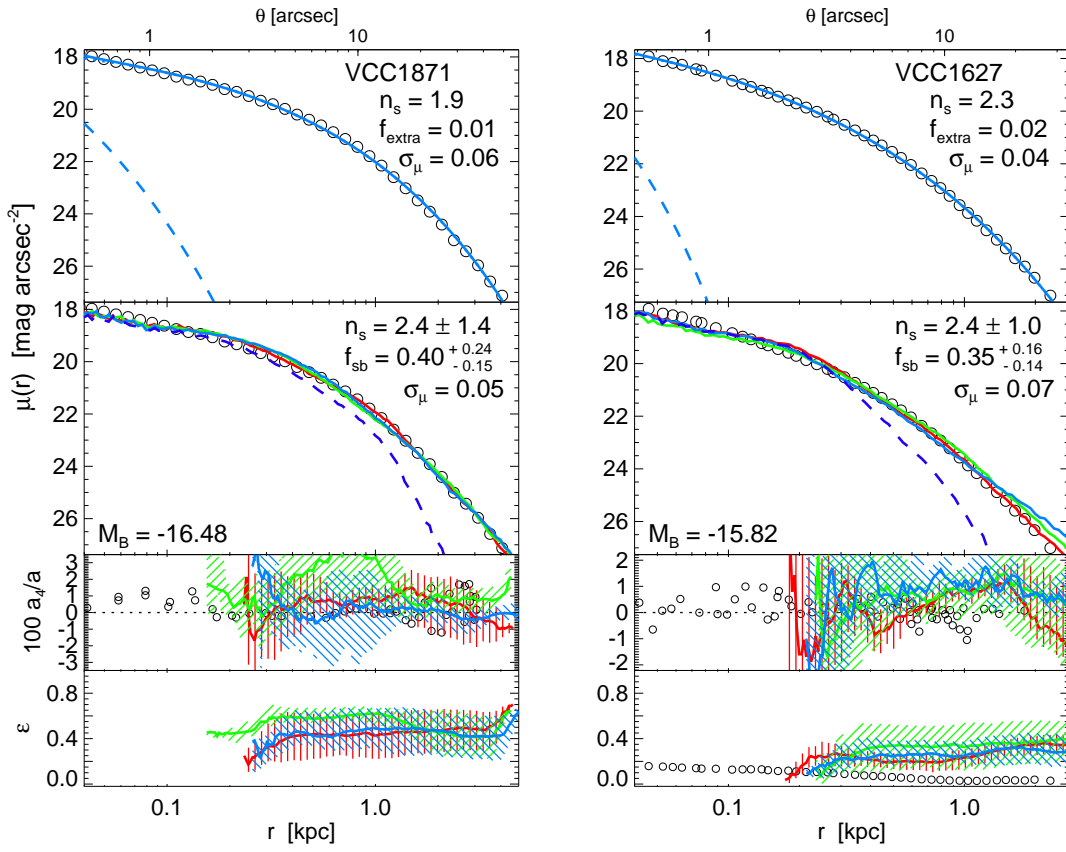


FIG. 40.— The lowest-luminosity cusp ellipticals in Virgo ( $\sim 0.01 M_*$ ). The comparison with our simulations is similar to Figure 39. (As Figure 11, but in log-log space.)



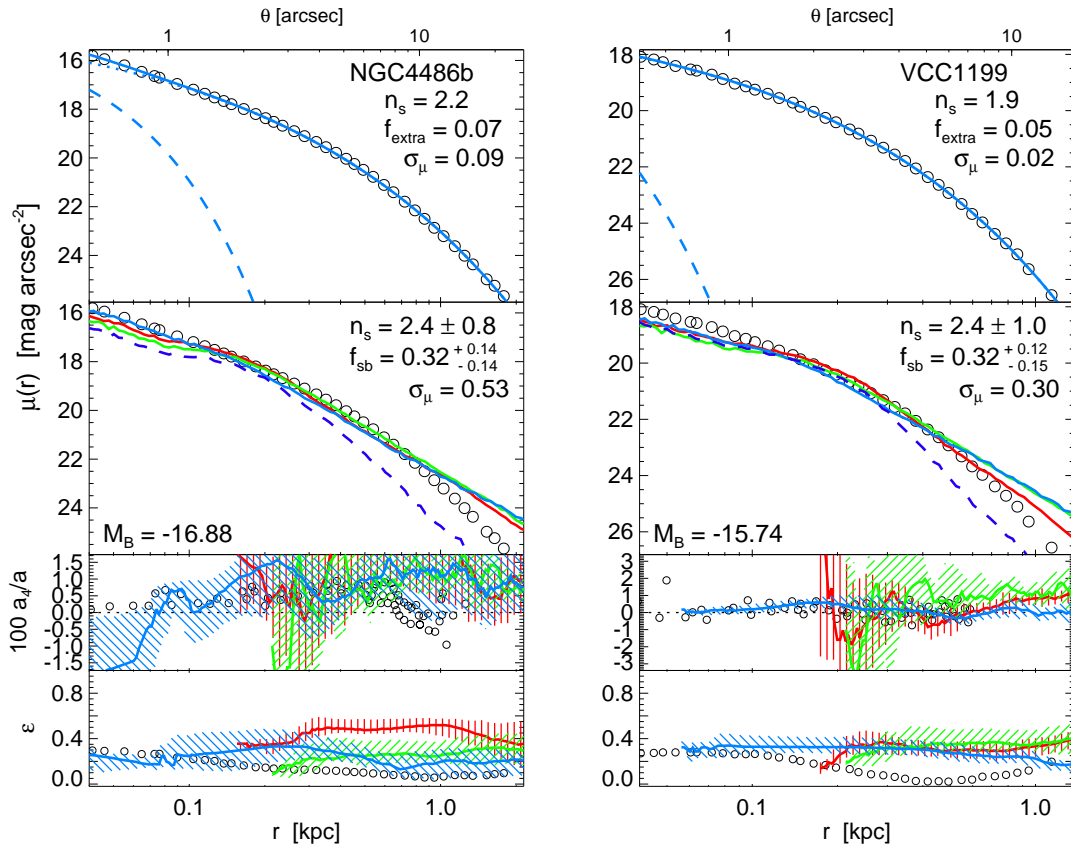


FIG. 41.— “Compact ellipticals.” None of our simulations are as compact as these objects (effective radii  $\sim 200$  pc). (As Figure 12, but in log-log space.)

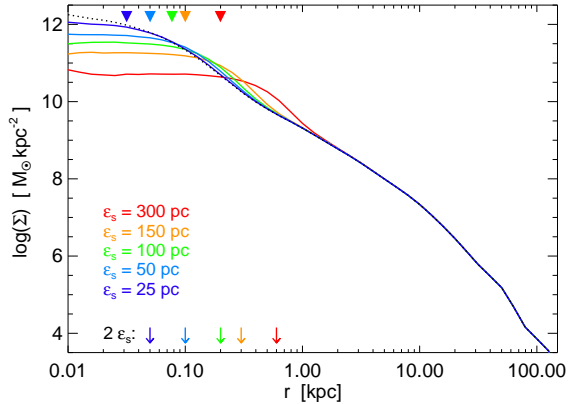


FIG. 42.— Effects of resolution on a remnant from a simulation of a gas-rich merger. We show profiles of otherwise identical simulations with a large dissipational starburst, but different gravitational softening lengths  $\epsilon_s$ . Dotted line is the profile (extrapolated to  $r \rightarrow 0$ ) of a typical “cuspy” elliptical (logarithmic slope  $d \ln I / d \ln(r) \rightarrow 0.5$  as  $r \rightarrow 0$ ). Finite resolution limits mean our profiles will always artificially flatten within some radius: triangles at top show where each simulation profile artificially flattens below this slope ( $d \ln I / d \ln(r) = 0.5$ ); this tends to happen at our softening length  $\approx \epsilon_s$ . Arrows are shown for each simulation at  $2\epsilon_s$ : at  $\sim 2-3\epsilon_s$ , the profiles are converged within  $\sim 0.1$  mag (good for our purposes in this paper). At  $\gtrsim 5\epsilon_s$  the profiles and kinematics are fully converged.

#### B. ARE GAS-RICH MERGER REMNANTS “CUSPS”? RESOLUTION TESTS AS $R \rightarrow 0$

In Paper I, we conduct resolution tests and demonstrate that the primary quantities of interest here, namely the extra light fraction and outer Sérsic index, are reasonably well converged for the mass range of interest given our typical  $< 100$  pc spatial resolution. In that paper, however, the observations had comparable (or poorer) spatial resolution to our simulations; the HST observations of the nuclear regions of ellipticals, on the other hand, resolve extremely small scales  $\sim 1-10$  pc, well below our typical simulations. It is therefore of some interest to examine the behavior at small radii in our simulations.

Figure 42 shows an example of the (sightline-averaged) surface brightness profile of a simulated major merger remnant as a function of numerical resolution, reflected in the gravitational softening length  $\epsilon_s$ . Clearly, at some point around our resolution limits, the profiles artificially flatten (according to the softening) and become flat (essentially creating an artificial “core” at the center).<sup>14</sup> It is clear that, as we increase our resolution, the profiles continue to rise towards smaller and smaller radii. In detail, outside of  $\sim 2-3\epsilon_s$ , we find that the profiles are sufficiently well-converged for our purposes in this paper. However, more subtle, detailed features in the galaxies such as the boxy or disky-ness of the isophotal shapes  $a_4/a$  (typically a  $\sim 1\%$  effect in the deviation of the shapes from ellipses) and central kinematics, converge less rapidly. Nevertheless we find that outside of  $\sim 5\epsilon_s$ , there are no measurable resolution effects in any of these parameters.

<sup>14</sup> Note that this is different from the behavior seen in earlier generations of numerical simulations such as those in Mihos & Hernquist (1994a). In those simulations, time integration inaccuracies at the highest densities led the stellar cusps to artificially contract to the spatial resolution set by the gravitational softening length, yielding sharp, compact “spikes” in the surface brightness profile. This did not affect any other aspects of the evolution and, indeed, if these spikes are smoothed on the spatial scale set by the condition that the starburst component be self-gravitating, the results of Mihos & Hernquist (1994a) agree in detail with those presented here and in Hopkins et al. (2008d).

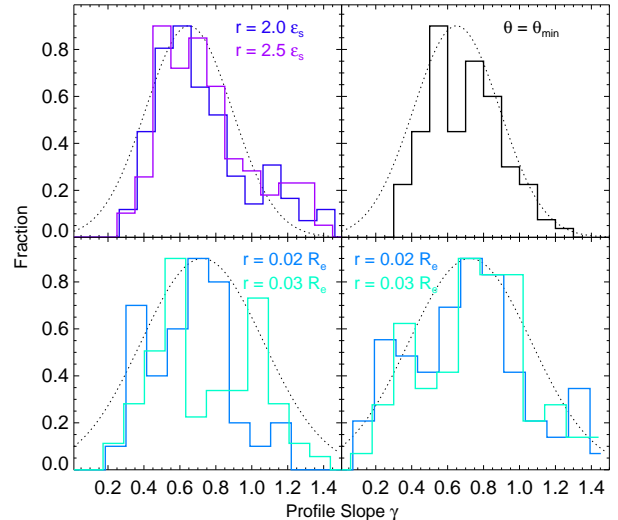


FIG. 43.— “Cuspy-ness” of our simulations at reasonably resolved radii. *Top Left*: Distribution of brightness profile slopes ( $\gamma \equiv -d \ln I / d \ln(r)$ ) in the remnants of gas-rich simulations, at the smallest radii where resolution limits do not completely flatten the profiles (measured at  $\sim 2.0\epsilon_s$  and  $2.5\epsilon_s$ ). *Top Right*: Same, but slopes are measured from the observed profiles at the HST resolution limits for each object. Dotted line in both panels is a fit to the observed distribution (see Lauer et al. 2007a). *Bottom Left*: Profile slopes from the simulations, measured at fixed (fractional) radius ( $0.02R_e$  and  $0.03R_e$ ); we include only simulations where these radii are  $> 3\epsilon_s$ . *Bottom Right*: Observed profile slopes measured at the same fractional radii ( $0.02R_e$  and  $0.03R_e$ ). Dotted line in the lower panels is a fit to the observed distribution at  $0.02R_e$ . Down to our best resolution limits, the simulated gas-rich merger remnants show typical steep “cuspy” slopes similar to those in the observed cusp population.

Where do our resolution limits flatten the profiles into false cores? We check this by simply adopting the common observational definition of a “core” (Faber et al. 1997; Lauer et al. 2007a), namely where the logarithmic derivative of the surface brightness profile flattens below a threshold  $I \propto r^{-1/2}$  ( $-d \ln I(r) / d \ln r < 0.5$ ). This is shown in Figure 42. On average, our systems only significantly flatten into false cores at  $r \lesssim 1\epsilon_s$ . In other words, nearly all of our gas-rich merger simulations, including those pushing our spatial resolution to  $\lesssim 20$  pc, have “cuspy” nuclear profiles (by the observational definition) all the way down to the gravitational softening length.

This approaches (and in the best cases overlaps with) the radii where the observed slopes are classified as “cusps” or “cores.” We therefore directly check whether the slopes of our simulated systems are similar to those observed. We already know that many of our simulations match observed profiles down to  $\sim 50$  pc, from Figures 3-13; here we use our highest-resolution simulations and test whether the slopes at the smallest radii we can reliably say anything about are reasonable or not. We consider the distribution in logarithmic slopes of our simulations at  $2\epsilon_s$ , the smallest radii where they are not strongly flattened by resolution effects, and compare with the observed nuclear slope distribution from Lauer et al. (2007a) at the observational resolution limits. In a more physically motivated manner, we compare the slopes measured at fixed radii relative to the effective radius  $\sim 0.02-0.03R_e$  in both our simulations and observations (comparison at fixed absolute radius yields similar results), only including simulations (and observations) where these radii are well-resolved ( $> 3$  times the resolution limit). In either case, the agreement is good. This strongly suggests that, down to  $\sim 10$  pc where the physics of e.g. individual star-forming sites becomes im-

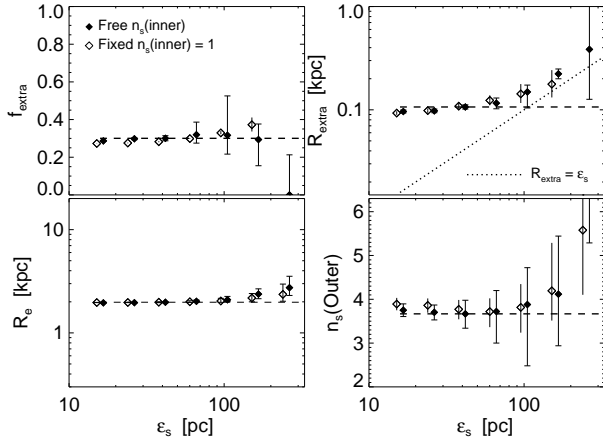


FIG. 44.— Convergence properties of the quantities of interest in this paper, for an otherwise identical simulation (shown in Figure 42) as a function of gravitational softening length  $\epsilon_s$ . Filled diamonds show results from fitting the projected profile to our two-component decomposition, with a free inner Sérsic index/shape parameter  $n'_s$ ; open circles adopt a fixed  $n'_s = 1$ . Error bars show the  $\pm 1\sigma$  range owing to shot noise, statistical fit degeneracies, and variation between different realizations. The quantities of interest here are well converged for our typical resolution limits  $\sim 30\text{--}50\text{pc}$ . For all resolutions ( $\lesssim 100\text{pc}$ ) where the quantities are converged, we obtain the same average answers using a free  $n'_s$  or fixed  $n'_s = 1$ ; but when resolution or seeing is relatively poor ( $\gtrsim 30\text{pc}$ ), a fixed  $n'_s$  is useful to minimize the noise (simply owing to the limited dynamic range in the fits).

portant, our gas-rich merger remnants genuinely have “cuspy” or “power-law” central profiles, and that the agreement seen in Figures 3–13 between simulated and observed profiles would continue down to such radii if we only had the numerical resolution. Similar conclusions were obtained in Cox et al. (2006c), who also demonstrated that these conclusions (given a fixed amount of gas at the time of the final merger) are insensitive to the details of the numerical algorithm and feedback prescriptions in the simulations.

Because the inner shape of the extra light clearly changes (continuing to rise towards small  $r$ ) in Figure 42, we examine the convergence properties in a similar resolution test in Figure 44. We plot the fitted extra light fraction  $f_{\text{extra}}$ , effective radius of the extra light component  $R_{\text{extra}}$ , effective radius of the whole elliptical inferred from the fit  $R_e$ , and outer Sérsic index  $n_s$ , in otherwise identical simulations as a function of  $\epsilon_s$ . We show the median values across a large number of sightlines, but the sightline-to-sightline distribution behaves as a whole in the same manner (see Paper I for resolution tests demonstrating the convergence of the distribution of  $f_{\text{extra}}$  and  $n_s$  across sightlines). For each simulation, we generate alternative realizations by randomly re-scattering the stars according to the smoothing kernel, and show the error bars corresponding to the  $\pm 1\sigma$  range in fits to these realizations (unlike e.g. the variation from sightline-to-sightline, much of which is real in that it reflects actual asymmetries in the galaxy, this variation is purely a resolution effect, and should vanish as  $\epsilon_s \rightarrow 0$ ). The error bars therefore effectively include the formal statistical errors and fit degeneracies as well. We show results both for a fixed inner  $n'_s = 1$  (the Sérsic index of the extra light component itself, as described in § 4), and free inner  $n'_s$  (i.e. both assuming a fixed extra light component shape or fitting for the shape).

Two broad rules of thumb consistently emerge from our resolution tests. First, regardless of the exact details of our fit methodology, the quantities of interest here, especially  $f_{\text{extra}}$ ,  $n_s$ , and  $R_e$  are well-converged for spatial resolution below  $\sim 100\text{pc}$  ( $\sim 1''$  at the distance to Virgo, a factor  $\sim 10$

larger than the HST diffraction limit). We demonstrate in Paper I that the distribution of these quantities across sightlines is also reasonably well-converged below this threshold. In terms of general criteria, global quantities (such as  $R_e$ ) converge quickly (at a resolution  $\sim$  a couple hundred pc), followed by integral quantities such as  $f_{\text{extra}}$  and quantities related to the “outer” (large-scale) profile ( $n_s$ ). The effective radius of the extra light ( $R_{\text{extra}}$ ) is more demanding, because of course the fitted size will not be smaller than the resolution limits (generally we find this is converged up to a smoothing length  $\lesssim 1/2$  of the converged or “true” extra light size). For this reason, we do not reproduce observed systems with  $R_{\text{extra}} \ll 100\text{pc}$  (see Figure 21 and Figures 39–41), but this is only relevant for a few of the very lowest-mass  $\sim 0.01L_*$  ellipticals in our sample. Most demanding, of course, is the detailed shape of the extra light component itself (as  $r \rightarrow 0$ ), which Figures 42 and 43 demonstrate we are only marginally resolving in our highest-resolution simulations. We reach almost identical conclusions regarding convergence if we repeat this study by artificially degrading the seeing in the observed profiles. Note that the absolute values here are for  $\sim 0.1\text{--}1L_*$  ellipticals – in much larger, more massive systems (especially those with flat central cores extending to  $\sim 100\text{--}300\text{pc}$ ), the resolution limits can be much less restrictive. In any case our resolution studies and experiments with observed profiles suggests we are not significantly biased in our estimates of the most important quantity here,  $f_{\text{extra}}$  (or  $f_{\text{sb}}$ ).

Second, Figure 44 explicitly demonstrates that our results are not changed whether we (for convenience) adopt a fixed inner extra light component shape  $n'_s$  when we fit to our simulations, or leave it as a free parameter. In the mean, the two recover the same answer (so long as our resolution is below the  $\sim 100\text{pc}$  threshold needed to resolve the structures of interest in the first place). Unsurprisingly, when the resolution is extremely good, the results are most robust when we allow a free  $n_s$  – this allows the fit the freedom to deal with small scale features and e.g. the broad range in inner profile “cusp” slopes (Figure 43). Fixing  $n'_s$  in such cases (or in e.g. observations with  $\sim 1\text{--}5\text{pc}$  resolution) can produce a higher rate of catastrophic failure owing to the presence of small-scale features that are unimportant for the overall profile. For example, a strict inner exponential ( $n'_s = 1$ ) implies that the logarithmic slope of the surface brightness profile goes to zero as  $r \rightarrow 0$ , whereas the small-scale ( $\ll 30\text{pc}$ ) profiles of cusp galaxies have a wide range of non-zero logarithmic slopes.

When the resolution is sufficient then, one can (and should) free  $n'_s$  and fit for the shape of the inner component as well as its radius and mass fraction (although, again, fixing it introduces no bias, just a higher failure/confusion rate). However, Figure 44 also shows the expected behavior as the resolution is downgraded: up to the limits where properties are converged, fits with a free inner component shape recover the same answer on average, but the uncertainties (realization-to-realization noise and fit degeneracies) grow rapidly (owing largely to the poor resolution of the converged extra light shape, which gives the fit too much freedom to trade off extra light and outer components). The result is that, as noted in § 4, our results for this paper are entirely unchanged if we re-fit all our simulations with a free inner  $n'_s$ , but the scatter in predicted quantities increases significantly. When the resolution is poor, then, especially if the data sets of interest are limited (i.e. one does not have so large a number of objects that very large scatter is not a problem), fixing the inner shape is a convenient assumption that greatly reduces fitting degen-

eracies and, for the choice of inner shape  $n'_s \sim 1$ , introduces no significant systematic bias. Fortunately, the behavior in Figure 44 and our other resolution tests is reasonably simple, and yields a useful rule of thumb: it is appropriate to free the inner component  $n'_s$  and fit for the shape of the extra light with resolution better than  $\sim 20\text{--}30\text{pc}$  (ideally  $\lesssim 10\text{pc}$ ), or equivalently with resolution such that the extra light size  $R_{\text{extra}}$  is resolved with at least  $\sim 5\text{--}10$  resolution elements. Again, we find the same is true for observations (the observations used in this paper – at least for the intermediate and massive galaxies – easily meet this criterion, with  $\sim 10\text{--}20\text{pc}$  corresponding to  $\sim 0.1\text{--}0.3''$  at Virgo, a factor of a couple larger than the HST diffraction limit).

Our dynamic range at large radii is, of course, not significantly limited in the simulations (rather we restrict to a comparable range to that observed). For a detailed study of the dynamic range requirements at large radii for fitting e.g. the outer  $n_s$ , we refer to Kormendy et al. (2008). We note though their conclusions (which we also find in limited experiments changing our sampled dynamic range) that for the observations and simulations here, the dynamic range is sufficient so as not to introduce bias or significantly larger uncertainties.

#### C. THE DISTINCTION BETWEEN STELLAR NUCLEI AND EXTRA LIGHT

Many spiral galaxies and dwarf spheroidals show a central excess in their light profiles associated with dense stellar nuclei (nuclear star clusters) (Phillips et al. 1996; Carollo et al. 1997, 1998; Carollo 1999; Matthews et al. 1999; Böker et al. 2002, 2004; Seth et al. 2006). In their analysis of the ACS Virgo data, this is what Côté et al. (2006) and Ferrarese et al. (2006) identify as the central “excess” component (largely in their dwarf spheroidal sample). In rough terms, this aspect of these nuclei is superficially similar to what we identify as extra light. However, as we discuss in § 4 and has been demonstrated with detailed HST observations of these objects (see e.g. Carollo 1999; Matthews et al. 1999; Böker et al. 2004; Walcher et al. 2006), on closer examination it is immediately clear that these nuclei are very different and physically distinct from the extra light or starburst components we identify in the observations and model in our simulations.

Figure 45 compares the parameter correlations of extra light components and stellar nuclei; specifically their stellar masses, effective radii, and effective surface brightness or surface mass density  $\sim M/(2\pi R_e^2)$ . The sequence of stellar nuclei is clearly distinct from that of extra light. The typical extra light component (effective radius  $\sim 100\text{--}500\text{pc}$ ) is  $\sim 100$  times larger in spatial extent than a stellar nucleus (effective radius  $\sim 1\text{--}5\text{pc}$ ) at the same surface brightness. The slopes of the sequences in either projection shown in Figure 45 are nearly perpendicular: for starburst/extra light components, we find  $I_e \propto M_*^{-0.8}$  (less massive systems are *more* dense and compact); for the stellar nuclei,  $I_e \propto M_*^{+1.3}$  (less massive systems are *less* dense). If we include the limited subsample of stellar nuclei with velocity dispersions measured in Geha et al. (2002) and Walcher et al. (2005), we find similar results in fundamental projections involving  $\sigma$ .

In fact, it is well established that the parameter correlations of stellar nuclei are similar to those of globular clusters, not ellipticals (e.g. Carollo 1999; Geha et al. 2002; Böker et al. 2004; Walcher et al. 2005, and references therein), and we show this in Figure 45. The extra light components, on the other hand, form a relatively smooth extension of the se-

quence obeyed by ellipticals (in terms of the elliptical total half-mass radius and mass; see e.g. Kormendy 1985b) towards smaller radii and higher surface densities. This is a natural prediction of our models: in § 7 and Hopkins et al. (2008a) we argue that ellipticals and bulges are (when analyzed as a single entity) driven along these correlations by the properties of their starburst/extra light, beginning from a location in parameter space (occupied by the least dissipational ellipticals with large radii and low surface brightness) similar to their progenitor disks. In short, dissipational/starburst components represent a smoothly rising excess at  $\sim 0.5\text{--}1\text{kpc}$  from an outer dissipationless component extending to  $\sim 10\text{--}100\text{kpc}$  in classical bulges and ellipticals, with smooth associated gradients; stellar nuclei represent a sharp excess (being a distinct *object* with a fairly steep internal density profile; see e.g. Walcher et al. 2005) at  $\sim 1\text{--}5\text{pc}$ , with very distinctive properties. To the extent that stellar nuclei exist in some ellipticals, they would sit “on top” of the extra light that dominates the profile within  $\sim 100\text{--}500\text{pc}$ , and exist entirely below the radius regime we model or fit.

As discussed in § 4, this is borne out by a detailed comparison between our fits and those in e.g. Côté et al. (2006) and Ferrarese et al. (2006), who fit multi-component profiles to identify stellar nuclei in the very small-scale nuclear regions of Virgo galaxies. The “outer” profile in their images is based on the HST ACS profiles, which extent to outer radii  $\sim 1\text{kpc}$  (almost entirely dominated by the starburst component of the galaxy), and their identified stellar clusters typically dominate the light profile at very small radii  $\lesssim 0.01R_e$ . This is akin to separating our “inner” component itself into multiple sub-components – i.e. a starburst stellar component that blends relatively smoothly onto the outer, violently relaxed stars and an innermost nuclear star cluster.

Moreover, the mass fractions of these components are very different. Figure 46 compares the distribution of stellar nucleus mass fractions (relative to their host bulges) versus the mass fractions of extra light/starbursts. The characteristic stellar nucleus has a mass fraction  $\sim 0.001\text{--}0.003M_{\text{gal}}$  (we plot the distribution fitted in Côté et al. (2006), but other studies find very similar distributions; see e.g. Carollo et al. 1997; Matthews et al. 1999), compared to  $\sim 0.1M_{\text{gal}}$  in extra light. Because the star clusters are typically identified in much less massive galaxies, the discrepancy is even larger ( $\sim 4\text{--}5$  orders of magnitude) if we consider absolute masses. No amount of hierarchical merging, then (which would roughly conserve mass fractions in these components), would move a stellar cluster into the regime of extra light components.

A number of other properties reveal the sharp division between these populations. The stellar populations in the extra light (see § 8) tend to be of similar (albeit slightly younger) stellar age to their hosts ( $\sim 3\text{--}10\text{Gyr}$ ), and are highly metal enriched (typical central metallicities  $\sim 1.5\text{--}3$  times solar) and moderately  $\alpha$ -enhanced ( $[\alpha/\text{Fe}] \sim 0.2\text{--}0.3$ ). Stellar nuclei tend to be extremely young (ages  $\lesssim 100\text{Myr}$ ) and have somewhat sub-solar metallicities (Walcher et al. 2006). There are also kinematic differences, with characteristically less rotation in nuclear clusters (Geha et al. 2002).

Altogether, there should be no risk of confusing stellar nuclei and dissipational components with detailed observations. It is worth noting that at the very lowest elliptical masses ( $M_* < 10^9 M_\odot$ ,  $M_B \gtrsim -17$ ) and very highest stellar nuclei masses, the parameter sequences in Figure 46 approach one another, albeit still with opposite slopes. The most likely ex-

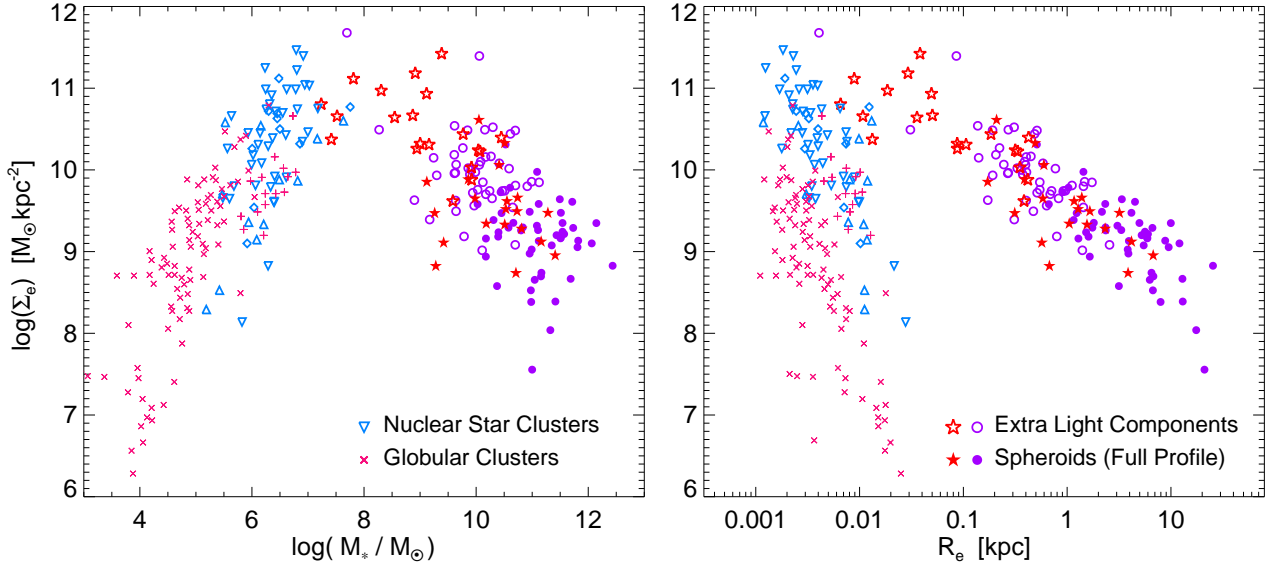


FIG. 45.— Fundamental parameter correlations of extra light components (open red stars and violet circles; style as in Figure 14), compared to those of stellar nuclei (nuclear stellar clusters or “central massive objects”; blue symbols). *Left*: Effective surface mass density versus stellar mass (a nearly identical plot is obtained if we consider surface brightness versus luminosity). Observed stellar nuclei parameters are from Geha et al. (2002, triangles), Böker et al. (2004, inverted triangles), and Walcher et al. (2005, diamonds). The two classes of systems not only separate strongly in mass, but trace nearly perpendicular correlations with *opposite* physical senses. For comparison, we plot the corresponding points for the entire elliptical profiles (filled symbols) and for globular clusters (pink symbols;  $\times$ 's and crosses are Milky Way and NGC 5128 (Cen A) globulars from Harris (1996) and Harris et al. (2002); Martini & Ho (2004), respectively). Extra light components form a continuous extension of the spheroid/elliptical population (“classical” stellar bulges also lie along this correlation when plotted); unsurprising given that we argue they drive the effective radii and central surface brightness of the ellipticals. Stellar nuclei, on the other hand, appear to follow (at least roughly) an extension of the correlations for globular clusters. *Right*: Same, but showing surface density versus effective radius of each component/population. Although the sequences may approach each other at the very lowest elliptical masses (where classical bulges and ellipticals are rare, and where we may have misidentified some dwarf spheroidals as ellipticals), there is a sharp division between their structural properties, masses, radii, and parameter correlations (also, stellar population ages and metallicities; see text). The two are in general easy to separate and should not be confused.

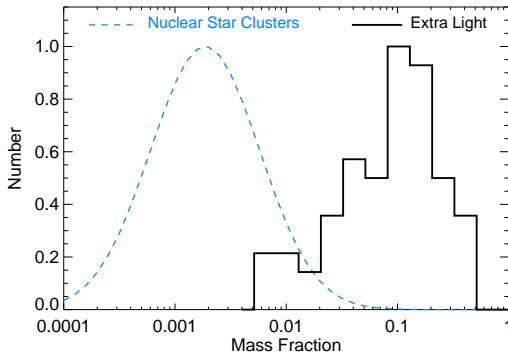


FIG. 46.— Distribution of the mass/light fraction of the galaxy bulge in stellar nuclei (dashed; from the fit to the distribution observed in Côté et al. 2006) versus our fitted extra light components (solid). Stellar nuclei have typical mass fractions  $\sim 2-3 \times 10^{-3} M_{\text{bul}}$ , whereas extra light is typically  $\sim 0.1 M_{\text{bul}}$ , a two order-of-magnitude difference. The gap between the populations is even larger if we consider e.g. absolute masses, effective radii, masses relative to the whole galaxy (as opposed to the bulge), or our best-fit simulation  $f_{\text{sb}}$  (instead of the fitted  $f_{\text{extra}}$ , which has somewhat more scatter). The systems are more than just distinct; it is not possible to assemble typical extra light components from any amount of hierarchical merging/aggregation of stellar nuclei.

planation is that this is just a coincidental overlap of their structural scalings, and in any case, true ellipticals and classical bulges become extremely rare at such low masses (likewise, stellar nuclei at and above these masses also become rare). It is also possible that, at these masses, some of our smallest ellipticals are really misclassified dwarf spheroidals (which have significant stellar nuclei; our fitting procedures might then mistakenly call that nucleus the “extra light”) or that we are in these couple of cases finding a real stellar nucleus in an elliptical and accidentally calling it the extra light

(as opposed to recognizing the larger, less dense starburst component, on top of which such a stellar cluster would sit at the center of the surface brightness profile). Figures 7 & 36 show examples where our parameterized fitting may fall victim to this misclassification. In general however, even at the lowest classical bulge masses and highest stellar nuclei masses, the other striking differences in the systems (their stellar populations and kinematics) remain distinct: there is no continuity or “intermediate” class between the two populations in our data or the literature.

It is in principle possible that there would be correlations between extra light and stellar nuclei, in that both might be formed by dissipational processes (see e.g. Milosavljević 2004; Seth et al. 2006). Moreover, at some level similar physics may be involved in determining e.g. the competition between star formation and gravitational collapse that determines their size-mass relations. However, given their separation in stellar populations, and given the prevalence of stellar nuclei in systems such as bulgeless disks and dwarf spheroidals that have manifestly *not* experienced major dissipational angular momentum loss, they probably are not directly coupled.



TABLE 3  
EXTENDED FIT RESULTS

Name (1)	Morph. (2)	Ref. (3)	$\mu_e$ (extra) (4)	$R_e$ (extra) (5)	$n'_s$ (extra) (6)	$\mu_e$ (out) (7)	$R_e$ (out) (8)	$n_s$ (out) (9)	$f_e$ (fit) (10)	$n_s$ (sim) (11)	$f_{sb}$ (sim) (12)
NGC 4621	E4/E/E5	1,2,3	$17.38^{+4.82}_{-1.02}$	$0.24^{+2.25}_{-0.21}$	$3.91^{+4.50}_{-2.91}$	$21.42^{+0.62}_{-2.20}$	$4.33^{+2.35}_{-1.48}$	$3.23^{+1.51}_{-0.75}$	$0.053^{+0.005}_{-0.044}$	$3.06^{+1.70}_{-0.18}$	$0.140^{+0.168}_{-0.050}$

As Table 1, but with a complete list of fit parameters (included as supplemental material in the on-line edition of the journal; here, we show an illustrative example of one table entry). Parameters are the same as in Table 1, with additional fitted parameters listed. Added columns include: (2) Morphology (taken from the sources given in column (3), in the same order). (3) Source for surface brightness profiles (as in Table 1), where 1=Kormendy et al. (2008), 2=Lauer et al. (2007a), 3=Bender et al. (1988), 4=Rothberg & Joseph (2004). (4)-(10) Parameters of our two-component fits: (4) Effective surface brightness (in mag arcsec<sup>-1</sup>, i.e.  $\mu(R_{\text{extra}})$ ), for the fitted inner (starburst) component. (5) Effective radius of the extra light component  $R_{\text{extra}}$  [kpc]. (6) Sérsic index of the extra light component  $n'_s$  (cases with  $n'_s = 1$  and errors = 0 are where  $n'_s$  is held fixed as described in the text). (7) Effective surface brightness of the outer (violently relaxed envelope) component. (8) Effective radius of this component. (9) Sérsic index of this component ( $n_s$ (fit) in Table 1). (10) Integrated mass/light fraction in the fitted “extra” (inner) component. (11) Range of outer Sérsic indices (equivalent of  $n_s$ (out)) fit in the same manner to the best-fit simulations, at  $t \approx 1 - 3$  Gyr after the merger when the system has relaxed. (12) Fraction of light from stars produced in the central, merger-induced starburst in the best-fit simulations ( $\pm$  the approximate interquartile range allowed). These values are medians for the fits to the available photometric profiles for each galaxy; they do not, together, represent the best fit to any particular individual measurements.